IDŐJÁRÁS

QUARTERLY JOURNAL OF THE HUNGAROMET
HUNGARIAN METEOROLOGICAL SERVICE

CONTENTS

VOL. 130 * NO. 2 * APRIL – JUNE 2026

IDŐJÁRÁS

Quarterly Journal of the HungaroMet Hungarian Meteorological Service

Editorial Office: Kitaibel P.u. 1, H-1024 Budapest, Hungary
P.O. Box 38, H-1525 Budapest, Hungary
E-mail: journal.idojaras@met.hu

Indexed and abstracted in Science Citation Index Expanded™ and Journal Citation Reports/Science Edition
Covered in the abstract and citation database SCOPUS®
Included in EBSCO's database

Subscription by mail:
IDŐJÁRÁS, P.O. Box 38, H-1525 Budapest, Hungary
E-mail: journal.idojaras@met.hu

DOI:10.28974/idojaras.2026.2.1

IDŐJÁRÁS

Quarterly Journal of the HungaroMet Hungarian Meteorological Service
Vol. 130, No. 2, April – June, 2026, pp. 101–115

Two decades of increasing aridity and temperature trends in the Nagykunság region, Hungary (2005–2024)

Krisztina Varga, **Seren Zedan**, **Gergő Asbolt***, **Loujaine Seddik**, **István Csízi**, **Géza Tuba**, **György Zsigrai**, and **József Zsembeli**

Hungarian University of Agriculture and Life Sciences, National Research Centre for Climate and Regional Land Management, Karcag, Kisújszállási út 166, H-5300, Hungary

**Corresponding author E-mail: Asbolt.Gergo@uni-mate.hu*

(Manuscript received in final form on August 26, 2025)

Abstract— To better understand the impacts of global and regional climate change, it is essential to conduct investigations at the local level as well, particularly in climatically sensitive areas. The aim of our study is to present the climatic characteristics of the Nagykunság region based on annual data recorded at the Karcag meteorological station (HungaroMet 55405) between 2005 and 2024. Our analysis focuses on the long-term trends of key meteorological variables such as temperature, precipitation, evaporation, sunshine duration, wind speed, and air pressure. For data processing, we used the built-in statistical tools of Microsoft Excel, especially linear regression, moving averages, and trendline fitting. During the examined period, we identified a significant increase in temperature (+0.097 °C/year), a slight decrease in precipitation (–9.72 mm/year), and a rise in the number of sunshine hours (+18.95 hours/year). Our results highlight not only the ongoing climatic changes but also the urgent need for regional adaptation measures, particularly in agricultural management and water resource planning. The methodology demonstrates that accessible statistical tools can provide valuable insights to support local climate resilience strategies.

Key-words: Nagykunság region, weather data, long-term analysis, extreme weather

1. Introduction

The study of climate change impacts has become one of the most complex and urgent scientific and societal challenges of recent decades (*Intergovernmental Panel on Climate Change (IPCC),* 2023). Numerous studies have documented changes in global climate systems, highlighting the rise in average temperatures, the reorganization of precipitation patterns, and the increasing frequency of extreme weather events (*Alexander et al.,* 2006; *Coumou* & *Rahmstorf,* 2012; *Fischer* and *Knutti,* 2015). While global and continental-scale climate models are indispensable for large-scale forecasting, identifying local and regional trends is essential for developing effective adaptation strategies (*Giorgi,* 2006; *Lelieveld et al.,* 2012; *Seneviratne et al.,* 2012).

Hungary is located on the continental fringe of the temperate zone, where the alternating influence of western European, Atlantic, and eastern European air masses prevails (*Péczely,* 1979; *Bartholy* and *Pongrácz,* 2010). These atmospheric characteristics, combined with the country's diverse topography – especially in the flat regions of the Great Hungarian Plain – result in significant microclimatic variations. In the Great Hungarian Plain, changes in temperature and precipitation patterns are particularly pronounced, directly affecting agricultural production, water management, and the condition of ecosystems (*Spinoni et al*., 2015).

In recent decades, rising summer temperatures and decreasing precipitation have already been documented in the Great Hungarian Plain. The observed climatic trends in this region show significant deviations compared to other parts of the country, particularly between the Trans-Tisza and Transdanubia regions. This highlights the necessity of locally focused trend analyses, which enable the identification of region-specific impacts and their integration into climate-related decision-making processes (*Bartholy et al*., 2015; *Szabó et al*., 2019).

Nagykunság is an agroecologically significant region located in the central part of the Trans-Tisza region, characterized by flat terrain and a continental climate that gives rise to distinct climatic features (*Biró* and *Kovács,* 2024). In this area – particularly in Karcag – arable crop production and extensive grassland management play a dominant role, while semi-natural habitats such as saline grasslands and loess steppes are highly sensitive to weather extremes (*Tölgyesi et al*., 2020). The region's climatic conditions – especially the seasonal variability of precipitation, temperature extremes, and fluctuations in sunshine duration – directly influence site-specific growing conditions and agricultural productivity (*Pongrácz et al*., 2011; *Kocsis* and *Schweitzer,* 2013). Therefore, the analysis of local meteorological trends is justified not only from a scientific standpoint but also for practical reasons, particularly to support the foundation of climate adaptation measures.

A reliable foundation for meteorological trend analyses is provided by long-term, consistently recorded, and homogenized data series. The development of the

automatic station network of the Hungarian Meteorological Service (HungaroMet) enables the temporal analysis of daily-resolution, validated data (*Izsák et al*., 2022). From these datasets, annual averages and totals can be calculated, yielding suitable indicators for examining trends in temperature and precipitation patterns, sunshine duration, and wind conditions (*Izsák* and *Szentimrey*, 2020).

In the town of Karcag (Jász-Nagykun-Szolnok County), the automatic meteorological station (code 55405) of HungaroMet has been recording daily meteorological data since 2005. Among the variables measured by the station are total precipitation, average, minimum, and maximum temperature, wind speed, sunshine duration, and global radiation. By aggregating these into annual datasets, a reliable time series can be constructed, enabling the examination of regional meteorological trends.

For the trend analysis, we used the built-in statistical tools of Microsoft Excel, particularly linear regression trendlines, moving averages, and the calculation of the coefficient of determination (R^2). These straightforward methods are well-suited for examining the long-term direction, magnitude, and reliability of changes in meteorological variables. Therefore, the aim of this study is not to provide an in-depth statistical analysis through complex climate modelling, but rather to demonstrate that valuable insights into regional climate changes can be drawn using Excel-based tools.

In our study, we hypothesize that meteorological data recorded in Karcag between 2005 and 2024 reveal a gradual warming and drying trend, which may have significant agroecological implications for the Nagykunság region. The objective of our analysis is to assess the extent to which local weather trends reflect broader climatic changes characteristic of the Great Hungarian Plain and the Carpathian Basin, and to examine how these changes influence the ecological and agricultural stability of the region. Our findings aim to contribute to a deeper understanding of the region's climatic sensitivity and to provide a foundation for future ecological, agricultural, or climate adaptation studies.

2. Materials and methods

For our analysis, we used daily meteorological data from the automatic weather station located in Karcag (station code: 55405). The study covered the period from 2005 to 2024.

The daily meteorological variables measured by the station and included in the analysis are presented in *Table 1*.

Table 1. Meteorological variables used in the study

Variable name	Symbol	Unit	Description
Average daily temperature	*t*	°C	Daily average temperature
Minimum daily temperature	*tn*	°C	Lowest daily temperature
Maximum daily temperature	*tx*	°C	Highest daily temperature
Daily precipitation sum	*rau*	mm	Amount of daily precipitation
Potential evapotranspiration	*upe*	mm	Daily potential evapotranspiration
Sunshine duration	*ns*	hours	Number of sunshine hours per day
Global radiation	*sr*	J/cm²	Daily sum of global radiation
Relative humidity	*u*	%	Daily average relative humidity
Average wind speed	*f*	m/s	Daily average wind speed
Synoptic wind speed	*fs*	m/s	Daily average synoptic wind speed
Maximum wind gust	*fx*	m/s	Maximum wind speed per day
Soil temperature at 5 cm	*et5*	°C	Daily average soil temperature at 5 cm depth
Near-surface minimum temperature	*tsn24*	°C	Daily minimum near-surface temperature
Average air pressure	*p*	hPa	Station-level daily air pressure
Sea-level pressure	*p0*	hPa	Air pressure adjusted to sea level

Annual aggregates were calculated from daily values according to the nature of each variable. For precipitation and potential evapotranspiration, we calculated annual sums; for temperature and atmospheric parameters, we computed annual averages, minima, and maxima (*Table 2*).

Additionally, seasonal breakdowns were performed for spring, summer, autumn, and winter to identify seasonal variations. Furthermore, a section on extreme weather events (e.g., water-deficit and drought periods) was included, comparing these to the climatic water balance (CWB – *Thornthwaite* and *Mather*, 1955).

To assess temporal trends, we applied linear regression models using the statistical functions of Microsoft Excel. The slope of the regression line and the corresponding p-value were used to evaluate long-term changes in each variable.

Table 2. Annual totals calculated on the basis of daily meteorological data for the years under study (Karcag, 2005–2024)

Year	*t* (°C)	*tn* (°C)	*tx* (°C)	*rau* (mm)	*upe* (mm)	*ns* (h)	*sr* (J/cm2)	*u* (%)	*f* (m/s)	*fs* (m/s)	*fx* (m/s)	*et5* (°C)	*tsn24* (°C)	*p* (hPa)	*p0* (hPa)
2005	9.8	-23.3	35.2	702.5	901.9	3046	511614.3	76.9	1.9	1.9	20.6	11.5	-11.6	1006.7	1017.6
2006	10.6	-16.5	34.3	585.3	981.5	2962	509486.9	76.1	1.9	1.9	21.9	11.8	-13.7	1007.5	1018.4
2007	12.0	-7.5	40.0	552.6	1289.5	3009	547125.8	68.8	2.4	2.4	25.1	13.0	-6.4	1006.1	1016.9
2008	11.4	-13.8	37.7	574.9	1048.5	3096	516925.2	74.1	2.3	2.3	24.9	12.3	-9.4	1006.4	1017.2
2009	11.6	-20.5	35.2	556.1	1216.2	2914	515396.6	70.9	2.2	2.2	22.7	12.4	-13.1	1004.7	1015.5
2010	10.4	-17.9	34.8	890.1	798.5	2846	488422.8	80.6	2.1	2.1	21.0	11.7	-11.0	1003.6	1014.4
2011	11.1	-13.9	37.6	385.7	1146.0	3070	487753.4	72.3	2.0	2.0	22.9	11.8	-7.6	1008.3	1019.2
2012	11.5	-21.2	38.8	344.8	1292.1	3154	521339.6	70.1	2.3	2.3	20.2	12.0	-13.1	1006.0	1016.8
2013	11.6	-13.5	37.7	574.2	1092.8	3001	464846.1	75.6	2.3	2.2	20.8	11.7	-9.3	1005.2	1016.0
2014	12.2	-11.9	35.4	630.0	991.8	2984	516984.6	77.5	2.0	2.0	24.5	13.1	-10.8	1005.5	1016.3
2015	12.1	-11.0	38.2	408.7	1160.5	2891	526305.1	73.9	2.2	2.2	25.1	12.8	-10.8	1008.2	1019.0
2016	11.2	-13.7	33.8	591.7	1013.9	3001	526893.0	75.9	2.0	2.0	20.2	12.2	-11.9	1006.6	1017.4
2017	11.2	-18.0	38.6	527.0	1159.3	3000	540046.9	72.9	2.3	2.3	22.0	12.2	-5.9	1006.9	1017.7
2018	12.4	-12.7	34.5	556.9	1178.7	3027	531891.6	74.4	1.9	1.9	19.3	12.9	-9.7	1006.2	1017.0
2019	12.5	-11.3	37.4	484.5	1152.3	3044	530244.8	72.8	2.2	2.2	28.6	12.9	-9.0	1005.6	1016.4
2020	11.7	-7.8	36.5	649.5	993.2	2848	507500.1	76.0	2.1	2.0	22.7	12.6	-9.1	1007.2	1018.1
2021	11.2	-12.6	37.5	397.8	1120.0	2983	523278.1	73.4	2.1	2.1	25.6	14.2	-10.1	1006.5	1017.3
2022	12.1	-14.1	39.4	342.0	1310.0	3000	521948.6	69.2	2.2	2.2	26.0	14.8	-11.0	1007.3	1018.1
2023	12.7	-8.8	37.9	572.3	1145.1	2512	408014.1	75.1	2.4	2.4	24.2	14.5	-8.9	1005.3	1016.1
2024	13.4	-9.5	39.5	357.1	1324.4	2896	495684.3	73.1	2.2	2.1	21.6	17.1	-7.6	1006.2	1017.0

Climatic variables were analyzed over time using linear trend analysis, which involved the following methodological steps: trends were estimated by fitting a linear regression line to the annual time series data. The slope (β) of the fitted line expresses the average annual change in the variable (e.g., mm/year or °C/year).

The strength of the linear fit was expressed using the coefficient of determination (R^2), indicating the percentage of total variance explained by the linear model. Trends were visualized in graphs, displaying the regression line along with its slope (β), p-value, and R^2. The temporal changes were statistically analyzed using linear regression in Excel (LINEST and TREND functions), and the results were validated with non-parametric methods. For this, the Mann-Kendall trend test (*McLeod*, 2022) and Sen's slope estimator (*Pohlert*, 2023) were applied using the latest version of the R programming language (R 4.5.1, 2025-06-13 ucrt). The Kendall package (version 2.2.1) and the trend package (version 1.1.6) were used for robust trend analysis, suitable for data that may not meet normal distribution assumptions. This approach confirmed the direction and statistical significance of the results obtained in Excel.

3. Results

The trend analysis covered all available meteorological variables (*Table 3*). Using annual averages, totals, and extremes derived from daily values, we calculated the parameters of linear regression models along with their significance levels. The variables were evaluated by grouping them according to their nature. Seasonal analyses revealed additional details, while the 5-year moving averages smoothed out natural interannual fluctuations and highlighted more pronounced long-term changes.

Based on the trend parameters of the examined variables, it is advisable to clearly distinguish between significant ($p < 0.05$), nearly significant ($0.05 \leq p < 0.1$), and non-significant ($p \geq 0.1$) trends. Notably, the strongest correlations were observed for average temperature (*t*), minimum temperature (*tn*), and soil temperature (*et5*), where the coefficient of determination (R^2) exceeded 0.25. Seasonal breakdowns revealed the most pronounced temperature increases during spring and summer, especially in the case of maximum temperature (*tx*). This trend coincides with a decrease in spring precipitation sums, resulting in an increased evapotranspiration deficit. During summer, the combined effect of rising temperatures and increasing sunshine hours may critically contribute to water stress in vegetation. In contrast, autumn showed a slight increase in precipitation, while winter saw a rise in minimum temperature (*tn*), which reduces the number of frost days.

Table 3. Trends of meteorological variables based on Excel and R statistical analysis (2005–2024)

Variable	β (slope) (Excel)	R^2 (Excel)	p-value (Excel)	Trend direction	Significance	MK p-value (R)	Sen's slope (R)	Note
t (avg temp)	+0.097 °C/year	0.47	0.01	increasing	significant	0.0022	+0.093 °C/year	warming trend
tn (min temp)	+0.40 °C/year	0.29	0.03	increasing	significant	0.0179	+0.43 °C/year	milder winters
tx (max temp)	+0.103 °C/year	0.10	0.12	increasing	not significant	0.183	+0.13 °C/year	summer warming
rau (precip.)	–9.72 mm/year	0.18	0.08	decreasing	near-significant	0.0743	–9.63 mm/year	precipitation deficit
upe (PET)	+9.23 mm/year	0.15	0.06	increasing	near-significant	0.0904	+8.89 mm/year	intensifying evapotranspiration
ns (sunshine)	–9.18 hours/year	0.17	0.073	decreasing	near-significant	0.0729	–9.63 hours/year	cloudier periods
sr (radiation)	−1079.2 J/cm²/year	0.043	0.44	decreasing	not significant	0.871	+266.5 J/cm²/year	weak trend
u (humidity)	–0.059 %/year	0.01	0.22	decreasing	not significant	0.1614	–0.054 %/year	decreasing humidity
f (avg wind)	+0.003 m/s/year	0.02	0.33	stable	not significant	0.3095	+0.003 m/s/year	slight increase
fs (syn. wind)	+0.0027 m/s/year	0.01	0.35	stable	not significant	0.3276	+0.002 m/s/year	no major change
fx (max gust)	+0.099 m/s/year	0.06	0.14	increasing	not significant	0.2102	+0.092 m/s/year	slight increase in gusts
et5 (soil temp 5 cm)	+0.172 °C/year	0.55	0.02	increasing	significant	0.0027	+0.169 °C/year	near-surface warming
tsn24 (min near-surface temp)	+0.116 °C/year	0.10	0.11	increasing	not significant	0.1416	+0.12 °C/year	increasing ground-level temp
p (air pressure)	+0.011 hPa/year	0.00	0.45	stable	not significant	0.6054	+0.009 hPa/year	nearly unchanged pressure
p0 (sea-level pressure)	+0.0072 hPa/year	0.00	0.47	stable	not significant	0.4834	+0.0068 hPa/year	nearly unchanged pressure

3.1 Temperature trends

The temperature data show a clear warming trend in the annual average temperatures recorded in Karcag (*t*; β = +0.097 °C/year; R^2 = 0.47), indicating a significant linear relationship over time (*Fig. 1*). The Mann–Kendall trend test confirms this tendency (τ = 0.507, p = 0.0022), and the Sen's slope estimate (+0.1 °C/year) is consistent with the regression-based slope. The increase in minimum temperatures (*tn*; β = +0.40 °C/year; R^2 = 0.29) suggests that night-time cooling is becoming progressively milder. According to the Mann–Kendall test (τ = 0.389, p = 0.0179), this trend is statistically significant, and the Sen's slope estimation indicates an increase of +0.43 °C/year. The rise in maximum temperature (*tx*; β = +0.103 °C/year; R^2 = 0.10) is particularly pronounced during the summer months, which may indicate an increase in the number of heatwave days. Despite a visible tendency, the Mann–Kendall test (τ = 0.222, p = 0.183) suggests a non-significant trend, though the Sen's slope estimate remains positive (+0.13 °C/year). The near-surface minimum temperature (*tsn24*) shows a slight increasing trend based on linear regression (β = +0.116 °C/year; R^2 = 0.10), although this trend is not statistically significant (p = 0.11). The Mann–Kendall test, however, yields a near-significant positive trend (τ = 0.277, p = 0.097), and the Sen's slope estimation suggests a warming rate of +0.15 °C/year. The soil temperature at 5 cm depth (*et5*) also displays a clear increasing trend (β = +0.172 °C/year; R^2 = 0.55) with statistical significance (p = 0.02). This warming is further confirmed by a highly significant Mann–Kendall trend (τ = 0.564, p = 0.0006), and the Sen's slope indicates a warming rate of +0.14 °C/year. Average (*t*) and maximum (*tx*) temperatures increase most intensely during the summer months (June–August). In the winter months (December–February), significant increases are observed in the minimum temperature (*tn*) and near-surface minimum temperature (*tsn24*). Moving averages of the temperature variables reveal a clear upward trend, with the most marked increases observed for the soil temperature (*et5*) and minimum temperature.

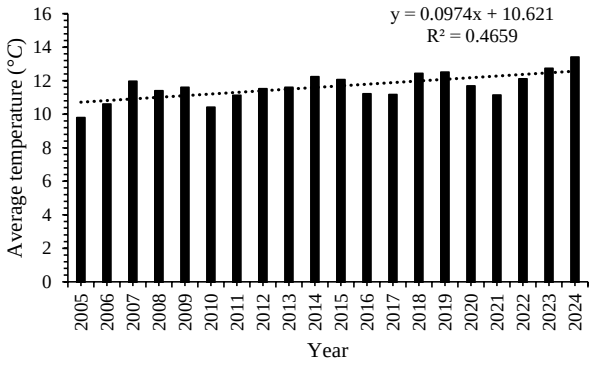

Fig. 1. Trend of annual mean temperature (*t*) in Karcag, 2005–2024.

3.2 Precipitation and evapotranspiration

The annual precipitation total (*rau*) shows a slight decreasing trend (β = –9.72 mm/year; R^2 = 0.18), although due to natural variability, this trend is not pronounced every year. According to the Mann–Kendall test, this trend is near-significant (τ = -0.295, p = 0.074), with a Sen's slope estimate of –9.63 mm/year. In parallel, the potential evaporation (*upe*) is increasing (β = +9.23 mm/year; R^2 = 0.15), indicating enhanced evaporative losses, which is an important implication in terms of drought sensitivity (*Fig. 2*). The Mann–Kendall test indicates a near-significant upward trend (τ = 0.263, p = 0.112), and the Sen's slope estimate is +9.53 mm/year. This dual effect intensifies the evaporation deficit, potentially leading to long-term water supply challenges in the region. Spring precipitation totals (March–May) exhibit the most pronounced decrease, while autumn values show a slight increase. The moving average of precipitation (*rau*) reveals a gradual decline, whereas potential evaporation (*upe*) follows an upward trend.

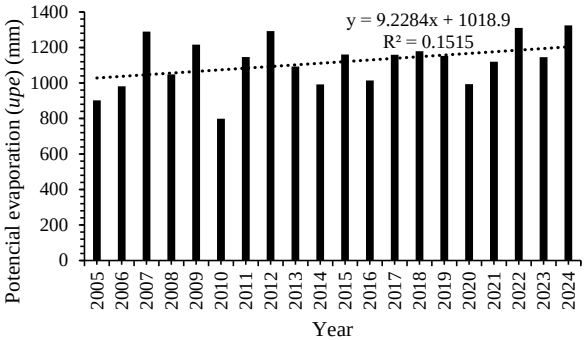

Fig. 2. Trend of annual potential evaporation (*upe*) in Karcag (2005–2024).

3.3 Sunshine and radiation

The number of sunshine hours (*ns*) shows a slight decreasing trend (β = –9.18 hours/year; R^2 = 0.17), which may indicate more frequent periods of cloudiness or changes in atmospheric composition. This is supported by a Mann–Kendall trend (τ = –0.265, p = 0.111), with a Sen's slope of –4.49 hours/year, close to near-significance. The annual total of global radiation (*sr*) also exhibits a slight decreasing trend (β = –1079.2 J/cm²/year) with relatively low explanatory power (R^2 = 0.04), which could be partly related to changes in cloud cover or aerosol levels (e.g., dust, pollen). No significant trend is observed (p = 0.87), and the Sen's slope estimate is statistically insignificant.

3.4 Wind conditions

Both the synoptic wind speed (*fs*) and the average wind speed (*f*) show minimal increases (*fs*: $\beta = +0.0027$ m/s/year; *f*: $\beta = +0.003$ m/s/year), but these trends are statistically weak ($R^2 < 0.02$). No significant trend is supported by the Mann–Kendall test of wind speed ($p = 0.77$), and the Sen's slope estimate is zero. The maximum wind gust speed (*fx*) exhibits an increasing tendency ($\beta = +0.099$ m/s/year), which may amplify extreme fluctuations in the wind climate. A weak upward tendency (Sen's slope = +0.08 m/s/year) is not confirmed by Mann–Kendall ($p = 0.44$). Maximum gusts (*fx*) tend to be stronger during the spring months, while they are weaker in winter.

3.5 Air pressure and relative humidity

Instrument-level (*p*) and sea-level (*p0*) air pressure changes show weak but positive trends (*p*: $\beta = +0.011$ hPa/year; *p0*: $\beta = +0.007$ hPa/year), but based on the coefficients of determination, these are not considered significant changes ($R^2 < 0.01$). The Mann–Kendall test of sea-level shows no trend ($p = 0.97$), the Sen's slope is near zero. Relative humidity (*u*) exhibits a slight decline ($\beta = –0.06$ %/year; $R^2 = 0.015$), which may indicate increasing aridity, especially during the summer months. A decreasing tendency is observed, though the Mann–Kendall ($p = 0.53$) does not confirm statistical significance, while the Sen's slope is –0.08 %/year. Relative humidity decreases moderately in spring and summer, while it remains stable in autumn and winter. Moving averages show minimal variation in air pressure values, and no significant seasonal trends are observed.

Based on daily maximum temperatures, heatwave days exceeding 35 °C were examined for the period 2005–2024 (*Table 4*). Annual data show an increasing trend both in the number and duration of heatwaves. The longest heatwave was recorded in 2022, lasting 11 consecutive days. Both the number of heatwaves and the maximum temperatures have increased year by year, indicating more frequent heat stress conditions during summers.

Table 4. Heatwaves and their characteristics between 2005 and 2024

Year	Number of heatwave days	Number of heatwave events	Longest heatwave (days)	Annual maximum temperature (°C)
2005	2	0	2	35.2
2006	0	0	0	34.3
2007	11	1	7	40.0
2008	3	0	2	37.7
2009	1	0	1	35.2
2010	3	0	2	34.8
2011	6	1	4	37.6
2012	10	1	5	38.8
2013	4	0	2	37.7
2014	5	0	2	35.4
2015	8	1	4	38.2
2016	3	0	2	33.8
2017	7	1	4	38.6
2018	4	0	2	34.5
2019	9	1	5	37.4
2020	3	0	2	36.5
2021	6	1	4	37.5
2022	24	2	11	39.4
2023	5	0	2	37.9
2024	10	1	6	39.5

The annual values of the climatic water balance (*CWB*), calculated as the difference between precipitation and potential evapotranspiration, were negative in almost every studied year, indicating persistent moisture deficits (*Table 5*). Among the most extreme years were 2007 and 2022, with *CWB* values of –736.9 mm and –968 mm, respectively.

The annual number of water-deficit days exceeded 290 on multiple occasions, with the longest continuous period of water deficit lasting 65 days (in 2009). These data clearly underline the increasing drought sensitivity of the region.

Table 5. Climatic water balance (CWB) and water-deficit periods between 2005 and 2024

Year	Annual *CWB* (mm)	Number of water-deficit days	Longest water-deficit period (days)
2005	–199.4	289	28
2006	–396.2	294	36
2007	–736.9	301	41
2008	–473.6	301	34
2009	–660.1	300	65
2010	91.6	252	15
2011	–760.3	303	45
2012	–947.3	306	55
2013	–518.6	291	33
2014	–361.8	276	31
2015	–751.8	303	41
2016	–422.2	290	26
2017	–632.3	298	49
2018	–621.8	296	28
2019	–667.8	299	40
2020	–343.7	285	25
2021	–722.2	303	50
2022	–968.0	308	60
2023	–855.4	310	53
2024	–967.3	309	58

Overall, the results indicate that among the meteorological variables recorded in Karcag, temperature, evapotranspiration, and sunshine duration show significant increasing trends, while decreasing precipitation and relative humidity, along with the increasing number of water-deficit years, point toward climatic drying. The Mann–Kendall test and Sen's slope estimator confirmed the statistical validity of the temperature trends detected by linear regression. We observed weaker but directionally consistent trends in precipitation and evapotranspiration. Trends with p-values below 0.05 were considered statistically significant. The Excel-based analyses effectively capture local signs of climate change and provide an important foundation for further agroclimatic studies.

4. Discussion

The analysis of meteorological data recorded in Karcag reveals clear trends that are consistent with other national and international regional studies. The increasing trends in temperature variables – particularly average and minimum temperatures – corroborate observations across Hungary and Central Europe highlighting intensified warming over recent decades (*Bartholy et al*., 2007; *Pongrácz et al*., 2011).

The moderate but declining trend in precipitation, coupled with rising potential evapotranspiration, projects significant climatic and ecological challenges for the region. This is especially critical for agricultural production, as Nagykunság primarily relies on arable farming and livestock. The increasing frequency of years with high evapotranspiration potential fits well with the concept of a "desiccation spiral" (a process of gradual drought and increasing water scarcity) that has been confirmed by several studies for the Hungarian Great Plain (*Szalai* and *Szinell*, 2000; *Pongrácz et al*., 2011).

The increase in sunshine hours alongside a slight decrease in global radiation may have a dual effect: while the former may support plant growth during the vegetation period, the latter may indicate changes in aerosol content and cloud cover in the climate system, as supported by other Hungarian research (*Lakatos et al*., 2013).

Our results are in agreement with climate projections for the Carpathian Basin, particularly regarding rising temperatures and more extreme precipitation patterns (*Pongrácz et al*., 2011; *Bartholy et al*., 2015). Similar drying trends have been observed in other parts of the Hungarian Great Plain (e.g., Homokhátság, Békés-Csongrád region) (*Szabó et al*., 2019), suggesting that the changes in Nagykunság fit into a broader regional climatic pattern.

The analysis of extreme temperature and water balance-based indicators further supports the observation that in the Nagykunság region, not only gradual warming but also an increased frequency of heat and moisture extremes have been observed over the past two decades. The rising number of days exceeding 35 °C and heatwaves, along with longer periods of water deficit, confirm estimates that the region is particularly vulnerable to the negative agricultural and ecological impacts of climate change (*Blanka* et al., 2013; *Vadas* and *Rácz*, 2013).

Moreover, the application of more robust statistical methods, such as the Mann–Kendall test and Sen's slope estimator, is justified in this study, as they are less sensitive to data variability and non-normal time series distributions. These methods more accurately confirm the direction and significance of climatic changes (*Hirsh et al.*, 1982; *Helsel et al.*, 2002).

A methodological strength of the Excel-based analysis is its ability to efficiently review long time series with basic statistical tools. While it does not replace complex modeling or multivariate statistical analysis, it effectively

captures key trends and can provide a foundation for future research, especially aimed at supporting climate adaptation strategies.

5. Conclusions

Based on data from the Karcag climate station for the period 2005–2024, it can be concluded that the climate changes occurring in the Nagykunság region are clear and affect multiple variables. The gradual increase in temperature, the decrease in precipitation, the rise in evapotranspiration, and the increase in sunshine hours together indicate a drying climatic trend. Although not all variables show significant trends individually, the combined effects clearly outline the warming and drying pattern characteristic of the Great Hungarian Plain. Based on our results, it is recommended to pay increased attention in the region to irrigation strategies, crop selection, and soil protection. Our study also demonstrates that reliable, publishable results can be achieved using simple tools such as Excel, which can provide a solid basis for preparing more complex climate adaptation decisions.

References

Alexander, L.V., Zhang, X., Peterson, T.C., Caesar, J., Gleason, B., Klein Tank, A.M.G., Haylock, M., Collins, D., Trewin, B., Rahimzedah, F., Tagipour, A., Kumar, K. R., Revadekar, J., Griffiths, G., Vincent, L., Stephenson, B.D., Burni, J., Aguilar, E., Brunet, M., Taylor, M., New, M., Zhai, P., Rusticucci, M., and *Vazquez-Aguirre, J.L.,* 2006: Global observed changes in daily climate extremes of temperature and precipitation. *Journal of Geophysical Research: Atmospheres*, *111*(D5), D05109. https://doi.org/10.1029/2005JD006290

Bartholy, J. and *Pongrácz, R.*, 2010: Analysis of precipitation conditions for the Carpathian Basin based on extreme indices in the 20th century and climate simulations for 2050 and 2100. *Physics and Chemistry of the Earth*, *35*(1–2), 43–51. https://doi.org/10.1016/j.pce.2010.03.011

Bartholy, J., Pongrácz, R., and *Gelybó, G.*, 2007: Regional climate change expected in Hungary for 2071–2100. *Applied Ecology and Environmental Research*, *5*(1), 1–17. https://doi.org/10.15666/aeer/0501_001017

Bartholy, J., Pongrácz, R., and *Kis, A.*, 2015: Projected changes of extreme precipitation using multi-model approach. *Időjárás*, *119*(2), 129–142.

Biró, K. and *Kovács, E.*, 2024: Agro-climatic analysis for agricultural adaptation in Hungary. *Periodica Polytechnica Social and Management Sciences*, *32*(2), 141–147. https://doi.org/10.3311/PPso.22482

Blanka, V. Mezősi, G., and Meyer, B., 2013: Projected changes in the drought hazard in Hungary due to climate change. *Időjárás*, *117*(2), 219-237.

Coumou, D. and *Rahmstorf, S.*, 2012: A decade of weather extremes. *Nature Climate Change*, *2*(7), 491–496. https://doi.org/10.1038/nclimate1452

Fischer, E. M. and *Knutti, R.*, 2015: Anthropogenic contribution to global occurrence of heavy-precipitation and high-temperature extremes. *Nature Climate Change*, *5*(6), 560–564. https://doi.org/10.1038/nclimate2617

Giorgi, F., 2006: Climate change hot-spots. *Geophysical Research Letters*, *33*(8), L08707. https://doi.org/10.1029/2006GL025734

Helsel, D.R. and *Hirsch, R.M.*, 2002: Statistical methods in water resources. *U.S. Geological Survey Techniques of Water-Resources Investigations*, Elsevier, Vol. 49, Book 4, Chapter A3. https://doi.org/10.3133/twri04A3

Hirsch, R.M., Slack, J.R., and *Smith, R.A.*, 1982: Techniques of trend analysis for monthly water quality data. *Water Resources Research*, *18*(1), 107-121. https://doi.org/10.1029/WR018i001p00107

IPCC, 2023: Climate Change 2021: The Physical Science Basis. Working Group I Contribution to the Sixth Assessment Report of the Intergovernmental Panel on Climate Change. Cambridge University Press. https://doi.org/10.1017/9781009157896

Izsák, B. and *Szentimrey, T.*, 2020: To what extent does the detection of climate change in Hungary depend on the choice of statistical methods? *GEM - International Journal on Geomathematics*, *11*(1), 17–32. https://doi.org/10.1007/s13137-020-00154-y

Izsák, B., Szentimrey, T., Lakatos, M., Pongrácz, R., and *Szentes, O.*, 2022: Creation of a representative climatological database for Hungary from 1870 to 2020. *Időjárás, 126*(1), 1–26. https://doi.org/10.28974/idojaras.2022.1.1

Kocsis, K. and *Schweitzer, F.* (Eds.)., 2013: Hungary in Maps. Geographical Research Institute, Hungarian Academy of Sciences, Budapest.

Lakatos, M., Szentimrey, T., Bihari, Z., and *Szalai, S.*, 2013: Creation of a homogenized climate database for the Carpathian region by applying the MASH procedure and the preliminary analysis of the data. *Időjárás*, *117*(3), 143–158.

Lelieveld, J., Hadjinicolaou, P., Kostopoulou, E., El Maayar, M., Giannakopoulos, C, Hannides, C., Lange, M.A., Tanarhte, M., Tyrlis, E., and *Xoplaki, E.*, 2012: Climate change and impacts in the Eastern Mediterranean and the Middle East. *Climatic Change, 114*(3–4), 667–687. https://doi.org/10.1007/s10584-012-0418-4

McLeod, A. 2022: Kendall Rank Correlation and Mann-Kendall Trend Test, R package version 2.2.1. https://doi.org/10.32614/CRAN.package.Kendall

Péczely, G., 1979: *Éghajlattan*. Nemzeti Tankönyvkiadó, Budapest. (in Hungarian)

Pohlert, T. 2023: Non-Parametric Trend Tests and Change-Point Detection, R package version 1.1.6. https://doi.org/10.32614/CRAN.package.trend

Pongrácz, R., Bartholy, J., and *Miklós, E.*, 2011: Analysis of projected climate change for Hungary using ENSEMBLES simulations. *Applied Ecology and Environmental Research*, *9*(4), 387–398. https://doi.org/10.15666/aeer/0904_387398

Seneviratne S.I., Nicholls N., Easterling D., Goodes M.C., Kanae, S., Kossin, J., Lou, Y., Marengo, J., McInnes, K., and *Rahimu, M.*, 2012: Changes in Climate Extremes and their Impacts on the Natural Physical Environment. In Field C.B, Barros V., Stocker T.F., Dahe Q., (eds.) *Managing the Risks of Extreme Events and Disasters to Advance Climate Change Adaptation: Special Report of the Intergovernmental Panel on Climate Change*. Cambridge University Press; 109-230. https://doi.org/10.1017/CBO9781139177245.006

Spinoni, J., Naumann, G., Vogt, J., and *Barbosa, P.*, 2015: The biggest drought events in Europe from 1950 to 2012. *Journal of Hydrology: Regional Studies, 3*, 509–524. https://doi.org/10.1016/j.ejrh.2015.01.001

Szabó, S., Szopos, N.M., Bertalan-Balázs, B., László, E., Milošević, D.D., Conoscenti, C., and *Lázár, I.*, 2019: Geospatial analysis of drought tendencies in the Carpathians as reflected in a 50-year time series. *Hungarian Geographical Bulletin*, *68*(3), 283–301. https://doi.org/10.15201/hungeobull.68.3.5

Szalai, S. and *Szinell, Cs.*, 2000: Comparison of two drought indices for drought monitoring in Hungary—A case study. In J. V. Vogt & F. Somma (Eds.), *Drought and Drought Mitigation in Europe* (pp. 161–166). Springer. https://doi.org/10.1007/978-94-015-9472-1_12

Thornthwaite, C.W., Mather, Jr. 1955: The Water Balance. Laboratory of Climatology, Centerton, NJ, USA.

Tölgyesi, C., Török P., Hábenczyus A.A., Bátori, T., Valkó, O., Deák, B. Tóthmérész, B., Erdős, L., and *Kelemen, A.*, 2020: Underground deserts below fertility islands? Woody species desiccate lower soil layers in sandy drylands. *Ecography*, *43*(6), 1–12. http://dx.doi.org/10.1111/ecog.04906

Vadas, A. and *Rácz, L.* 2013: Climatic Changes in the Carpathian Basin during the Middle Ages. The State of Research. *Global Environment, 6*, 198-227. https://doi.org/10.3197/ge.2013.061209

DOI:10.28974/idojaras.2026.2.2

IDŐJÁRÁS

Quarterly Journal of the HungaroMet Hungarian Meteorological Service
Vol. 130, No. 2, April – June, 2026, pp. 117–134

Drought monitoring and assessment with different meteorological drought indices in a transitional climate: Amasya and Merzifon, Türkiye

Utku Zeybekoglu

[1] *Boyabat Vocational School of Higher Education,*
Sinop University, Sinop, Türkiye

Author E-mail: Utku Zeybekoglu, utkuz@sinop.edu.tr

(Manuscript received in final form on April 15, 2025)

Abstract—The identification, monitoring and prediction of the possible future conditions of drought, a complex disaster, are of significance for decision makers in planning natural-social and human activities and planning, operation, and management of water resources. The present study investigates the meteorological drought experienced by Amasya and Merzifon, located within the transition zone between the Black Sea and continental climates in Türkiye. The analysis employs the standardized precipitation index (SPI), the China-Z index (CZI), and the modified China-Z index (MCZI), utilizing annual time scales to assess the precipitation patterns in these regions. The precipitation records obtained from the selected meteorological stations between 1964 and 2023 were analyzed in order to assess the drought and compare the performance of precipitation-based drought indices. The investigation also focused on drought-wet period percentages, the percentages of occurrence of drought classes, and the negative and positive peak index values. According to all three drought indices, significant dry years were identified, including 1964, 1974–1976, 1982, 1984, 1986, 1990, 1999, 2013, 2017, and 2020.The assessment revealed that SPI, CZI, and MCZI performance was similar in identifying drought in transition climate zones. It was also determined that CZI and MCZI are a viable alternative to SPI for drought monitoring.

Key-words: drought assessment; drought indices; comparative analysis; standardized precipitation index (SPI); China-Z index (CZI); modified China-Z index (MCZI)

1. Introduction

Drought is a recurring global phenomenon characterized by multiple climatological and hydrological parameters, causing significant damage to both the natural environment and human life (*Mishra* and *Desai*, 2005; *Adisa et al*., 2020; *Adib et al.*, 2024). Dependent variables that affect drought include temperature, precipitation, and soil properties (*Jenkins* and *Warren*, 2015). Drought is distinct from other natural disasters in that it does not occur abruptly. The phenomenon of drought is characterized by a decrease in precipitation, leading to a decline in water availability. This initial meteorological drought is followed by a subsequent hydrological drought, which in turn results in an agricultural drought (*Mishra* and *Desai*, 2005).

Drought indices (DIs) have been developed as means to monitor and measure the aforementioned negative effects, with DIs being mathematical tools used to determine the severity, duration, and effects of drought events. The application of DIs has been instrumental in the monitoring of drought conditions and the formulation of strategic decisions across a range of domains, including agricultural production and water resources management. The development of DIs has enabled the establishment of drought management and early warning systems, with DIs being used to determine the severity, duration, and effects of drought events. Furthermore, DIs have been identified as a pivotal instrument in the effort to combat climate change, as they offer insights into long-term shifts in climate and drought occurrences, thereby paving the way for the formulation of adaptation strategies (*UNEP*, 2021).The role of DIs in the establishment of drought management and early warning systems, the efficient use of water resources, the determination of agricultural policies, and the development of strategies to combat climate change is critical. The World Meteorological Organization (WMO) has recommended the utilization of the SPI by all national meteorological and hydrological services globally for the characterization of meteorological droughts (*Hayes et al*., 2011; *WMO*, 2012). Additionally, the SPI is proposed for use as a reference index, as it has been demonstrated to facilitate the earlier identification of droughts, to be reliable, to necessitate only precipitation data, and to yield more accurate results (*Morid et al.*, 2006; *Dogan et al.*, 2012; *Mishra* and *Singh*, 2011; *Yacoub* and *Tayfur*, 2017; *Zeybekoglu et al*., 2023). *Tanoglu* (1943) prepared a drought map using temperature and precipitation values throughout Türkiye. *Erinc* (1949) performed a drought analysis by Thorntwaite method by precipitation, temperature, and evaporation records. *Wu et al.* (2001) sought to compare the results of three DIs – the standard precipitation index (SPI), the China-Z index (CZI), and the Z-score index (ZSI) – for China. Their findings revealed that both the CZI and the ZSI yielded results that were analogous to those of the SPI across all temporal ranges. Moreover, the calculations required to determine the CZI and the ZSI were comparatively less onerous than those of the SPI. *Morid et al.* (2006) evaluated seven distinct DIs

(SPI, percent of normal (PN), deciles index (DI), ZSI, CZI, modified China-Z index (MCZI), and effective drought index (EDI)). The study concluded that DIs exhibited a rapid response to precipitation events in specific years but demonstrated temporal and field inconsistencies. Conversely, SPI and EDI were effective in detecting the onset of drought, exhibiting temporal and field consistency, though EDI yielded more sensitive results than SPI. *Bacanli et al.* (2011) conducted an analysis of precipitation and temperature data from 13 selected meteorological stations in the Central Anatolia Region of Türkiye, collected over the period 1965–2006. The evaluation was conducted for all stations. The results of the comparative analysis indicated that the PDSI index indicated more humid conditions than the Erinc and De Martonne indices. *Dogan et al.* (2012) conducted a comparative analysis of six drought indices in the Konya Closed Basin, Türkiye. The drought indices employed included PN, RDDI, ZSI, CZI, SPI, and EDI. In their study, *Shahabfar* and *Eitzinger* (2013) sought to compare and evaluate six meteorological drought indices –PN, SPI, CZI, MCZI, ZSI, and the De Martonne aridity index (I) – with a view to assessing the spatio-temporal dynamics of droughts in six climatic regions in Iran. *Jain et al.* (2015) undertook a comparative analysis of SPI, EDI, ZSI, CZI, rainfall departure (RD), and rainfall decile based drought index (RDDI), with the objective of ascertaining the suitability of indices in districts susceptible to drought in the Ken River Basin in central India. The findings of this study indicated a strong correlation between DIs at equivalent time scales. *Tadic et al.* (2015) undertook an analysis of five drought identification methods (SPI, DI, percent of normal precipitation (PNPI), rainfall anomaly index (RAI), and threshold level method) for continental Croatia. This analysis was conducted on 15 weather stations in the period from 1981 to 2011.In a separate study, *Payab* and *Turker* (2019) compared and evaluated the performance of the SPI, RDI, ZSI, CZI, supply and demand drought index (SDDI), and combined China-Z and supply and demand drought index (CZSDDI) in Northern Cyprus. Multiple DIs, including the PN, SPI, ZSI, and EDI, were employed to evaluate the drought conditions in the Wuyuer River Basin, Northeast China, by *Li et al.* (2019). *Katipoglu et al.* (2020) conducted a comparative analysis of five meteorological DIs: SPI, ZSI, RAI, SPEI, and RDI. This analysis was conducted across seasonal and annual time scales to monitor drought. *Boustani* and *Ulke* (2020) compared the drought analysis of the Yeşilırmak River basin between 1970 and 2014 with different indices (PN, DI, RAI, ZSI, CZI, MCZI, and SPI) and drought analysis between different time scales. They determined that the best index and time for the basin was SPI and 12-month scale. *Salvacion* (2021) identified drought characteristics by SPI and SPEI for the Philippines. In a related study, *Dalkilic et al.* (2021) utilized statistical analysis to calculate and evaluate four DIs (Aridity Index; PNI; SPEI; SPI) to assess the drought status of the Konya Closed Basin. *Sridhara et al.* (2021) utilized precipitation data to evaluate five DIs: the deciles index (DI), PN, CZI, ZSI, and SPI. The researchers employed monthly total precipitation data to

ascertain drought occurrences in the period 1967–2017 across diverse talukas in the Chitradurga district of Karnataka, India. The assessment revealed that the performances of SPI, CZI, and ZSI were similar in identifying drought. *Sa'adi et al.* (2022) evaluated the performance of several rain-based meteorological DIs for the Johor River Basin in Malaysia from 1970 to 2015. The indices evaluated included the RAI, SPI, CZI, PN, DI, and ZSI. *Singh et al.* (2022) compared the performance of seven DIs (SPI, CZI, MCZI, PNI, DI, RAI, and ZSI) in identifying meteorological droughts in the Betwa River basin, India. *Zeybekoglu et al.* (2023) sought to determine the drought conditions that prevailed at stations selected from the Yesilirmak Basin in Türkiye between 1970 and 2014. To this end, they employed a range of indices, including the ZSI, the CZI, the MCZI, and the SPI. The findings indicated that the indices exhibited congruent results and that SPI identified drought conditions earlier than the other indices. *Gumus* (2023) conducted a comparative analysis of drought characteristics across diverse climates and geographical regions in Türkiye. This analysis employed the SPI, utilizing the precipitation parameter, and the SPEI, which is derived by adding the Potential Evaporation (PET) values to precipitation from 1970 and 2021. In a related study, *Sener* and *Davraz* (2024) compared the performance of six DIs (SPI, PNI, DI, CZI, RAI, and ZSI) in the Egirdir Lake Basin in Türkiye. In their study, *Simsek et al.* (2024) sought to evaluate the meteorological drought of the Black Sea region in the north of Türkiye. To this end, they employed the SPI and RDI methods, undertaking a comparative analysis across diverse temporal scales. The meteorological parameters recorded from 28 stations between 1965 and 2019 were subjected to analysis, resulting in a high correlation coefficient of 97.8%, 97.6%, and 97.3% for the 3-, 6-, and 12-month time scales, respectively, between the SPI and RDI in the evaluation of meteorological drought in the Black Sea region.

Türkiye is located between the temperate and subtropical zones. The country's geographical characteristics, including its proximity to the sea, the presence of mountains, and the diversity of its landforms, have resulted in the diversification of its climates. The coastal regions experience a more temperate climate, influenced by the sea, while the interior is characterized by a continental climate, due to the influence of the North Anatolian and Taurus mountains (*Atalay*, 1997; *Sensoy et al.*, 2007). The transition climate between the Black Sea region and the continental climate is characterized by the following features: (a) The summers are less arid than in the continental climate and less rainy than in the Black Sea climate. (b) The winters are less mild than in the Black Sea climate and less harsh than in the continental climate.

The present study investigates the occurrence of drought conditions in Amasya, a region situated in the transition zone between the Black Sea and continental climates in Türkiye, using three precipitation-based DIs: SPI, CZI, and MCZI. To this end, precipitation records from Amasya and Merzifon rainfall stations spanning the period 1964–2023 were investigated in order to make a comparative analysis of these indices. The objective of this research is to quantify

drought on an annual basis, thereby facilitating a more profound comprehension of the drought patterns that characterize it. The present study has therefore been designed with the following objectives in mind: (1) to examine the spatial variation of meteorological drought characteristics, (2) to determine the important dry and wet years, (3) to determine the magnitude, duration and frequency for dry/wet years, (4) to examine the performance of DIs comparatively, and (5) to identify an appropriate drought index. The present paper is composed of four sectionss. Section 1 and 2 provide a detailed exposition of the study area, the sources of data, and the analysis method utilized in the study. Section 3 is concerned with the evaluation of the findings obtained as a result of the analyses. The final section of the paper presents the conclusion of the study.

2. Material and methodologies

2.1. Study area

Amasya's geographical location in the inner part of the Central Black Sea region of Türkiye results in a transitional climate that exhibits characteristics of both the Black Sea climate and the continental climate. This transitional climate is characterized by the influence of the post-Black Sea climate, with summers that are less arid than in the continental climate and less rainy than in the Black Sea climate. Conversely, winters are not as mild as in the Black Sea climate and are not as harsh as in the continental climate. This results in a transitional climate that is situated between the continental climate and the Black Sea climate. Precipitation data were recorded at Amasya and Merzifon for the 1964–2023 period by the Turkish State Meteorological Service (TSMS) in the Black Sea Region of Türkiye. The list of stations is given in *Table 1*, together with their geographical and meteorological details. The localization of stations used in the study are shown in *Fig 1*. Furthermore, *Fig. 2* illustrates the precipitation time series of the stations.

Fig. 1. The geographical and topographical situation of the study area.

Table 1. Basic characteristics of the stations: ID, geographical coordinates, and precipitation records

ID	Name	Latitude(oN)	Longitude(oE)	P_{mean}(mm/year)	P_{min}(mm/year)	P_{max}(mm/year)
17085	Amasya	40.88	35.46	461.53	293.40	681.20
17082	Merzifon	40.67	35.84	432.10	225.10	703.30

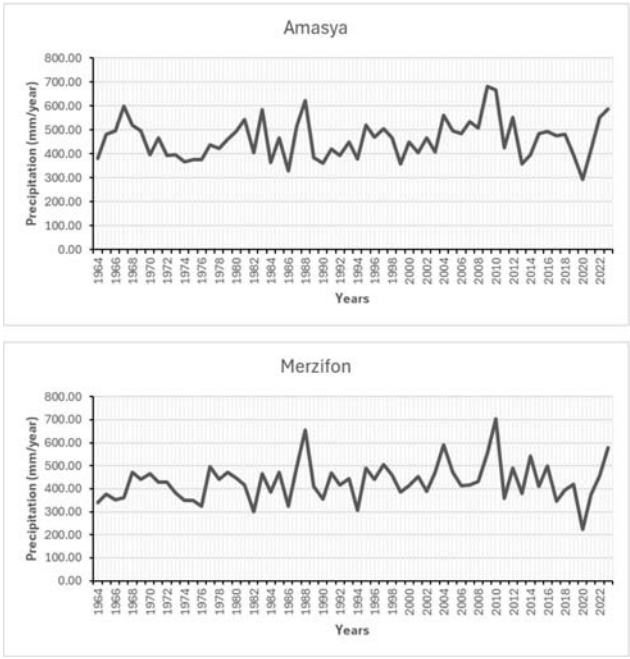

Fig. 2. Precipitation time series for stations utilised in this study.

2.2. Standardized precipitation index (SPI)

The SPI is predicated exclusively on precipitation data developed by *McKee et al.* (1993), which is extensively utilized on a global scale. It serves as a valuable instrument for the identification of drought occurrences across diverse geographical regions. The calculation of the SPI is initiated by the determination of the probability distribution function. According to a study conducted by *McKee et al.* (1995), gamma family functions are the optimal probability distribution functions for the fitting of precipitation data, as it is outlined below.

$$g(x) = \frac{1}{\beta^{\alpha}\Gamma(\alpha)} x^{\alpha-1} e^{\frac{-x}{\beta}}, \quad (1)$$

where $\Gamma(\alpha)$ denotes the gamma function, x is the precipitation amount, $\alpha > 0$ is the shape parameter, and $\beta > 0$ is the scale parameter. The parameters of the gamma probability density function are determined using the maximum likelihood method, with this being performed separately for each station and time scale:

$$\Gamma(\alpha) = \int_0^{\infty} y^{\alpha-1} e^{-y} dy, \quad (2)$$

$$\alpha = \frac{1}{4A}\left(1 + \sqrt{1 + \frac{4A}{3}}\right); \beta = \frac{\overline{x}}{\alpha}; A = \ln(\overline{x}) - \sum \frac{\ln(x)}{n}, \quad (3)$$

where n denotes the number of precipitation observations. A mathematical cumulative probability function can accurately describe the distribution of precipitation at stations, as it is follows:

$$G(x) = \int_0^x g(x)dx = \frac{1}{\beta^{\alpha}\Gamma(\alpha)} \int_0^x x^{\alpha-1} e^{\frac{-x}{\beta}} dx. \quad (4)$$

In the event that the gamma function is undefined for $x = 0$, and the precipitation distribution is zero, the cumulative probability is obtained as:

$$H(x) = q + (1 - q)G(x), \quad (5)$$

where q denotes the probability of a zero. Subsequently, the cumulative probability $H(x)$ is converted to the standard normal distribution, thereby yielding the SPI. According to *Wu et al.* (2007), the calculation of the SPI is presented based on the following equations:

$$0 < H(x) < 0.5; \text{ SPI} = -\left(t - \frac{c_0 + c_1 t + c_2 t^2}{1 + d_1 t + d_2 t^2 + d_3 t^3}\right); t = \sqrt{ln\left(\frac{1}{(H(x))^2}\right)}, \quad (6)$$

$$0.5 < H(x) < 1.0; \text{ SPI} = +\left(t - \frac{c_0 + c_1 t + c_2 t^2}{1 + d_1 t + d_2 t^2 + d_3 t^3}\right), \quad (7)$$

whrer c_0, c_1, c_3, d_1, d_2, and d_3 are coefficients whose values are: c_0 = 2.515517, c_1=0.802853, c_2 = 0.010328, d_1 = 1.432788, d_2 = 0.189269, and d_3 = 0.001308. The drought classification according to SPI is given in *Table 2*.

2.3. China-Z index (CZI) and modified China-Z index (MCZI)

In the early 1990s, the China-Z index (CZI) and modified China-Z index (MCZI) were introduced to the National Meteorological Centre of China as a drought calculation index (*Ju et al.*, 1997; *Hong et al.*, 2001; *Kassaye et al.*, 2021). The CZI and MCZI are associated with the Wilson-Hilferty cube root transformation (*Wilson* and *Hilferty*, 1931; *Kendall* and *Stuart*, 1977; *Wu et al.*, 2001). The calculation of the MCZI is analogous to that of the CZI; however, the median value (υ) of the series is taken into account rather than the mean value ($\emptyset$) of the series (*Morid et al.*, 2006). In the event that precipitation is assumed to follow the Pearson type III distribution, the following equation computes the CZI/MCZI (*Wu et al.*, 2001; *Morid et al.*, 2006; *Dogan et al.*, 2012; *Jain et al.*, 2015; *Singh et al.*, 2022):

$$CZI = \frac{6}{C_s}\left(\frac{C_s}{2}\varphi_j + 1\right)^{1/3} - \frac{6}{C_s} + \frac{C_s}{6},\ C_s = \frac{\sum_{j=1}^{n}\left(x_j - \overline{\emptyset}\right)^3}{n * \sigma^3},\ \varphi_j = \frac{x_j - \overline{\emptyset}}{\sigma}, \qquad (8)$$

where C_s denotes the coefficient of skewness, n signifies the total number of months within the specified record, φ is a standardized variable (also termed the Z-score), x_j represents the precipitation during a specified period, and $\emptyset$ indicates the mean value. *Table 2* shows the drought classification based on MCZI.

Table 2. Classification and value ranges of DIs

Symbol	Category	SPI/CZI/MCZI
EW	Extremely wet	≥2.00
VW	Very vet	1.50 to 1.99
MW	Moderately wet	1.00 to 1.49
N	Normal	-0.99 to 0.99
MD	Moderately dry	-1.49 to -1.00
SD	Severely dry	-1.99 to -1.50
ED	Extremely dry	≤-2.00

3. Results and discussion

The present study focuses on investigating the meteorological drought of Amasya, which is located in the transition zone between the Black Sea and continental climates in the Black Sea region of Türkiye, through precipitation-based DIs. The precipitation records from 1964 to 2023 at Amasya and Merzifon stations within the region were analyzed employing the SPI, CZI, and MCZI indices. Moreover, a comparative evaluation of the performance of DIs was conducted. The SPI, CZI, and MCZI were calculated at annual scales for Amasya and Merzifon, as illustrated in *Fig. 3*. The dry and wet years, as determined by the DIs and their frequency distribution, are presented in *Table 3*. As indicated in *Table 4*, the correlation coefficient (R) for the SPI-CZI, SPI-MCZI, and CZI-MCZI for Amasya and Merzifon are also presented. Furthermore, scatter diagrams were prepared for the stations in order to examine the agreement between the indices (*Fig. 4*).

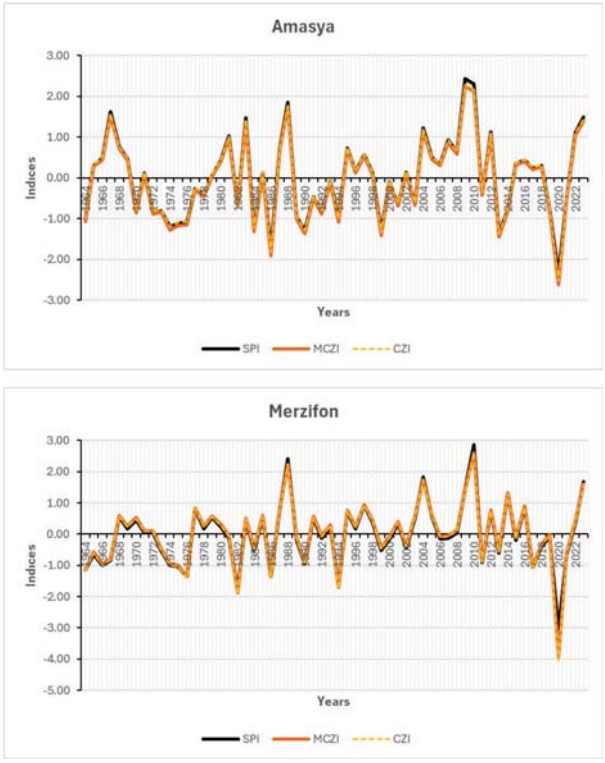

Fig. 3. Temporal variation of all DIs utilized in this study.

As demonstrated in *Fig. 3* and *Table 3*, the SPI, CZI, and MCZI results of Amasya and Merzifon reveal significant findings. The CZI results for Amasya demonstrate that the number of dry and wet years is equal, with 10 years classified as dry and 10 years classified as wet. Conversely, the SPI and MCZI results indicate that the number of dry years exceeds the number of wet years, with 11 and 10 years, respectively, classified as dry. In wet years, the SPI classified 10 years and the MCZI classified 9 years as wet. In Merzifon, the number of dry years exceeds the number of wet years, according to all DIs. While the CZI and SPI each define 10 years as dry, the MCZI defines 7 years as dry. In wet years, all DIs define 6 years as wet.

The all DIs showed dry conditions in 1974-1976, 1984, 1986, 1990, 1994, 1999, 2013, and 2020 for Amasya. The driest year for the SPI was -2.35 for 2020, while the CZI and MCZI for the same year in Cankiri were -2.52 and -2.63, respectively. According to the DIs results in Amasya, the MD conditions happened in 1974-1976, 1984, 1990, 1999, and 2013. On the other hand 1964 was distinguished as SD by MCZI and SPI. Also just CZI distinguished the year 1981 as MD. The year 2020 was identified as ED condition by all DIs. 1967, 1983, 1988, 2004, 2009-2010, 2012, and 2022-2023 were determined as wet years by all DIs. The EW condition happened in 2009 and 2010. The MW years include 1983, 2004, 2012, and 2022-2023. Also just SPI and CZI distinguished the year 1981 as MW. The years 1967 and 1988 showed VW conditions. In 2009, the peak value of the SPI was 2.44, whereas the corresponding CZI and MCZI were 2.29 and 2.13, respectively.

The SPI, CZI, and MCZI indicated that years 1964, 1976, 1982, 1986, 1994, 2017, and 2020 have droughts in Merzifon. The driest year for the SPI was -3.04 for 2020, while the CZI and MCZI for the same year were -4.04 and -3.93, respectively. All DIs indicate that the MD conditions occurred in 1964, 1976, 1986, and 2017. Unlike the MCZI and SPI, CZI identified the years 1966 and 1974-1975 as MD at Merzifon. All DIs indicated that 1982 and 1994 were SD years, while 2020 was ED year. According to the all DIs, wet conditions occurred in 1988, 2004, 2009-2010, 2014 and 2023. MW conditions happened in 2009 and 2014. The years 2004 and 2023 were identified as VW conditions. Unlike the other indices, SPI identified the year 2016 as MW at Merzifon. The EW condition occurred in 1988 and 2010. In 2010 the peak value of the SPI was 2.86, whereas the corresponding CZI and MCZI were 2.60 and 2.62, respectively.

The findings of the arid classes presented in *Table 3* for the meteorological stations in Amasya and Merzifon determined MD frequencies of 15% and 11.67% for SPI, 11.67% for CZI, and 16.67% and 6.67% for MCZI, respectively. In Merzifon, the MD frequencies of the SPI and CZI methods are identical, and the years belonging to this drought class are also congruent. The SD frequencies for Amasya and Merzifon were found to be 1.67% and 3.33% for SPI and MCZI, respectively, and 3.33% for CZI. In Amasya, the SD frequencies of the SPI and MCZI methods are found to be identical, and the years (e.g., 1986) belonging to this drought class are also congruent. Similarly, in Merzifon, the SD frequencies of all DIs are found to be identical, and the years (1982 and 1994) belonging to

this drought class are also congruent. In the Amasya and Merzifon, it has been determined that the ED frequencies of the SPI, CZI, and MCZI methods are identical to 1.37%. Furthermore, the year 2020, which has been designated as belonging to this drought class, corresponds with all DIs.

Table 3. Characteristics of years as detected by DIs

			SPI		CZI		MCZI	
			Years	**Frequency**	**Years**	**Frequency**	**Years**	**Frequency**
Amasya	WET	EW	**2009** 2010	3.33%	**2009** 2010	3.33%	**2009** 2010	3.33%
		VW	1967 1988	3.33%	1967 1988	3.33%	1967 1988	3.33%
		MW	1981 1983 2004 2012 2022 2023	10%	1981 1983 2004 2012 2022 2023	10%	1983 2004 2012 2022 2023	8.33%
	DRY	MD	1964 1974 1975 1976 1984 1990 1994 1999 2013	15%	1974 1975 1976 1984 1990 1999 2013	11.67%	1964 1974 1975 1976 1984 1989 1990 1994 1999 2013	16.67%
		SD	1986	1.67%	1986 1994	3.33%	1986	1.67%
		ED	**2020**	1.67%	**2020**	1.67%	**2020**	1.67%
Merzifon	WET	EW	1988 **2010**	3.33%	1988 **2010**	3.33%	1988 **2010**	3.33%
		VW	2004 2023	3.33%	2004 2023	3.33%	2004 2023	3.33%
		MW	2009 2014	3.33%	2009 2014	3.33%	2009 2014	3.33%
	DRY	MD	1964 1966 1974 1975 1976 1986 2017	11.67%	1964 1966 1974 1975 1976 1986 2017	11.67%	1964 1976 1986 2017	6.67%
		SD	1982 1994	3.33%	1982 1994	3.33%	1982 1994	3.33%
		ED	**2020**	1.67%	**2020**	1.67%	**2020**	1.67%

As it is demonstrated in *Table 3*, the results of the wetland classes indicate that Amasya and Merzifon exhibited the following MW frequency for the SPI: 10% and 11.67%, for the CZI: 10.00% and 3.33%, and for the MCZI: 8.33% and 3.33%, respectively. In Amasya, the MW frequencies of the SPI and CZI methods are found to be identical, and the years belonging to this drought class are also congruent. Similarly, in Merzifon, the MW frequencies of all DIs are found to be identical, and the years (2009 and 2014) belonging to this drought class are also congruent. The VW frequencies for Amasya and Merzifon were found to be 1.67% for all DIs. Moreover, the years 1988 and 2020; 2004 and 2023, which have been designated as belonging to this drought class, correspond with SPI, CZI, and MCZI for Amasya and Merzifon, respectively. While the proportional results of the EW are consistent with those of the VW, with 3.33%, it is important to note that the years 2009 and 2010, classified as EW drought class, coincide with the all DIs for Amasya and the years 1988 and 2010 coincide with the all DIs for Merzifon

Table 4. The correlations between all DIs

Years	SPI-CZI	SPI-MCZI	CZI-MCZI
Amasya	0.9991	0.9990	1.0000
Merzifon	0.9911	0.9917	1.0000
Average	0.9951	0.9954	1.0000

As it is illustrated in *Table 4*, the correlation values between all DIs on annual timescales are demonstrated. Amasya and Merzifon exhibit a higher correlation between SPI and CZI with 0.9991 and 0.9911, respectively. They exhibit a stronger correlation between SPI and MCZI with 0.9990 and 0.9917, respectively. The calculation of the CZI and MCZI correlation values (1.0000) indicates a state of complete agreement between the results obtained. Furthermore, as evidenced by the scatter diagrams in *Fig. 3*, the drought indices exhibited a high degree of concordance.

The mean of R values for all combinations were found to be 0.9951 for SPI-CZI, 0.9954 for SPI-MCZI, and 10000 for CZI-MCZI. Following the analysis, it was determined that CZI-MCZI exhibited the maximum R value of 1.0000, while SPI-CZI demonstrated the minimum. A comparison of the correlation values calculated between SPI, which is recommended as the reference index, and CZI and MCZI, was undertaken. The results of this comparison indicated that SPI-CZI has higher correlation values than SPI-MCZI in Amasya. Conversely, in Merzifon, the correlation value of SPI-MCZI was observed to be higher than SPI-CZI. In the context of drought research, the CZI and MCZI methods have been

identified as viable alternatives to the SPI reference index at the Amasya and Merzifon stations, respectively. A thorough examination of the average correlation values reveals that the MCZI method emerges as a better option in comparison to the CZI method across the entire study area.

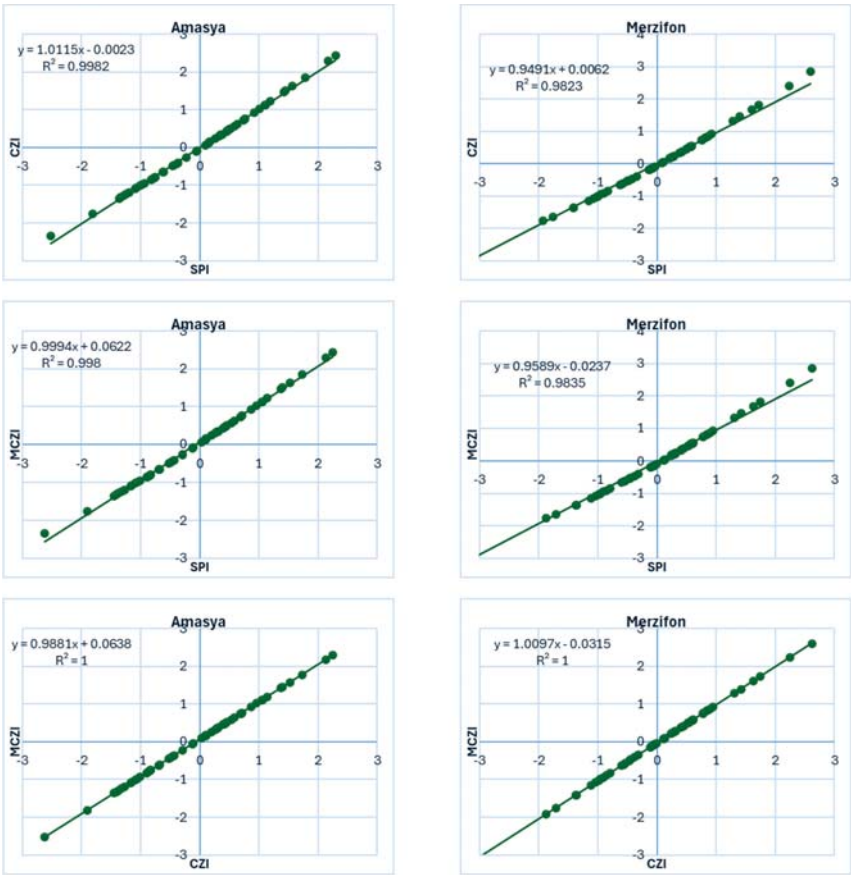

Fig. 4. The scatter diagrams between all DIs in the Amasya and Merzifon.

Drought researches will continue to represent a central focus within the broader field of climate research, both in the present moment and in the future. A substantial body of researches has been conducted employing diverse DIs across various geographical scales, ranging from regional to national, in Türkiye. The results of SPI, CZI, and MCZI demonstrate that Amasya and Merzifon, which are characterized by a transitional climate in the Black Sea region of Türkiye,

experienced drought in 1964, 1974- 1976, 1982, 1984, 1986, 1990, 1999, 2013, 2017, and 2020. *Sirdas* and *Sen* (2003a, b) reported that water resources in certain arid regions of Türkiye would decrease by 10–30% by the middle of the 21st century. Furthermore, they anticipated an increase in the severity, duration and effects of drought in the southern parts of the country, and an increase in the frequency of floods in the northern parts. *Ceylan et al.* (2009) have reported that significant water deficits were recorded in 1927–1928, 1956–1957, 1959, 1970, 1972–1973, 1977, 1982, 1984, 1989–1990, 1994, 2000–2001, and 2006–2007 in Türkiye. *Türkeş et al.* (2009a, b) and *Türkeş* (2014) reported that the most severe and widespread drought events in Türkiye were in 1971–1974, 1983–1984, 1989–1990, 2007–2008, and 2013–2014. *Komuscu* (1999, 2001) asserted that the Black Sea region of Türkiye experienced significant drought conditions between 1990 and 2000. *Sonmez et al.* (2005) reported that significant drought conditions were observed during the late 1980s, with this trend continuing into the late 1990s in the Central Anatolia region of Türkiye. *Bacanli et al.* (2011) provide compelling evidence that the region is still in danger of severe drought in the Central Anatolia Region of Türkiye. *Yetmen* (2014) reported that the central Black Sea in northern Türkiye experienced notable drought conditions during the years 1976–1977, 1982–1983, 1985–1986, 1994, 2001, 2003, and 2007–2008, as indicated by the SPI. *Gumus* and *Algin* (2017) conducted a study of the Seyhan-Ceyhan River basins, located in the south of Türkiye, utilising the SPI to identify the most protracted meteorological droughts. These were observed to be 1971–1973, 1988–1990 and 2003–2005. *Bacanli* and *Aksan* (2019) observed that the Mediterranean region of Türkiye experienced a period of drought in the early 1970s and early 1990s. *Altin et al.* (2020) determined that a considerable part of the drought conditions experienced in the Seyhan and Ceyhan River Basins were mild to moderate. Furthermore, *Kumanlioglu* and *Fistikoglu* (2019) identified a protracted drought period between 1984 and 1996 using the SPI for the upper Gediz basin. Furthermore, 1961, 1987, 2006, 2008, 2011, and 2014 were designated as severe drought years. In addition, *Dikici* (2020) analyzed the Asi basin, located in the southern part of Türkiye. This basin was the focus of studies conducted using DI, SPI, SPEI, and SRI. These studies revealed the effects of drought in the years 1973–1974, 1989–1991, 1993–1994, 2000–2001, 2004–2005, 2014, and 2016. Concurrently, *Katipoglu* and *Acar* (2021) and *Katipoglu et al.* (2021) reported that the most severe meteorological droughts were observed in the years 1989 and 2012–2017 in the Euphrates basin, which encompasses a substantial expanse in the east and southeast of Türkiye. *Simsek et al.* (2024) reported that the coastal strip of the Black Sea region has been impacted by prolonged droughts, particularly following the year 2010. The findings obtained from this study are consistent with those reported in the extant literature.

4. Conclusion

The present study investigates the performance of three precipitation-based drought indices (SPI, CZI, and MCZI) in order to determine the suitable indices for the study area. This investigation is based on precipitation records from the Amasya and Merzifon meteorological stations between 1964 and 2023, which represent a transitional climate zone within the Black Sea region of Türkiye. The following years have been identified as being significant in terms of drought: 1964, 1974–1976, 1982, 1984, 1986, 1990, 1999, 2013, 2017, and 2020. Correlation values were obtained between SPI-CZI, SPI-MCZI, and CZI-MCZI, with graphs that were found to be compatible with each other. The relation of the DIs with SPI, which was selected as the reference index, was investigated and evaluated. In this particular instance, the most compatible index with SPI is MCZI, which serves as a commendable alternative to SPI in drought assessment in the Amasya and Merzifon regions. The study's findings underscore the importance of utilizing CZI and MCZI in place of SPI for the purpose of enhancing drought forecasting and evaluating prevailing climatic conditions in transitional climate zones. The two DIs (CZI and MCZI), which were successfully implemented to identify droughts in the transitional climate zone, are recommended for use in detailed drought analyses to be conducted in the basin as an alternative to SPI. In future studies, it is recommended that the region has to be evaluated with DIs that take into account different parameters such as temperature, evaporation, and satellite data, together with precipitation-based DIs for drought monitoring and assessment purposes. Furthermore, the temporal trends of climate parameters, including precipitation, temperature, evaporation, and potential drought conditions, can be analyzed using climate projection data. This studies can provide policy makers and decision makers with the necessary information to implement suitable plans and strategies for the region, both in the present and in the future.

Acknowledgements: The author wishes to express their gratitude to the Turkish State Meteorological Service for the provision of meteorological data. The author wishes to express gratitude to the General Directorate of Mapping for assistance in the preparation of the cartographic materials. The author would also like to express their gratitude to the reviewers, whose constructive criticisms have resulted in significant improvement to the manuscript.

Data availability: Rainfall data provided by the Turkish State Meteorological Service (TSMS) can be purchased from “https://mevbis.mgm.gov.tr/ mevbis/ui/index.html#/Workspace”, (Purchase numbers: 20240527308A and 202405276447).

Declaration of Competing Interest: The author declares that I have no known competing financial interests or personal relationships that could have appeared to influence the work reported in this paper.

Authorship Contribution Statement: The author contributed solely to all aspects of this study, including conceptualization, methodology, data analysis, writing, and revision of the manuscript.

References

Adib, A., Soleimani, M., Ashrafi S.M., Lotfirad, M., Sofla, M.S.D.S., and *Liaghat, A.*, 2024: Monitoring annual meteorological drought in arid and semi-arid watersheds by SPI12 drought index and spatial autocorrelation pattern analysis: a case study of the Khuzestan province, Southwest Iran. Sustain. *Water. Resour. Manag. 10*, 160. https://doi.org/10.1007/s40899-024-01142-y

Adisa, O.M., Masinde, M., Botai, J.O., and *Botai, C.M.*, 2020: Bibliometric analysis of methods and tools for drought monitoring and prediction in Africa. *Sustainability 12(16),* 6516. https://doi.org/10.3390/su12166516

Altın, T.B., Sarış, F., and *Altın, B.N.*, 2020: Determination of drought intensity in Seyhan and Ceyhan River Basins, Turkey, by hydrological drought analysis. *Theor. Appl. Climatol. 139*, 95–107. https://doi.org/10.1007/s00704-019-02957-y

Atalay, İ., 1997: *Türkiye Coğrafyası,* İzmir, Ege Üniversitesi Basımevi (in Turkish).

Bacanli, U.G., Dikbas F., and *Baran T.*, 2011: Meteorological drought analysis case study: Central Anatolia. *Desalination and Water Treatment 26(1–3),* 14-23. https://doi.org/10.5004/dwt.2011.2105

Bacanli, U.G. and *Aksan, G.N.*, 2019: Drought analysis in Mediterranean Region. *Pamukkale University Journal of Engineering Sciences 25(6),* 665-671. https://doi.org/10.5505/pajes.2019.64507

Boustani, A. and *Ulke, A.K.*, 2020: Investigation of meteorological drought indices for environmental assessment of Yesilirmak region. Journal of Environmental Treatment Techniques 8(1), 374-381.

Ceylan, A., Turgu, E., Inal, I., Mollamahmutoglu, A., and *Aydoğan, A.*, 2009: Assessment of Drought Events Observed In Recent Years In Turkey. *Su Kaynakları 2(1),* 1-11 (in Turkish).

Dalkilic, H.Y., Baycinar, M., and *Samui, P.*, 2021: Evaluation of combined use of drought indices in the case of Konya Closed Basin. *Int. J. Global Warming 23(2),* 169–190. https://doi.org/10.1504/IJGW.2021.112895

Dikici, M., 2020: Drought analysis with different indices for the Asi Basin (Turkey). *Sci. Rep. 10*, 1–12. https://doi.org/10.1038/s41598-020-77827-z

Dogan, S., Berktay, A., and *Singh, V.P.*, 2012: Comparison of multi-monthly rainfall-based drought severity indices, with application to semi-arid Konya closed basin, Turkey. *J. Hydrol. 470–471,* 255–268. https://doi.org/10.1016/j.jhydrol.2012.09.003

Erinc, S., 1949: The climates of Turkey according to Thornthwaite's classifications. *Ann. Assoc. Amer. Geograph. 39(1),* 26–46.

Gumus, V., 2023: Evaluating the effect of the SPI and SPEI methods on drought monitoring over Turkey. *J. Hydrol. 626*, 130386. https://doi.org/10.1016/j.jhydrol.2023.130386

Gumus, V. and *Algin, H.M.*, 2017: Meteorological and hydrological drought analysis of the Seyhan-Ceyhan River basins, Turkey. *Meteorol. Appl. 24(1),* 62–73. https://doi.org/10.1002/met.1605

Hayes, M., Svoboda, M., Wall, N., and *Widhalm, M.*, 2011: The Lincoln Declaration on Drought Indices: Universal Meteorological Drought Index Recommended. *Bull. Amer. Meteorol. Soc. 92(4),* 485–488. https://doi.org/10.1175/2010BAMS3103.1

Hong, W., Michael, J.H., Albert, W., and *Qi, H.*, 2001: An evaluation of the standardized precipitation index, the china-z index and the statistical z-score. *Int. J. Climatol. 21*, 745–758. https://doi.org/10.1002/joc.658

Jain, V.K., Pandey, R.P., Jain, M.K., and *Byun, H.R.*, 2015: Comparison of drought indices for appraisal of drought characteristics in the Ken River Basin. *Weather Climate Extr. 8*, 1–11. https://doi.org/10.1016/j.wace.2015.05.002

Jenkins, K., and *Warren, R.*, 2015: Quantifying the impact of climate change on drought regimes using the Standardised Precipitation Index. *Theor. Appl. Climatol. 120*, 41–54. https://doi.org/10.1007/s00704-014-1143-x

Ju, X., Yang, X., Chen, L., and *Wang, Y.*, 1997: Research on determination of indices and division of regional flood/drought grades in China. *J. Appl. Meteor. Sci. 8(1),* 26–33 (in Chinese).

Kassaye, A.Y., Shao, G., Wang, X., and *Wu, S.*, 2021: Quantification of drought severity change in Ethiopia during 1952–2017. *Environ. Dev. Sustain. 23*, 5096–5121. https://doi.org/10.1007/s10668-020-00805-y

Katipoglu, O.M., and *Acar, R.*, 2021: Determination of Meteorological and Hydrological Drought Maps with Various Interpolation Methods in the Euphrates Basin. *J. Nat. Hazards Environ. 7(2)*, 298–317 (in Turkish). https://doi.org/10.21324/dacd.853893

Katipoglu, O.M., *Acar, R.*, and *Sengul, S.*, 2020: Comparison of meteorological indices for drought monitoring and evaluating: a case study from Euphrates basin, Turkey. *J. Water Climate Change 11(S1)*, 29–43. https://doi.org/10.2166/wcc.2020.171

Katipoglu, O.M., *Acar, R.*, and *Senocak, S.*, 2021: Spatio-temporal analysis of meteorological and hydrological droughts in the Euphrates Basin, Turkey. *Water Supply 21(4)*, 1657–1673. https://doi.org/10.2166/ws.2021.019

Kendall, M.G., and *Stuart, A.*, 1977: The Advanced Theory of Statistics: Distribution theory. Macmillan.

Komuscu, A.U., 1999: Using the SPI to analyze spatial and temporal patterns of drought in Turkey. *Drought Network News (1994-2001) 11*, 7-13

Komuscu, A.U., 2001: An analysis of recent drought conditions in Turkey in relation to circulation patterns. *Drought Network News (1994-2001) 13(2-3)*, 5–6.

Kumanlioglu, A., and *Fistikoglu, O.*, 2019: Meteorological drought analysis of Upper Gediz basin precipitations. *DEUFMD 21(62)*, 509–523 (in Turkish). https://doi.org/10.21205/deufmd.2019216216

Li, F., *Li, H.*, *Lu, W.*, *Zhang, G.*, and *Kim, J-C.*, 2019: Meteorological drought monitoring in Northeastern China using multiple indices. *Water 11(1)*, 1-17. https://doi.org/10.3390/w11010072

McKee, T.B., *Doesken, N.J.*, and *Kleist, J.*, 1993: The relationship of drought frequency and duration to time scales. 8th Conference on Applied Climatology, Anaheim, CA, USA, January, 179–184

McKee, T.B., *Doesken, N.J.*, and *Kleist, J.*, 1995: Drought monitoring with multiple time scales. 9th Conference on Applied Climatology, Dallas, Texas, USA, January, 233–236

Mishra, A.K. and *Desai, V.R.*, 2005: Drought forecasting using stochastic models. *Stochastic Environ. Res. Risk Assess. 19*, 326-339. https://doi.org/10.1007/s00477-005-0238-4

Mishra, A.K. and *Singh, V.P.*, 2011: Drought modeling - A review. *J. Hydrology 403*, 157–175. https://doi.org/10.1016/j.jhydrol.2011.03.049

Morid, S., *Smakhtin, V.*, and *Moghaddasi, M.*, 2006: Comparison of seven meteorological indices for drought monitoring in Iran. *Int. J. Climatol. 26*, 971–985. https://doi.org/10.1002/joc.1264

Payab, H. and *Turker, U.*, 2019: Comparison of standardized meteorological indices for drought monitoring at northern part of Cyprus. *Environ. Earth. Sci. 78(10)*, 309–327. https://doi.org/10.1007/s12665-019-8309-x

Sa'adi, Z., *Yusop, Z.*, and *Alias, N.E.*, 2022: Inter-comparison on the Suitability of Rain-Based Meteorological Drought in Johor River Basin, Malaysia. *KSCE J. Civ. Eng. 26*, 2519–2537. https://doi.org/10.1007/s12205-022-1481-7

Salvacion, A.R., 2021: Mapping meteorological drought hazard in the Philippines using SPI and SPEI. *Spat. Inf. Res. 29*, 949–960. https://doi.org/10.1007/s41324-021-00402-9

Sener, E. and *Davraz, A.*, 2024: Comparison of drought indices in the analysis of temporal and spatial changes of climatic drought events: a case study in the Egirdir Lake basin (Isparta/Turkey). *Nat. Hazards 120*, 12817–12849. https://doi.org/10.1007/s11069-024-06711-0

Sensoy, S., *Demircan, M.*, *Ulupinar Y.*, and *Balta, I.*, 2007: *Türkiye İklimi*. Turkish State Meteorological Service (in Turkish).

Shahabfar, A. and *Eitzinger, J.*, 2013: Spatio-Temporal Analysis of Droughts in Semi-Arid Regions by Using Meteorological Drought Indices. *Atmosphere 4(2)*, 94-112. https://doi.org/10.3390/atmos4020094

Simsek, O., *Yildiz-Bozkurt, S.*, and *Gumus, V.*, 2024: Analysis of meteorological drought with different methods in the Black Sea region, Turkey. *Acta Geophys. 72*, 1927–1943. https://doi.org/10.1007/s11600-023-01099-0

Singh, U., *Agarwal, P.*, and *Sharma, P.K.*, 2022: Meteorological drought analysis with different indices for the Betwa River basin, India. *Theor. Appl. Climatol. 148*, 1741–1754. https://doi.org/10.1007/s00704-022-04027-2

Sirdas, S., and *Sen, Z.*, 2003a: Meteorological drought modelling and application to Turkey. *İTÜDERGİSİ/d 2(2)*, 95–103 (in Turkish).

Sirdas, S., and *Sen, Z.*, 2003b: Spatio-temporal drought analysis in the Trakya region, Turkey. *Hydrol. Sci. J. 48(5),* 809–820. https://doi.org/10.1623/hysj.48.5.809.51458

Sonmez, F.K., Komuscu, A.U., Erkan, A., and *Turgu E.*, 2005: An Analysis of Spatial and Temporal Dimension of Drought Vulnerability in Turkey Using the Standardized Precipitation Index. *Nat. Hazards 35,* 243–264. https://doi.org/10.1007/s11069-004-5704-7

Sridhara, S., Chaithra, G.M., and *Gopakkali, P.*, 2021: Assessment and monitoring of drought in Chitradurga district of Karnataka using different drought indices. *J. Agrometeorol. 23*, 221–227. https://doi.org/10.54386/jam.v23i2.72

Tadić, L., Dadić, T., and *Bosak, M.*, 2015: Comparison of different drought assessment methods in continental Croatia. *GRAĐEVINAR 67(1),* 11–22. https://doi.org/10.14256/JCE.1088.2014

Tanoglu, A., 1943. Indices D'aridite De La Turquie. *Turkish Geographical Review 1,* 36-41.

Turkes, M., 2014: Analysis of reasons of 2023-2024 drought and climatological/meteorological in Turkey. *Konya Toprak Su Dergisi 2,* 20-34.

Turkes, M., Akgundüz, A.S., and *Demirors, Z.*, 2009a: Drought periods and severity over the Konya Sub-region of the Central Anatolia Region according to the Palmer drought index. *Turk. J. Geograph. Sci. 7,* 129–144 (in Turkish). https://doi.org/10.1501/Cogbil_0000000102

Turkes, M., Koc, T., and *Saris, F.*, 2009b: Spatiotemporal variability of precipitation total series over Turkey. *Int. J. Climatol. 29,* 1056–1074. https://doi.org/10.1002/joc.1768

UNEP, (2021: *United Nations Environment Programme*: Global environment outlook 6: Healthy planet, healthy people. UNEP.

Wilson, E.B. and *Hilferty, M.M.*, 1931: The distribution of chi-square. *Proc. Natl. Acad. Sci. USA 17(12),* 684. https://doi.org/10.1073/pnas.17.12.684

WMO, 2012: *World Meteorological Organization*: Standardized Precipitation Index User Guide. (*M. Svoboda, M. Hayes* and *D. Wood*). WMO-No. 1090. Geneva. ISBN 978-92-63-11091-6. 16p.

Wu, H., Hayes, M.J., Weiss, A., and *Hu, Q.*, 2001: An evaluation of the Standardized Precipitation Index, the China Z Index and the statistical Z Score. *Int. J. Climatol. 21(6),* 745–758. https://doi.org/10.1002/joc.658

Wu, H., Svoboda, M.D., Hayes, M.J., Wilhite, D.A., and *Wen, F.*, 2007: Appropriate application of the standardized precipitation index in arid locations and dry seasons. *Int. J. Climatol 27(1),* 65-79. https://doi.org/10.1002/joc.1371

Yacoub, E. and *Tayfur, G.*, 2017: Evaluation and assessment of meteorological drought by different methods in Trarza Region, Mauritania. *Water Res. Manage. 31,* 825–845. https://doi.org/10.1007/s11269-016-1510-8

Yetmen, H., 2014: Characteristics of drought events in the Middle Black Sea region. TÜCAUM VIII. Coğrafya Sempozyumu, Ankara, Turkey, 87–96 (in Turkish).

Zeybekoglu, U., Hezarani, A.B., and *Ulke Keskin, A.*, 2023: Comparison of four precipitation based meteorological drought indices in the Yesilirmak Basin Turkey. *Időjárás 127(1),* 123–142. https://doi.org/10.28974/idojaras.2023.1.7

DOI:10.28974/idojaras.2026.2.3

IDŐJÁRÁS

Quarterly Journal of the HungaroMet Hungarian Meteorological Service
Vol. 130, No. 2, January – March, 2026, pp. 135–150

Study on the performance of WRF 4DVAR with GSMaP_NOW rainfall assimilation in forecasting heavy rainfall over the Maritime Continent

Achmad Fahruddin Rais[1*], **Giarno**[2], **Sayful Amri**[2], **Muflihah**[3], **Nurtiti Sunusi**[4], **Didiharyono**[5], **Agustina Rachmawardani**[6], **Hariyanto**[6], **Bono Pranoto**[1], **Muhammad Syamsudin**[3], and **Bagus Satrio Utomo**[3]

[1]*Research Centre of Limnology and Water Resource, Research and Innovation Agency, Indonesia*

[2]*Climatology Study Program, School of Meteorology, Climatology and Geophysics, Indonesia*

[3]*Balai Besar Wilayah IV, Agency for Meteorology, Climatology and Geophysics, Indonesia*

[4]*Departemen of Statistic, Hasanuddin University, Indonesia*

[5]*Research Center for Computing, Research and Innovation Agency, Indonesia*

[6]*Instrumentation Study Program, School of Meteorology, Climatology and Geophysics, Indonesia*

**Corresponding author E-mail: achm050@brin.go.id*

(Manuscript received in final form on December 25, 2025)

Abstract— This study evaluated the performance of the Weather Research and Forecasting (WRF) model with Four-Dimensional Variational (4DVar) data assimilation using the Global Satellite Mapping of Precipitation (GSMaP_NOW). Several verification metrics, including the root mean square error (RMSE), bias Score, equitable threat score (ETS), - fractional bias score (FBS), and fractional skill score (FSS) were employed in the assessment. The results demonstrated that 4DVar improved the accuracy of vertical velocity and specific humidity predictions at mid and upper levels, as well as the enhanced heavy rainfall forecasting. Spatially, 4DVar was able to increase specific humidity and vertical velocity in lowland areas, leading to higher rainfall in those regions. Future studies should investigate the assimilation of additional conventional and satellite observations to further enhance forecast accuracy.

Key-words: 4DVar, GSMaP_NOW, Maritime Continent, WRF, rainfall

1. Introduction

The Maritime Continent (MC) is recognized as the region with the highest precipitation in the tropics, mainly due to its status as the area with the longest coastline in the world (*Yamanaka*, 2016). Extensive forests and mountainous terrains also significantly contribute to rainfall generation across the MC (*Ruppert* and *Chen*, 2020). This region's diurnal cycle over land is particularly pronounced (*Argüeso et al.*, 2020). Differential solar heating across land and sea surfaces induces local pressure gradients that drive sea–land breeze circulations. These circulations, combined with orographic lifting and nocturnal downdrafts, constitute the area's primary mechanisms for rainfall formation (*Qian*, 2008). Positioned between the Pacific and Indian Oceans, the weather dynamics of the MC substantially influence the global climate system (*Chen et al.*, 2023).

Heavy precipitation in this region has multidimensional impacts, encompassing environmental, social, economic, and public health domains. Ecologically, extreme rainfall can disrupt ecosystem balance by triggering soil erosion, habitat degradation, and altered hydrological patterns that often result in flash floods (*Trenberth*, 2005; *Li et al.*, 2019). In agriculture, intense rainfall damages crops and reduces yields, particularly for sensitive commodities such as maize, sugarcane, and turmeric, and increases the economic vulnerability of smallholder farmers (*Guo* and *Chen*, 2022; *Muthiah et al.*, 2025). The socio-economic repercussions also extend to infrastructure and construction, where poor drainage systems and rainfall-induced landslides can lead to structural damage and disrupt essential public services (*Jiang* and *Tan*, 2021). Rapid urbanization amplifies flood risks in urban areas by increasing surface runoff volume and shortening rainfall concentration time, thereby intensifying the likelihood of localized flooding (*Huang et al.*, 2011; *Sahoo et al.*, 2020). From a public health perspective, high precipitation is linked to rising waterborne diseases, such as diarrhea, particularly in communities lacking adequate sanitation infrastructure (*Carlton et al.*, 2014). Irregular and intense rainfall events further affect food security and clean water supply, exacerbating social inequalities in disaster-prone regions.

Rainfall forecasting in tropical regions presents greater challenges than in the subtropics, due to its lower accuracy (*Haiden et al.*, 2012). This discrepancy stems from the complexity of tropical atmospheric systems and their connections to both local convection and large-scale equatorial waves, such as Convectively Coupled Equatorial Waves (CCEWs) and the Madden–Julian Oscillation (MJO), which remain difficult to represent accurately in numerical weather prediction (NWP) models (*Zhu et al.*, 2014; *Gehne et al.*, 2022). Nevertheless, the tropics exhibit longer predictability horizons, attributed to the dominant role of equatorial waves, which help prolong forecast skill and are more resilient to error growth than baroclinic disturbances in mid-latitudes (*Judt*, 2020). Additionally, NWP forecasts in the tropics rely heavily on convective parameterization, which introduces further uncertainty (*Selz* and *Craig*, 2015).

The Four-Dimensional Variational Data Assimilation (4DVar) method has enhanced precipitation forecast accuracy for up to 10 days ahead (*Lopez*, 2013). 4DVar enables the assimilation of multitemporal observations, consistent with the model dynamics, leading to more realistic atmospheric state estimations (*Tiwari* and *Kumar*, 2022). The longer the observational period assimilated, the greater the increase in the forecast accuracy (*Trémolet*, 2006).

Numerous studies have explored the integration of 4DVar with remote sensing. Some researchers have assimilated radar data into models (*Ban et al.*, 2017; *Tai et al.*, 2020; *Thiruvengadam et al.*, 2020; *Syafitri* and *Sari*, 2021), while others have focused on satellite data (*Lin et al.*, 2017; *Pan et al.*, 2017; *Yi et al.*, 2018; *Wu et al.*, 2020; *Zhang et al.*, 2020; *Gopalakrishnan* and *Chandrasekar*, 2022; *Vourlioti et al.*, 2022; *Wang et al.*, 2023; *Ren et al.*, 2024; *Patel et al.*, 2025). Radar-based rainfall estimation is more reliable than satellite data (*Jiang et al.*, 2019) and provides higher resolution (*Tesfagiorgis et al.*, 2011). However, weather radar systems are limited in terms of coverage area. For regions not covered by radar, the assimilation of satellite data provides an alternative to improve forecast accuracy. One such product is GSMaP, which offers a latency of approximately one hour, faster than the IMERG product of NOAA (*P. Neeck* and *Oki*, 2018). While the assimilation of GSMaP data into NWP models for precipitation forecasting has been limited, *Kumar et al.* (2014) are among the few to investigate the impact of assimilating GSMaP rainfall data using WRF 4DVar.

This study aims to assess the impact of assimilating GSMaP data with WRF 4DVar on forecasting heavy rainfall in the MC. This research will focus on central Sulawesi, located in the heart of the MC. The study will consider six heavy rainfall events resulting in flooding and landslides, causing loss of life and material damage (BNPB, 2024). These six events occurred on July 12, 2020; October 3, 2021; October 29, 2021; October 18, 2022; May 16, 2023; and May 2, 2024.

2. Materials and methods

As the primary reference for this study, we use 139 rainfall gauges operated by the Indonesian Agency for Meteorology, Climatology and Geophysics (BMKG), symbolized as a black circle in *Fig. 1*. Weather station measurements serve as the primary source of rainfall observations over land (*Barlow et al.*, 2019). The FNL (Final Analysis) data are provided by the NOAA (*UCAR*, 2015a). It is used as the spin-up time data for the WRF-ARW model for 12 hours. Additionally, we utilize the GFS (Global Forecast System) from NOAA (*UCAR*, 2015b) as the boundary condition forecast. For the assimilated data, we employ Global Satellite Mapping of Precipitation NOW (GSMaP_NOW), which is accumulated every 6 hours.

In *Fig. 1*, the study area is central Sulawesi, marked with a red line. Domain 1 of WRF covers most of Sulawesi, with spatial and temporal output resolutions of 10 km and 3 hours, respectively, illustrated as a purple box. Domain 2

encompasses the study area with spatial and temporal output resolutions of 2 km and 1 hour, respectively, marked with a black box. The vertical levels for both domains are set to 34, which aligns with the vertical levels of the GFS.

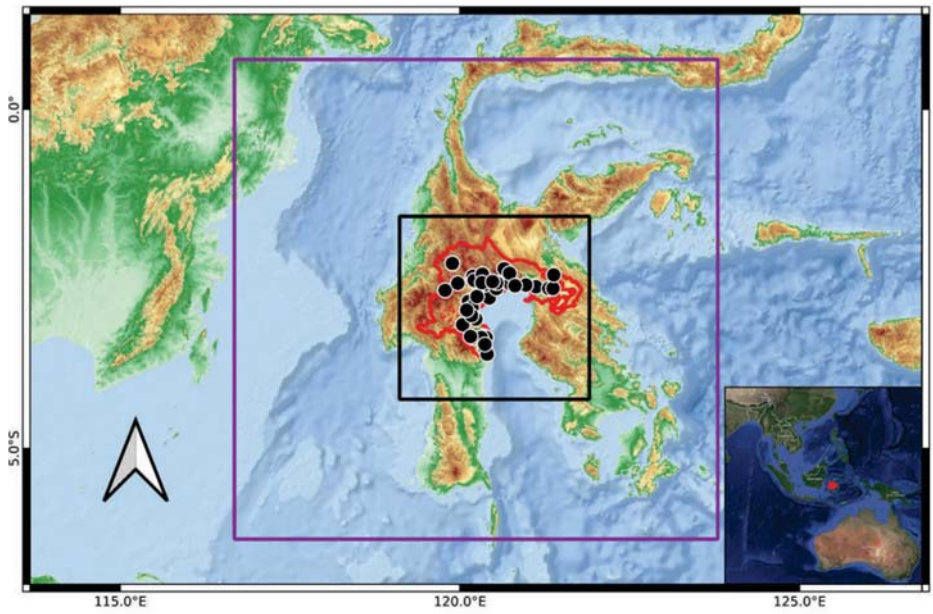

Fig. 1. WRF-ARW domain 1 (purple box), domain 2 (black box), study area (red line), and rain gauges (black circles)

For this study, we employ tropical-specific physical parameterizations (*Table 1*), which include the WRF Single Moment 6-Class (WSM6) microphysics scheme, the more recent Tiedtke scheme for cumulus convection, the Rapid Radiative Transfer Model for Global Circulation Models (RRTMG) for both shortwave and longwave radiations, and the Yonsei University (YSU) scheme for the planetary boundary layer. Notably, the WSM6 scheme includes graupel production in the microphysical process (*Hong* and *Lim*, 2006), distinguishing it from the WSM5 scheme (*Lim* and *Hong*, 2005). The more recent Tiedtke scheme calculates cloud and ice mixing ratios, momentum tendencies, and shallow convection (*Skamarock et al.*, 2019). This scheme has been shown to capture the fundamental characteristics of the marine boundary layer structure and low clouds (*Zhang et al.*, 2011) and provide improved diurnal precipitation simulations (*Sun* and *Bi*, 2019). Additionally, the RRTMG scheme offers more accurate radiation forcing results, especially for high-resolution computations (*Iacono et al.*, 2008).

Table 1. WRF-ARW configuration for domain 1 and domain 2

Configuration	Domain 1	Domain 2
Temporal resolution	3 h	1 h
Spatial resolution	10 km	2 km
Vertical level	34	34
Parameterization	*Tropical*	*Tropical, Cu=0*

The WRF model is run for non-assimilation (NONDA) and 4DVar assimilation (DA) scenarios. NONDA uses FNL data at 12 UTC and 18 UTC for a 12-hour spin-up time, followed by forecasts up to t+24 hours. In contrast, DA assimilates 3-hour accumulated GSMaP data at 18 UTC and 00 UTC, with assimilation performed within Domain 1 (*Fig. 2*).

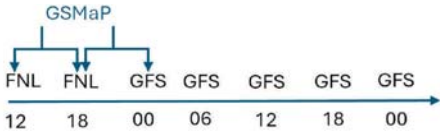

Fig. 2. Timeline of WRF.

Several WRF output variables will be analyzed, including precipitation, specific humidity, temperature, and wind. Precipitation is the sum of non-convective rainfall (RAINNC) and shallow cumulus rainfall (RAINSH). Specific humidity (Q) is calculated from the water vapor mixing ratio (*r*) using the formula (*Stull*, 2020):

$$Q = \frac{r}{1+r} \tag{1}$$

The DA and NONDA model forecasts will be evaluated against ERA5 reanalysis data for specific humidity, temperature, and vertical velocity using the root mean square error (RMSE) metric. ERA5 is used as the reference because in-situ sounding observations are unavailable in the study area, and several researchers – such as *Kumar et al.* (2014), *Xie et al.* (2018), and *Zheng et al.*(2023) – have employed ERA5 in similar contexts. RMSE measures the average error between the predicted values from the model and the actual observed values (*James et al.*, 2013). For assessing the accuracy and bias of the rainfall forecasts, DA and NONDA rainfall predictions will be tested against the rain gauge data using the bias score (*Hayashi et al.*, 2008; *Gao et al.*, 2021; *Syafitri* and *Sari*, 2021) and equitable threat score (ETS) (*Hayashi et al.*, 2008; *Mohanty et al.*, 2012; *Kumar et al.*, 2014; *Wu et al.*, 2020; *Rakesh* and *Kutty*, 2021; *Wang et al.*, 2023). Rainfall evaluation will also use nine surrounding grids with the fractional bias score (FBS) and fractional skill score (FSS) methods (*Ban et al.*, 2017; *Wu et al.*, 2020; *Wang et al.*, 2023). FBS and FSS are used to quantitatively assess the spatial skill of rainfall forecasts, particularly when differences between experiments are not visually distinct (*Roberts* and *Lean*, 2008).

3. Results and discussion

3.1. Observation analysis

On October 18, 2022 (*Fig. 3d*) and May 2, 2024 (*Fig. 3f*), the maximum rainfall occurred in the mountainous regions, as indicated by the black 500 m elevation contours. The maximum rainfall was observed in the lowlands on other dates (*Figs. 3a-c* and *3e*). The maximum rainfall is localized, with no significant rainfall observed in the surrounding areas, except on July 12, 2020 (*Fig. 3a*). This highlights the necessity of high-resolution models to accurately predict the spatial distribution of rainfall. Furthermore, extreme rainfall in these lowland areas could not be adequately simulated using only the WRF NONDA model in the study by *Yulihastin et al.* (2021).

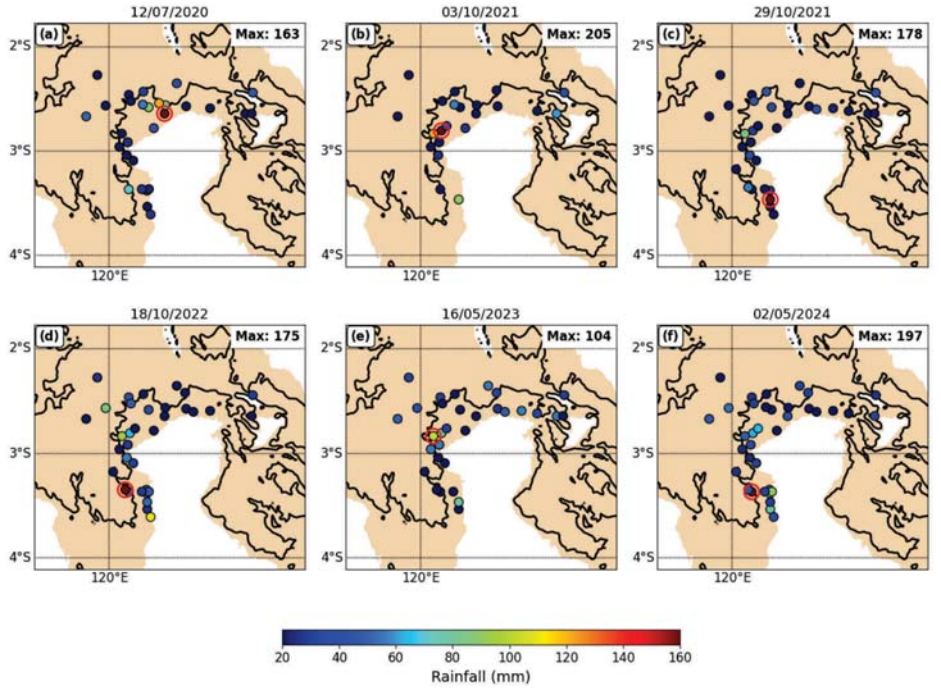

Fig. 3. 24-hour rainfall accumulation of gauges for six heavy rainfall events. The red circles are maximum rainfall locations. The black lines represent the 500 m elevation contours, and the light brown shaded area denotes the island of Sulawesi.

3.2. *Specific humidity, temperature, and vertical velocity*

Fig. 4 displays the RMSE of DA and NONDA against ERA5. The RMSE of specific humidity for DA is larger than that of NONDA in the low level at 00 UTC and 06 UTC. In comparison, the RMSE of specific humidity for DA is smaller in the middle and upper layers between 06 UTC and 18 UTC (*Fig. 4a*). In the middle layer at 00 UTC (*Fig. 4b*), the RMSE of temperature for DA is also higher than for NONDA. In contrast, *Fig. 4c* shows that the RMSE of vertical velocity for DA is smaller than NONDA in the low level at 06 UTC and in the middle and upper layers at 12 UTC. The decrease in RMSE of specific humidity in the low level and the increase in RMSE of temperature in the middle layer for DA compared to NONDA are also simulated in the study by (*Xie et al.*, 2018), which used 3DVar assimilation of AMSU-A and MHS radiation. Additionally, DA rainfall assimilation reduces the RMSE of specific humidity when compared to conventional observation assimilation at the 1000 hPa layer (*Wang et al.*, 2023).

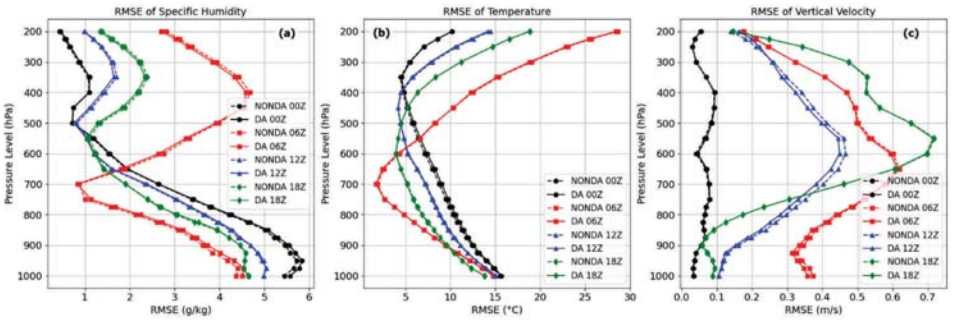

Fig. 4. RMSE DA and NONDA against ERA5 for (a) specific humidity, (b) temperature, and (c) vertical velocity.

In the time section of *Fig. 5a*, the specific humidity (*Q*) for DA reaches its maximum between 06 UTC and 08 UTC, with values approaching 16 g/kg, which is lower than NONDA. The *Q* for DA in the low to mid-levels (1–5 km) becomes larger after 12 UTC, which is consistent with the findings of Pan et al. (2022). At mid to upper levels (6–9 km), the *Q* in DA is higher than in NONDA from 01 to 07 UTC, but then becomes lower starting at 08 UTC.

The temperature (*T*) at the low level for DA shows slight temporal variation (*Fig. 5b*), as the diurnal temperature variation in the tropics is much smaller than in the subtropics (*Riehl*, 1979). At low levels (1–4 km), the *T* of DA is only higher than NONDA between 00 UTC and 03 UTC, after which it becomes lower. At mid-levels (4–7 km), the *T* of DA exceeds that of NONDA starting from 06 UTC, although the difference remains small. At upper levels (9–12 km), the T of DA is higher than NONDA between 01 and 05 UTC.

In *Fig. 5c*, the vertical velocity (*W*) in the low level for DA is positive starting from 00 UTC and extends to the upper layers by 06 UTC. This upward motion weakens after 12 UTC. Compared to NONDA, positive changes are observed in the middle and upper layers, especially at 07 UTC and 09–14 UTC. In contrast, at the low level, the *W* for DA is lower than for NONDA, except at 07 UTC when the *W* of DA exceeds that of NONDA. *Mohanty et al*. (2012), *Narasimha Rao et al.* (2020), and *Pan et al.* (2022) also observed an increase in vertical velocity values.

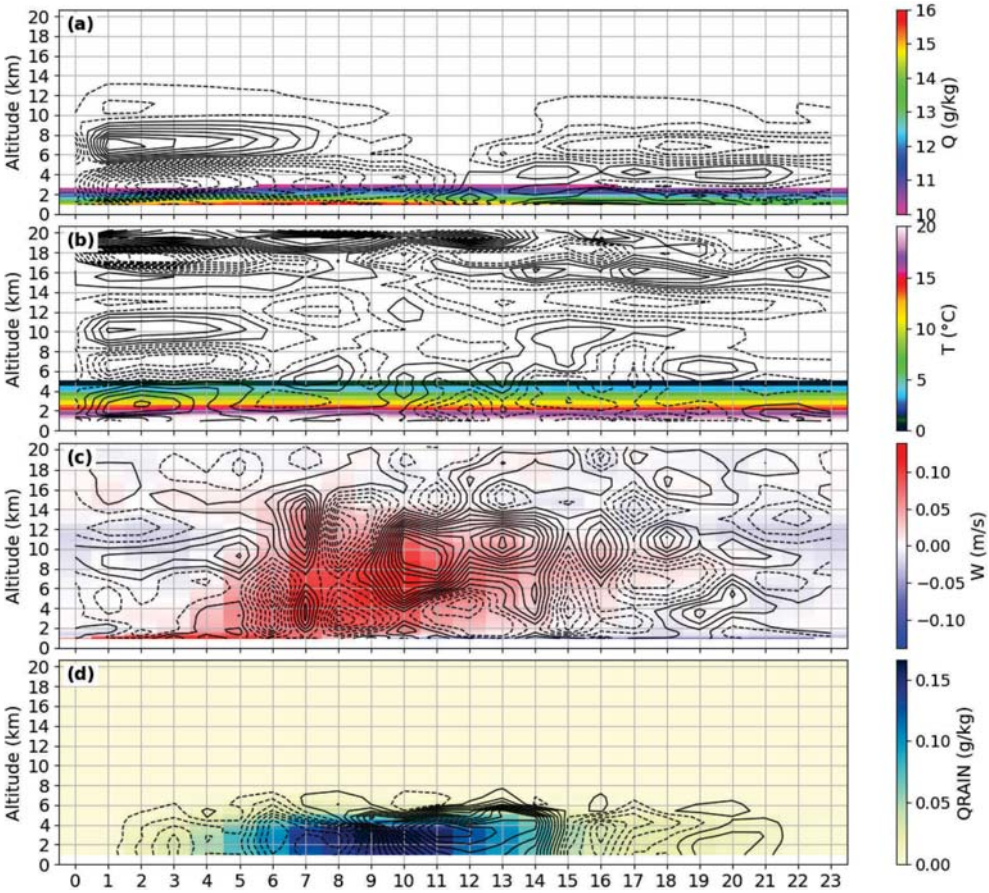

Fig. 5. Time–height section of the DA composite (shading) and DA–NONDA difference (contours) for (a) specific humidity, (b) temperature, (c) vertical velocity, and (d) rainwater mixing ratio. Solid contours are for positive values and dashed contours are for negative values.

Fig. 5d shows that the rainwater mixing ratio (*QRAIN*) reaches its maximum between 07 and 11 UTC, with values confined below 4 km altitude. This peak in

QRAIN occurs prior to the maximum *Q* and coincides with the maximum *W*. The observed lag time reflects the process of water vapor converting into raindrops. The coincidence indicates the direct influence of strong vertical velocity on *QRAIN*. Compared to NONDA, *QRAIN* in the DA experiment is higher between 10 and 14 UTC, coinciding with enhanced *W* at mid and upper levels.

At the low level, ΔQ is generally negative at 00 and 06 UTC (*Fig. 6a-b*), except for some areas in the mountainous region where it becomes positive at 06 UTC. The most significant increase in *Q* for DA occurs in the western region, covering both the lowlands and mountainous areas at 12 UTC (*Fig. 6c*), and is limited to the mountainous areas at 18 UTC (*Fig. 6d*). The increase in *T* of DA is mostly concentrated over mountainous regions at 00 UTC (Fig. 6e), but becomes negative at 06 UTC (*Fig. 6f*). The reduction in ΔT at 12 UTC intensifies due to evaporative cooling caused by rainfall (*Fig. 6g–h*). Although the general pattern of ΔW is negative, the spatial distribution of ΔW shows positive values in the mountains at 06 UTC (*Fig. 6j*) and in the lowlands at 12 UTC (*Fig. 6k*). No significant changes in *W* are observed at 00 UTC (*Fig. 6i*) and 18 UTC (*Fig. 6l*). *Xiong et al.* (2020) also observed the same general pattern, where topography influences the assimilation in WRF.

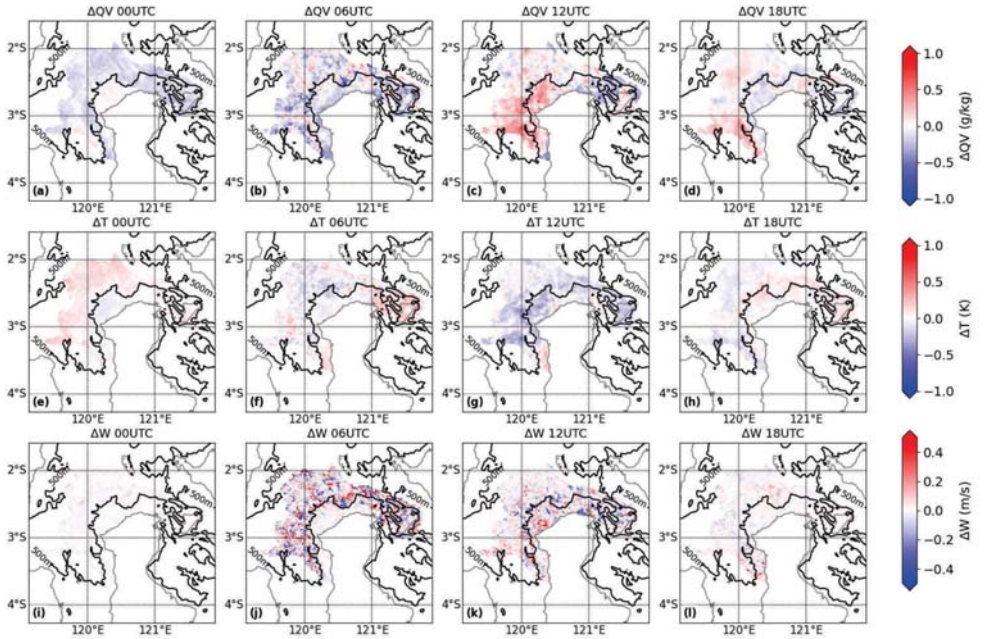

Fig. 6. Composite of DA–NONDA differences at low levels for (a–d) specific humidity, (e–h) temperature, and (i–l) vertical velocity. Contours represent elevations at 500 m.

3.3. Rainfall

Fig. 7a shows that DA and NONDA predict rainfall as underestimated, with a bias score of less than 1. DA predicts higher rainfall than NONDA in 10–40 mm, 80 mm, and 130–140 mm, while it predicts lower rainfall in 50 mm, 100 mm, and 120 mm. The ETS for both DA and NONDA is generally very small, with accuracy improvements in 20-30 mm and 60-80 mm, and DA being worse in the 40-50 mm (*Fig. 7b*). Although the ETS for DA is small, similar to the smaller rainfall ETS in tropical regions compared to subtropical areas (*Hayashi et al.*, 2008), DA generally improves the prediction of heavy rainfall, as found in the research by Dhanya and Chandrasekar using WRF 3DVar (*Dhanya* and *Chandrasekar*, 2016).

Considering nearby grids, the FBS for DA is less than 1, indicating that the predicted rainfall for DA is lower than the observed rainfall. The FBS for DA is lower than for NONDA in the 60-80 mm rainfall range, but higher in the 10-40 mm range (*Fig. 7c*). In *Fig. 7d*, the FSS for DA is greater than 0.6 only up to the 20 mm threshold. The FSS for DA is smaller than for NONDA in the 10-40 mm rainfall range, but larger in the 60-80 mm rainfall range.

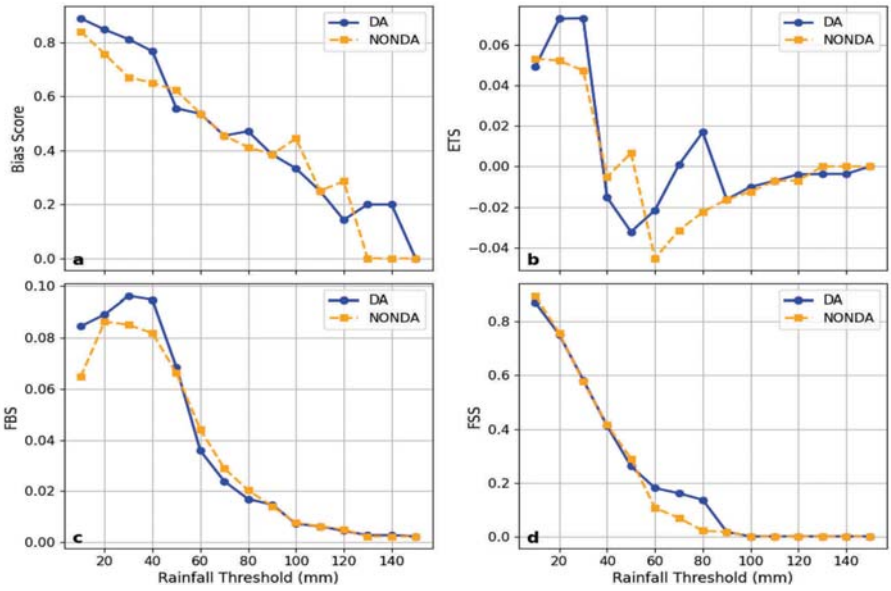

Fig. 7. Daily rainfall verification scores at several thresholds: (a) bias score, (b) equitable threat score, (c) fractional bias store, and (d) fractional skill score.

Fig. 8 shows that the mean rainfall predicted over the study area by the DA model exceeds that of the NONDA model during the spin-up period. This suggests a significant impact of satellite rainfall assimilation in the initial hours post-analysis. The forecasted rainfall in DA peaks more gradually than in NONDA, leading to a negative DA-NONDA difference until 09 UTC, after which it becomes positive. Both models exhibit the same start and end times for rainfall. Since the values represent spatial averages over the study area, slight differences in DA–NONDA rainfall may correspond to substantial discrepancies at localized scales.

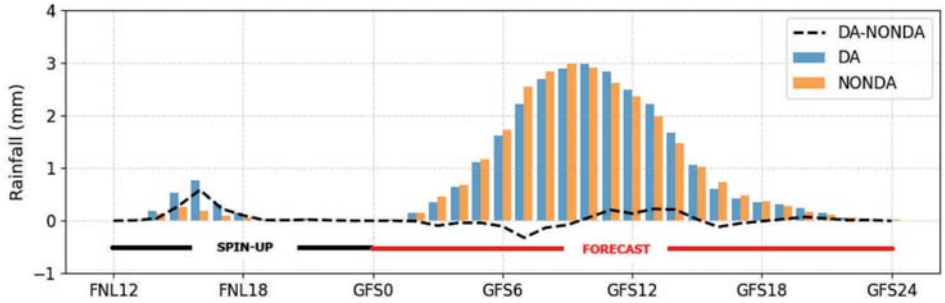

Fig. 8. Composite of area-averaged diurnal rainfall of DA and NONDA.

At 00 UTC, rainfall in both DA (*Fig. 9a*) and NONDA (*Fig. 9e*) remains below 1 mm/h. By 06 UTC, rainfall in DA (Fig. 9b) and NONDA (*Fig. 9f*) is concentrated over the mountainous regions. At 12 UTC, rainfall in both models (*Fig. 9c* and *Fig. 9g*) extends across the entire study area, including the lowlands and mountains. DA predicts greater rainfall in the lowlands at 12 UTC (*Fig. 9k*) compared to NONDA. This enhancement is attributed to increased *Q* and stronger *W* in the lowlands. By 18 UTC, rainfall diminishes sharply in both DA (*Fig. 9d*) and NONDA (*Fig. 9h*). This diurnal rainfall pattern aligns with typical conditions observed in the MC, as *Sakaeda et al.* (2020) and *Cui* and *Pu* (2023) reported. The improved lowland rainfall prediction by the DA experiment demonstrates the effectiveness of GSMaP assimilation in enhancing model performance, particularly in regions often underestimated in NONDA runs. This result highlights the potential of GSMaP assimilation as a reliable alternative to weather radar assimilation, which has already been shown to improve forecast accuracy (*Ban et al.*, 2017; *Tai et al*., 2020; *Thiruvengadam et al*., 2020; *Syafitri* and *Sari*, 2021). Furthermore, GSMaP assimilation offers a practical solution for areas lacking radar coverage, making it especially valuable for operational forecasting in data-sparse regions.

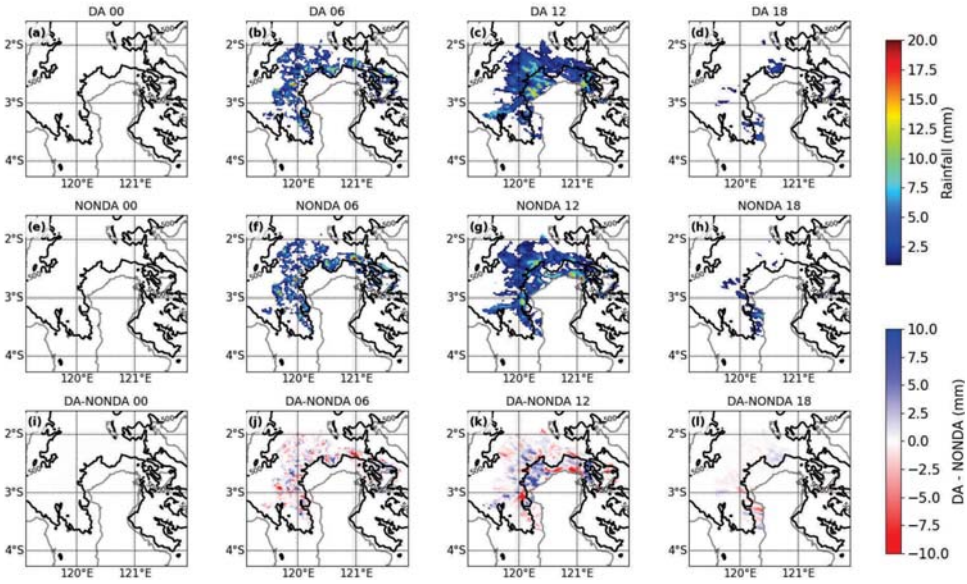

Fig. 9. Rainfall composite of DA (a-d), NONDA (e-h), and DA-NONDA (i-l). Contours represent elevations at 500 m.

4. Conclusions

This study examines the performance of WRF 4DVAR with GSMaP rainfall assimilation compared to a non-assimilated WRF at a 2 km resolution in forecasting six heavy rainfall events that led to floods and landslides in the Maritime Continent. The findings indicate that DA improves the accuracy of vertical velocity and specific humidity predictions, particularly in the middle and upper atmospheric layers. DA shows lower specific humidity values at lower levels and higher values at mid-to-upper levels. While temperature differences between DA and NONDA are minimal, DA slightly increases temperatures at mid and upper levels and exhibits more pronounced upward vertical velocity at these levels. DA predicts higher rainwater mixing ratios, which correspond to higher vertical velocity. Additionally, DA improves the accuracy of heavy rainfall predictions, enhancing rainfall forecasting, particularly in lowland regions, in line with the specific humidity and vertical velocity patterns.

References

Argüeso, D., Romero, R., and *Homar, V.*, 2020: Precipitation features of the maritime continent in parameterized and explicit convection models. *Journal of Climate*, *33*. https://doi.org/10.1175/JCLI-D-19-0416.1

Ban, J., Liu, Z., Zhang, X., Huang, X.Y., and *Wang, H.*, 2017: Precipitation data assimilation in WRFDA 4D-Var: implementation and application to convection-permitting forecasts over United States. *Tellus, Series A: Dynamic Meteorology and Oceanography*, *69*. https://doi.org/10.1080/16000870.2017.1368310

Barlow, M., Gutowski, W.J., Gyakum, J.R., Katz, R.W., and *Lim, Y.K.*, 2019: North American extreme precipitation events and related large-scale meteorological patterns: A review of statistical methods, dynamics, modeling, and trends. *Climate Dynamics*, *53*, 1841–1863. https://doi.org/10.1007/s00382-019-04958-z

Carlton, E.J., Eisenberg, J.N.S., Goldstick, J., Cevallos, W., Trostle, J., and *Levy, K.*, 2014: Heavy rainfall events and diarrhea incidence: The role of social and environmental factors. *American Journal of Epidemiology*, *179*. https://doi.org/10.1093/aje/kwt279

Chen, C., Sahany, S., Moise, A.F., Chua, X.R., Hassim, M.E., Lim, G., and *Prasanna, V.*, 2023: ENSO–Rainfall Teleconnection over the Maritime Continent Enhances and Shifts Eastward under Warming. *Journal of Climate*, *36*. https://doi.org/10.1175/JCLI-D-23-0036.1

Cui, Z., and *Pu, Z.*, 2023: The Use of Regional Data Assimilation to Improve Numerical Simulations of Diurnal Characteristics of Precipitation during an Active Madden–Julian Oscillation Event over the Maritime Continent. *Remote Sensing*, *15*. https://doi.org/10.3390/rs15092405

Dhanya, M., and *Chandrasekar, A.*, 2016: Impact of variational assimilation using multivariate background error covariances on the simulation of monsoon depressions over India. *Annales Geophysicae*, *34*. https://doi.org/10.5194/angeo-34-187-2016

Gao, S., Yu, H., Ren, C., Liu, L., and *Min, J.*, 2021: Assimilation of Doppler Radar Data with an Ensemble 3DEnVar Approach to Improve Convective Forecasting. *Advances in Atmospheric Sciences*, *38*. https://doi.org/10.1007/s00376-020-0081-z

Gehne, M., Wolding, B., Dias, J., and *Kiladis, G.N.*, 2022: Diagnostics of Tropical Variability for Numerical Weather Forecasts. *Weather and Forecasting*, *37*. https://doi.org/10.1175/WAF-D-21-0204.1

Gopalakrishnan, D., and *Chandrasekar, A.*, 2022: The sensitivity of the WRF-4DVar data assimilation system to the control variables: A study on heavy rainfall events over India. *Dynamics of Atmospheres and Oceans*, *99*, 101304. https://doi.org/10.1016/j.dynatmoce.2022.101304

Guo, J., and *Chen, J.*, 2022: The Impact of Heavy Rainfall Variability on Fertilizer Application Rates: Evidence from Maize Farmers in China. *International Journal of Environmental Research and Public Health*, *19*. https://doi.org/10.3390/ijerph192315906

Haiden, T., Rodwell, M.J., Richardson, D.S., Okagaki, A., Robinson, T., and *Hewson, T.*, 2012: Intercomparison of global model precipitation forecast skill in 2010/11 using the SEEPS score. *Monthly Weather Review*, *140*. https://doi.org/10.1175/MWR-D-11-00301.1

Hayashi, S., Aranami, K., and *Saito, K.*, 2008: Statistical Verification of Short Term NWP by NHM and WRF-ARW with 20 km Horizontal Resolution around Japan and Southeast Asia *4*, 133–136.

Hong, S.-Y., and *Lim, J.-O.J.*, 2006: The WRF Single-Moment 6-Class Microphysics Scheme (WSM6). *Journal of Korean Meteorlogy 42(2)*, 129–151..

Huang, J.J., Gan, Y.Q., Miao, S.X., Wu, J.Q., Yang, L., Hua, M., Min, W., Zhao, L.H., and *Fang, Q.*, 2011: A preliminary study of the evaluation index system for geo-environment regionalization in Jiangsu. *Geol China*, *38*. https://doi.org/10.3969/j.issn.1000-3657.2011.06.020

Iacono, M.J., Delamere, J.S., Mlawer, E.J., Shephard, M.W., Clough, S.A., and *Collins, W.D.*, 2008: Radiative forcing by long-lived greenhouse gases: Calculations with the AER radiative transfer models. *Journal of Geophysical Research Atmospheres*, *113*. doi:10.1029/2008JD009944

James, G., Witten, D., Hastie, T., and *Tibishirani, R.*, 2013: *An Introduction to Statistical Learning with Applications in R (older version)*, Springer Texts in Statistics.

Jiang, Q., Li, W., Wen, J., Fan, Z., Chen, Y., Scaioni, M., and *Wang, J.*, 2019: Evaluation of satellite-based products for extreme rainfall estimations in the eastern coastal areas of China. *Journal of Integrative Environmental Sciences*, *16*, 191–207. https://doi.org/10.1080/1943815X.2019.1707233

Jiang, W., and *Tan, Y.*, 2021: Heavy rainfall-related excavation failures in China during 1994 to 2018: An overview. *Engineering Failure Analysis*,. doi:10.1016/j.engfailanal.2021.105695

Judt, F., 2020: Atmospheric predictability of the tropics, middle latitudes, and polar regions explored through global storm-resolving simulations. *Journal of the Atmospheric Sciences*, *77*. https://doi.org/10.1175/JAS-D-19-0116.1

Kumar, P., Kishtawal, C.M., and *Pal, P.K.*, 2014: Impact of satellite rainfall assimilation on weather research and forecasting model predictions over the Indian region. *Journal of Geophysical Research*, *119*. https://doi.org/10.1002/2013JD020005

Li, L., Zheng, Z., Biederman, J.A., Xu, C., Xu, Z., Che, R., Wang, Y., Cui, X., and *Hao, Y.*, 2019: Ecological responses to heavy rainfall depend on seasonal timing and multi-year recurrence. *New Phytologist*, *223*. https://doi.org/10.1111/nph.15832

Lim, J.O.J., and *Hong, S.Y.*, 2005: Effects of bulk ice microphysics on the simulated monsoonal precipitation over east Asia. *Journal of Geophysical Research Atmospheres*, *110*, 1–16. https://doi.org/10.1029/2005JD006166

Lin, L.F., Ebtehaj, A.M., Flores, A.N., Bastola, S., and *Bras, R.L.*, 2017: Combined assimilation of satellite precipitation and soil moisture: A case study using TRMM and SMOS data. *Monthly Weather Review*, *145*, 4997–5014. https://doi.org/10.1175/MWR-D-17-0125.1

Lopez, P., 2013: Experimental 4D-var assimilation of SYNOP rain gauge data at ECMWF. *Monthly Weather Review*, *141*. https://doi.org/10.1175/MWR-D-12-00024.1

Mohanty, U.C., Routray, A., Osuri, K.K., and *Kiran Prasad, S.*, 2012: A study on simulation of heavy rainfall events over Indian region with ARW-3DVAR modeling system. *Pure and Applied Geophysics*, *169*. https://doi.org/10.1007/s00024-011-0376-1

Muthiah, K., Arunya, K.G., Sridhar, V., and *Patakamuri, S.K.*, 2025: Heavy Rainfall Impact on Agriculture: Crop Risk Assessment with Farmer Participation in the Paravanar Coastal River Basin. *Water*,. doi:10.3390/w17050658

Narasimha Rao, N., Shekhar, M.S., and *Singh, G.P.*, 2020: Forecasting extreme precipitation event over Munsiyari (Uttarakhand) using 3DVAR data assimilation in mesoscale model. *Journal of Earth System Science*, *129*. https://doi.org/10.1007/s12040-019-1315-2

P. Neeck, S., and *Oki, R.*, 2018: Precipitation Virtual Constellation (P-VC). URL https://ceos.org/document_management/Meetings/SIT-Technical-Workshop/2015-SIT-Tech-Workshop/SITWS2015_VCWGDay_03_Presentation PVC rev d no anim.pdf (accessed 10.7.25).

Pan, X., Li, X., Cheng, G., and *Hong, Y.*, 2017: Effects of 4D-Var data assimilation using remote sensing precipitation products in a WRF model over the complex terrain of an arid region river basin. *Remote Sensing*, *9*. https://doi.org/10.3390/rs9090963

Pan, Z., Zhang, S., and *Zhang, W.*, 2022: Impact of Radar and Surface Data Assimilation on the Forecast of a Nocturnal Squall Line in the Yangtze–Huaihe River. *Atmosphere*, *13*. https://doi.org/10.3390/atmos13091522

Patel, S.S., Routray, A., Singh, V., Bhatla, R., Kumar, R., and *Surovyatkina, E.*, 2025: Evaluation of 3D-Var and 4D-Var data assimilation on simulation of heavy rainfall events over the Indian region. *Meteorological Applications*, *32*, 1–32. https://doi.org/10.1002/met.70037

Qian, J.H., 2008: Why precipitation is mostly concentrated over islands in the maritime continent. *Journal of the Atmospheric Sciences*, *65*, 1428–1441. https://doi.org/10.1175/2007JAS2422.1

Rais, A.F., Hudayat, N., and *Yunita, R.*, 2023: Accuracy improvement of merging real-time global satellite mapping of precipitation (GSMaP_NOW) and gauge: A case study of Jakarta flood on January 1, 2020. AIP, 040011. https://doi.org/10.1063/5.0181671

Rakesh, S., and *Kutty, G.*, 2021: Intercomparison of the Performance of Four Data Assimilation Schemes in a Limited-Area Model on Forecasts of an Extreme Rainfall Event Over the Uttarakhand in Himalayas. *Earth* and *Space Science*, *8*. https://doi.org/10.1029/2020EA001461

Ren, J., Huang, C., Hou, J., Zhang, Y., Ma, P., and *Yang, L.*, 2024: Impact of the combined assimilation of GPM/IMGER precipitation and Himawari-8/AHI water vapor radiance on snowfall forecasts

using WRF model and 4Dvar system. *Atmospheric Research*, *311*, 107726. https://doi.org/10.1016/j.atmosres.2024.107726

Riehl, H., 1979: *Climate* and *Weather in the Tropics*. Academic Press, London.

Roberts, N.M., and *Lean, H.W.*, 2008: Scale-selective verification of rainfall accumulations from high-resolution forecasts of convective events. *Monthly Weather Review*, *136*, 78–97. https://doi.org/10.1175/2007MWR2123.1

Ruppert, J.H., and *Chen, X.*, 2020: Island Rainfall Enhancement in the Maritime Continent. *Geophysical Research Letters*, *47*. https://doi.org/10.1029/2019GL086545

Sahoo, S.K., *Himesh, S.*, and *Gouda, K.C.*, 2020: Impact of Urbanization on Heavy Rainfall Events: A Case Study over the Megacity of Bengaluru, India. *Pure and Applied Geophysics*, *177*. https://doi.org/10.1007/s00024-020-02624-8

Sakaeda, N., *Kiladis, G.*, and *Dias, J.*, 2020: The diurnal cycle of rainfall and the convectively coupled equatorial waves over the maritime continent. *Journal of Climate*, *33*, 3307–3331. https://doi.org/10.1175/JCLI-D-19-0043.1

Selz, T., and *Craig, G.C.*, 2015: Simulation of upscale error growth with a stochastic convection scheme. *Geophys. Res. Lett.*, *42*, 3056–3062. doi:https://doi.org/10.1002/2016RG000538

Skamarock, W.C., *Klemp, J.B.*, *Dudhia, J.*, *Gill, D.O.*, *Liu, Z.*, *Berner, J.*, *Wang, W.*, *Powers, J.G.*, *Duda, M.G.*, *Barker, D.M.*, and *Huang, X.-Y.*, 2019: A Description of the Advanced Research WRF Model Version 4. Boulder. https://doi.org/10.5065/1dfh-6p97

Stull, R., 2020: *Practical Meteorology :* An Algebra-based Survey of Atmospheric Science Roland. The University of British Columbia, 944 p.

Sun, B.Y., and *Bi, X.Q.*, 2019: Validation for a tropical belt version of WRF: sensitivity tests on radiation and cumulus convection parameterizations. *Atmospheric and Oceanic Science Letters*, *12*, 192–200. https://doi.org/10.1080/16742834.2019.1590118

Syafitri, J.D.I., and *Sari, F.P.*, 2021: Four-dimensional variational (4DVAR) performance test with assimilation satellite and radar data (case study of a heavy rainfall Bengkulu March 4, 2019), In: IOP Conference Series: Earth and Environmental Science. 10.1088/1755-1315/893/1/012031

Tai, S.L., *Liou, Y.C.*, *Chang, S.F.*, and *Sun, J.*, 2020: The heavy rainfall mechanism revealed by a terrain-resolving 4dvar data assimilation system-A case study. *Monthly Weather Review*, *148*, 2307–2330. https://doi.org/10.1175/MWR-D-19-0244.1

Tesfagiorgis, K., *Mahani, S.E.*, *Krakauer, N.Y.*, and *Khanbilvardi, R.*, 2011: Bias correction of satellite rainfall estimates using a radar-gauge product – a case study in Oklahoma (USA). *Hydrology and Earth System Sciences*, *15*. https://doi.org/10.5194/hess-15-2631-2011

Thiruvengadam, P., *Indu, J.*, and *Ghosh, S.*, 2020: Significance of 4DVAR Radar Data Assimilation in Weather Research and Forecast Model-Based Nowcasting System. *Journal of Geophysical Research: Atmospheres*, *125*, 1–20. https://doi.org/10.1029/2019JD031369

Tiwari, G., and *Kumar, P.*, 2022: Predictive skill comparative assessment of WRF 4DVar and 3DVar data assimilation: An Indian Ocean tropical cyclone case study. *Atmospheric Research*, *277*. https://doi.org/10.1016/j.atmosres.2022.106288

Trémolet, Y., 2006: Accounting for an imperfect model in 4D-Var. *Quarterly Journal of the Royal Meteorological Society*, *132*. https://doi.org/10.1256/qj.05.224

Trenberth, K.E., 2005: The Impact of Climate Change and Variability on Heavy Precipitation, Floods, and Droughts, In: Encyclopedia of Hydrological Sciences. https://doi.org/10.1002/0470848944.hsa211

UCAR, 2015a: NCEP GDAS/FNL 0.25 Degree Global Tropospheric Analyses and Forecast Grids.

UCAR, 2015b: NCEP GFS 0.25 Degree Global Forecast Grids Historical Archive.

Vourlioti, P., *Mamouka, T.*, *Agrafiotis, A.*, and *Kotsopoulos, S.*, 2022: Medicane Ianos: 4D-Var Data Assimilation of Surface and Satellite Observations into the Numerical Weather Prediction Model WRF. *Atmosphere*, *13*. https://doi.org/10.3390/atmos13101683

Wang, Y., *Li, X.*, and *Chen, Y.*, 2023: Combined assimilation of hourly rainfall data and every 10-min AHI radiance with WRF 4DVar for the short-range heavy rainfall forecast in Eastern China. *Atmospheric Research*, *292*. https://doi.org/10.1016/j.atmosres.2023.106867

Wu, Y., *Liu, Z.*, and *Li, D.*, 2020: Improving forecasts of a record-breaking rainstorm in Guangzhou by assimilating every 10-min AHI radiances with WRF 4DVAR. *Atmospheric Research*, *239*. https://doi.org/10.1016/j.atmosres.2020.104912

Xie, Y., *Shi, J.*, *Fan, S.*, *Chen, M.*, *Dou, Y.*, and *Ji, D.*, 2018: Impact of radiance data assimilation on the prediction of heavy rainfall in RMAPS: A case study. *Remote Sensing*, *10*. https://doi.org/10.3390/rs10091380

Yamanaka, M.D., 2016: Physical climatology of Indonesian maritime continent: An outline to comprehend observational studies. *Atmospheric Research*, *178–179*, 231–259. 10.1016/j.atmosres.2016.03.017

Yi, L., *Zhang, W.*, and *Wang, K.*, 2018: Evaluation of heavy precipitation simulated by the WRF model using 4D-Var data assimilation with TRMM 3B42 and GPM IMERG over the Huaihe River basin China. *Remote Sensing*, *10*. https://doi.org/10.3390/rs10040646

Yulihastin, E., *Nuryanto, D.E.*, *Trismidianto,* and *Muharsyah, R.*, 2021: Improvement of heavy rainfall simulated with sst adjustment associated with mesoscale convective complexes related to severe flash flood in luwu, sulawesi, indonesia. *Atmosphere*, *12*. https://doi.org/10.3390/atmos12111445

Zhang, C., *Wang, Y.*, and *Hamilton, K.*, 2011: Improved representation of boundary layer clouds over the southeast pacific in ARW-WRF using a modified tiedtke cumulus parameterization scheme. *Monthly Weather Review*, *139*, 3489–3513. https://doi.org/10.1175/MWR-D-10-05091.1

Zhang, J., *Lin, L.F.*, and *Bras, R.L.*, 2020: Effect of logarithmically transformed IMERG precipitation observations in WRF 4D-Var data assimilation system. *Water (Switzerland)*, *12*, 1–12. 10.3390/w12071918

Zheng, H., *Chen, Y.*, *Zheng, S.*, *Meng, D.*, and *Sun, T.*, 2023: Radar Reflectivity Assimilation Based on Hydrometeor Control Variables and Its Impact on Short-Term Precipitation Forecasting. *Remote Sensing*, *15*. 10.3390/rs15030672

Zhu, H., *Wheeler, M.C.*, *Sobel, A.H.*, and *Hudson, D.*, 2014: Seamless precipitation prediction skill in the tropics and extratropics from a global model. *Monthly Weather Review*, *142*. https://doi.org/10.1175/MWR-D-13-00222.1

DOI:10.28974/idojaras.2026.2.4

IDŐJÁRÁS

Quarterly Journal of the HungaroMet Hungarian Meteorological Service
Vol. 130, No. 2, April – June, 2026, pp.151–167

An investigation of the angular distribution of the degree of polarization in natural solar radiation diffusely reflected and transmitted through atmospheric layers

Jurabek Y. Rozikov*, **Makhmud M. Sobirov**, **Valijon U. Ruziboyev**, and **Muhabbat M.Kamolova**

Department of Physics, Fergana State University
Fergana, 150100, Uzbekistan

**Correponding author E-mail: roziqovjurabek1991@gmail.com*

(Manuscript received in final form on June 23, 2025)

Abstract— This study investigates the angular distribution of the degree of polarization of diffusely reflected and transmitted natural solar radiation in atmospheric layers subjected to multiple Rayleigh scattering. The analysis employs the Chandrasekhar's S,T- matrix theory and the factorization method. Specific characteristics related to the numerical computation of *X* and *Y* functions using the successive approximations method are detailed. The results reveal that when the observation angle equals the illumination angle ($\mu = \mu_0$), a notable feature emerges in the angular distribution of the degree of polarization of diffusely transmitted light. At this juncture, a sharp change in the degree of polarization is observed. Additionally, the study examines the dependence of the angular width of this discontinuity on the illumination angle and optical thickness.

Key-words: polarization, optical thickness, S,T-matrices, X,Y-functions, neutral points

1. Introduction

Chandrasekhar's theory of $X(\mu), Y(\mu)$ functions (*Chandrasekhar*, 1960) is widely recognized as a key approach to investigate the transmission of polarized radiation in turbid, light-scattering media with limited optical thicknesses. It is extensively utilized in addressing diverse practical issues in the field of atmospheric physics. Extensive research has been conducted on the analytical properties of the $X(\mu)$ and $Y(\mu)$ functions, as well as on the numerical methods used to solve them. Nevertheless, the subject of $X(\mu), Y(\mu)$ functions remains pertinent and continues to captivate the interest of experts. The research of *Natraj et al.* (2009) and *Natraj* and *Hovenier* (2012) have demonstrated that the often utilized tables by Chandrasekhar and Coulson (*Chandrasekhar* and *Elbert*, 1954; *Coulson*, 1988; *Coulson et al.*, 1960), which are applied for solving practical problems in atmospheric physics, exhibit low accuracy and do not sufficiently characterize polarization phenomena. The authors performed novel numerical computations with enhanced precision. However, research focused on the examination of polarization phenomena in atmospheric layers and the use of polarization methods for remote sensing of the Earth's surface still relies on the works of Chandrasekhar and Coulson. These works serve as reference points for evaluating the outcomes of both theoretical and practical investigations (*Yan et. al.*, 2019; *Yan et. al.*, 2020; *Mishchenko*, 1987; *Mishchenko et. al.*, 2006).

A technique for solving the radiative transfer equation for polarized light in media with limited optical thickness using the factorization method was proposed in *Sobirov and Rozikov* (2020). This method aims to refine the theoretical framework and improve the precision of numerical calculations. The findings demonstrate that the factorization method significantly simplifies both the analytical and numerical computations involved in solving the radiative transfer equation for polarized radiation. Initially developed by *Lenoble* (1970), this approach was further elaborated upon in *Ivchenko et. al.* (1980), *Ivchenko et. al.* (1981), *Sobirov* and *Yuldashev* (1984), and *Pikus et. al.* (1985), and it was effectively applied to axisymmetric problems in crystals, particularly within the semi-infinite medium model. The present study investigates the angular distribution of the degree of polarization of diffusely reflected and transmitted natural solar radiation through atmospheric layers, considering multiple Rayleigh scattering. The analysis is grounded in the theoretical framework outlined in *Sobirov and Rozikov* (2020).

2. Equation for the reflection and transmission matrix

The radiative transfer equation (*Chandrasekhar*, 1960) describes the radiation field in a plane-parallel medium that scatters and absorbs light, without any internal sources, when it is lit by plane, monochromatic polarized radiation. The

equation can be written as follows:

$$\mu \frac{d\mathbf{I}(\tau,\mathbf{\Omega})}{\mathrm{d}\tau} = \mathbf{I}(\tau,\mathbf{\Omega}) - \frac{\widetilde{\omega}_0}{4\pi}\int_0^1 d\mu' \int_0^{2\pi} d\varphi' \, \mathbf{P}(\mathbf{\Omega},\mathbf{\Omega}')\mathbf{I}(\tau,\mathbf{\Omega}') - \\ - \frac{\widetilde{\omega}_0}{4}\exp\left(-\frac{\tau}{\mu_0}\right)\mathbf{P}(\mathbf{\Omega},\mathbf{\Omega_0})\mathbf{F}, \qquad (1)$$

where τ represents the optical thickness of the medium, $\widetilde{\omega}_0$ is the single scattering albedo (quantum yield of single scattering) calculated as $\frac{a^{\mathrm{sc}}}{\alpha^{\mathrm{ext}}+a^{\mathrm{sc}}}$, α is the attenuation coefficient (per unit volume) given by $\alpha = \alpha^{\mathrm{abs}} + a^{\mathrm{sc}}$, α^{abs} denotes the true absorption coefficient, a^{sc} represents the scattering coefficient, z is the axis directed normally from the surface of the medium, $\pi\boldsymbol{F}$ is the total flux of the incident parallel radiation per unit area (at the boundary $\tau = 0$), and $\boldsymbol{P}(\mathbf{\Omega}, \mathbf{\Omega_0})$ is the Rayleigh phase matrix.

The intensity of radiation propagating in a medium, in the direction $\Omega = \Omega(\theta,\varphi)$ (where θ is the polar angle determined by the direction of the vectors $\boldsymbol{n^0}$ and Ω, $\boldsymbol{n^0}$ is the normal to the surface of the medium, and φ is the azimuthal angle), is described by the Stokes matrix (in the Chandrasekhar basis (*Chandrasekhar*, 1960)):

$$\mathbf{I} = \begin{bmatrix} I_l \\ I_r \\ U \\ V \end{bmatrix}, I_l = d_{ll}, I_r = d_{ll}, \mathrm{U} = 2\mathrm{Re}d_{lr}, V = 2\mathrm{Im}d_{lr}, \qquad (2)$$

where I_l and I_r are the intensities in the l and r polarizations, the unit orthogonal vector $\mathbf{l}$ lies in the plane of the vectors $\boldsymbol{n^0}$ and $\boldsymbol{\Omega}$, and $\boldsymbol{r}$ is perpendicular to it, $d_{ij} \approx \left(E_i, E_j^*\right)$. Here, $i,j = l,r,E_l$, and E_r are the corresponding components of the electric field of the light wave.

When the atmosphere is illuminated by natural, unpolarized solar radiation with a broad spectrum in the optical range, the optical thickness of the atmosphere varies depending on the wavelength of the light. In the radiative transfer equation (Eq.(1)), the optical thickness of the atmosphere τ is determined by the integral:

$$\tau(\lambda, z) = \int_0^\infty \alpha(\lambda, z)dz, \qquad (3)$$

where the integration is performed from sea level ($z = 0$) to the upper layers of the atmosphere, taking into account the change in air concentration with height. In the calculations presented below, the values of the optical thickness of the atmosphere are taken from *Coulson* (1988) according to the tables of Elterman (*Elterman*, 1968*; Pikus et. al.*, 1985). We present the values of optical thickness

for several wavelengths: τ = 0.01 (λ = 0.920 μm), τ = 0.1 (λ = 0.546 μm), τ = 0.15 (λ = 0.495 μm), τ = 0.5 (λ = 0.371 μm), and τ = 1 (λ = 0.312 μm) at $\widetilde{\omega}_0$ =1.

In the theory of S,T-matrices, the relationship between the intensities of diffusely reflected and transmitted radiation with the incident radiation is determined by the reflection and scattering matrices:

$$I_{\text{ref}}(\tau = 0, \Omega) = \left(\frac{\widetilde{\omega}_0}{4\mu}\right) S(\tau_1, \Omega, \Omega_0) F\left(\tau = 0, \overline{\Omega}_0\right). \tag{4}$$

$$I_{\text{trans}}\left(\tau = \tau_1, \overline{\Omega}\right) = \left(\frac{\widetilde{\omega}_0}{4\mu}\right) T(\tau_1, \Omega, \Omega_0) F\left(\tau = 0, \overline{\Omega}_0\right). \tag{5}$$

Using the principle of Ambartsumian's invariance and taking into account the boundary conditions from the radiative transfer equation (Eq.(1)), the general integral equations for the $\boldsymbol{S}$ and $\boldsymbol{T}$ matrices can be derived (*Chandrasekhar*, 1960):

$$\begin{aligned}\boldsymbol{S}(\tau_1, \Omega, \Omega_0) = \boldsymbol{Q}\Big\{&\left(\frac{3}{4}\right)\boldsymbol{S}^{(0)}(\tau_1, \mu, \mu_0) \; + \\ &+\sqrt{(1-\mu^2)(1-\mu_0^2)}\boldsymbol{S}^{(1)}(\tau_1, \Omega, \Omega_0)\boldsymbol{P}^{(1)}(\mu, \phi, -\mu_0, \phi_0) + \\ &S^{(2)}(\tau_1, \mu, \mu_0)\boldsymbol{P}^{(2)}(\mu, \phi, -\mu_0, \phi_0)\Big\}.\end{aligned} \tag{6}$$

$$\begin{aligned}\boldsymbol{T}(\tau_1, \Omega, \Omega_0) = \boldsymbol{Q}\Big\{&\left(\frac{3}{4}\right)\boldsymbol{T}^{(0)}(\tau_1, \mu, \mu_0) + \\ &+\sqrt{(1-\mu^2)(1-\mu_0^2)}\boldsymbol{T}^{(1)}(\tau_1, \Omega, \Omega_0)\boldsymbol{P}^{(1)}(\mu, \phi, -\mu_0, \phi_0) + \\ &+T^{(2)}(\tau_1, \mu, \mu_0)\boldsymbol{P}^{(2)}(\mu, \phi, -\mu_0, \phi_0)\Big\}.\end{aligned} \tag{7}$$

In Eqs.(1)–(7), the problem is presented in general form. In Eq.(1), all four components of the Stokes matrix are simultaneously determined, taking into account both linearly polarized and circularly polarized radiation. For brevity, we will discuss the solution of the problem concerning only the I_l and I_r components of the Stokes matrix, as we are considering the case where the medium is illuminated by unpolarized radiation.

To solve this problem, it is sufficient to consider the 2x2 block matrices in the $\boldsymbol{S}$ and $\boldsymbol{T}$ matrices in Eqs. (6) and (7). For brevity, we will not go into detail describing each term in Eqs. (6) and (7) (see *Sobirov* and *Rozikov*, 2020).

In the factorization method, the values of the $\boldsymbol{S}^{(0)}$ and $\boldsymbol{T}^{(0)}$ matrices in Eqs. (6) and (7) are determined by solving the system of equations for the $\boldsymbol{X}^{(0)}$ and $\boldsymbol{Y}^{(0)}$ matrices, which are 2x2 matrices with eight components:

$$\boldsymbol{X}^{(0)}(\mu) = \mathbf{1} + \mu\widetilde{\omega}_0 \int_0^1 \frac{d\mu'\Psi(\mu')}{\mu+\mu'}\left[\boldsymbol{X}^{(0)}(\mu)\boldsymbol{X}^{(0)^+}(\mu') - \boldsymbol{Y}^{(0)}(\mu)\boldsymbol{Y}^{(0)^+}(\mu')\right]. \quad (8)$$

$$\boldsymbol{Y}^{(0)}(\mu) = \mathbf{1}\exp\left(-\frac{\tau_1}{\mu}\right) + \mu\widetilde{\omega}_0 \int_0^1 \frac{d\mu'\Psi(\mu')}{\mu-\mu'}\left[\boldsymbol{Y}^{(0)}(\mu)\boldsymbol{X}^{(0)^+}(\mu') - \right.$$
$$\left. - \boldsymbol{X}^{(0)}(\mu)\boldsymbol{Y}^{(0)^+}(\mu')\right]. \quad (9)$$

Here, the identity matrix has a dimension of 2x2. The $\boldsymbol{S}^{(1)}$, $\boldsymbol{T}^{(1)}$, $\boldsymbol{S}^{(2)}$, and $\boldsymbol{T}^{(2)}$ matrices are determined through scalar functions $S^{(1)}$, $T^{(1)}$, $S^{(2)}$, and $T^{(2)}$, which, in turn, are determined by scalar integral equations for the $X(\mu)$ and $Y(\mu)$ functions, similarly to Eqs. (8) and (9), but using different characteristic functions.

According to Chandrasekhar's calculation method, the values of the $\boldsymbol{S}^{(0)}$ and $\boldsymbol{T}^{(0)}$ matrices are determined using four $X(\mu)$ and $Y(\mu)$ functions. However, this requires additional and complex calculations.

2.1. Iterative convergence of X and Y functions in a conservative medium when $\widetilde{\omega}_0 = 1$

Below are the results of numerical calculations of the $X(\mu)$ and $Y(\mu)$ functions obtained using the method of successive approximations or iterations. In the iteration method for solving Eqs. (3) and (4), the solution can be represented as a series in powers of $\widetilde{\omega}_0$ (*Lenoble*, 1970 and *Pikus et. al.*, 1985):

$$\boldsymbol{I}_{\text{ref}}(\tau_1 = 0, \Omega) = \sum\left(\frac{\widetilde{\omega}_0^n}{4\mu}\boldsymbol{S}^{(n)}(\tau_1, \overline{\Omega}, \Omega_0)\boldsymbol{F}\right), \quad (10)$$

$$\boldsymbol{I}_{\text{trans}}(\tau_1, \Omega) = \sum\left(\frac{\widetilde{\omega}_0^n}{4\mu}\boldsymbol{T}^{(n)}(\tau_1, \Omega, \Omega_0)\boldsymbol{F}\right), \quad (11)$$

where n is the order or multiplicity of scattering (*Mishchenko et.al.*, 2006; *Sobirov* and *Rozikov*, 2020; *Lenoble*, 1970; *Ivchenko et.al.*, 1980, 1981). The $\boldsymbol{S}^{(n)}(\tau_1, \Omega, \Omega_0)$ and $\boldsymbol{T}^{(n)}(\tau_1, \Omega, \Omega_0)$ are determined by solving the $\boldsymbol{S}$ and $\boldsymbol{T}$ matrices, expressed through integral equations for the $X(\mu)$ and $Y(\mu)$ functions using the method of successive approximations. If trial functions such as $\boldsymbol{X}(\mu) = 1$ and $\boldsymbol{Y}(\mu) = \mathbf{1}\exp(-\tau_1/\mu)$ are used, then after the first iteration, the intensity and polarization of singly scattered radiation are determined. After the first iteration, the scattering order does not correspond to the number of iterations. In the second approximation, the values of $X(\mu)$ and $Y(\mu)$ include contributions from singly, doubly, and partially triply scattered radiation, and so on.

Analytically, in Eq.(10), components up to the fourth order of scattering can

be distinguished, after which it becomes more complex. However, this is sufficient for the initial analysis of the physical picture of the formation of the intensity and polarization of secondary radiation. It is possible to establish a relationship between the number of iterations and the maximum order of scattering corresponding to this number of iterations. If $\tilde{n}$ is the number of iterations and n is the maximum order of scattering, then $\tilde{n} = 1, n = 1; \tilde{n} = 2, n = 3; \tilde{n} = 3, n = 7; \tilde{n} = 4, n = 15; \tilde{n} = 5, n = 31; \tilde{n} = 6, n = 63$, etc.

The solutions to the system of nonlinear integral equations for the $X(\mu)$ and $Y(\mu)$ functions were conducted at 201 points of μ values in the interval [0,1] through numerical calculations. Additionally, to compare our results with Chandrasekhar's tables, calculations were performed at fifty-one points.

To ensure the correctness of the numerical calculations, two conditions must be met (*Chandrasekhar*, 1960):

$$X(\mu) \to H(\mu), Y(\mu) \to 0 \text{ as } \tau \to \infty. \tag{12}$$

$$X(\mu) \to 1, Y(\mu) \to 1\exp(-\tau_1/\mu) \text{ as } \tau \to 0. \tag{13}$$

Indeterminacies of the type $0/0$ arising in Eq.(9) when $\mu - \mu' = 0$ are eliminated using Lopital's rule.

Numerical calculations showed that in the region $\widetilde{\omega}_0 < 0.7$, after a certain number of iterations, the values of all X and Y functions reach saturation and have good convergence at $\tau_1 \leq 1$ (*Sobirov et al.*, 2021; *Sobirov et al.*, 2023; *Sobirov et al.*, 2024). In the region $0.7 < \widetilde{\omega}_0 \leq 1$, convergence slows down, but depending on the optical thickness, the values of the *X* and *Y* functions approach the tabulated values of Chandrasekhar in *Chandrasekhar* and *Elbert* (1954). For example, at $\tau_1 = 0.15$ after the fifth iteration, and at $\tau_1 = 1$, after the fourth iteration. At small values of optical thickness, when $\tau_1 < 0.5$, the difference in some points is a maximum of 1%, and at $\tau_1 = 1$, it points up to 4%.

If in the case of $\tau_1 = 1$ the number of iterations is increased to $\tilde{n} = 5$, then near the point $\mu = 1$, in a narrow region $\Delta\mu$, the component $Y_{21}(\mu)$ takes negative values, which contradicts the conditions specified in Eq.(13). This means that at values of μ within $\Delta\mu$, the component $Y_{21}(\mu)$ has no solution. Considering that all $X_{11}, X_{12}, X_{21}, X_{22}, Y_{11}, Y_{12}, Y_{21}, Y_{22}$ functions form a single system of equations, all members of this system within $\Delta\mu$ also have no solution. It can be said that with the number of iterations $\tilde{n} = 4$, the values of all $X_{11}, X_{12}, X_{21}, X_{22}, Y_{11}, Y_{12}, Y_{21}, Y_{22}$ functions within $\Delta\mu$ reach saturation. In the subsequent iteration step (at $\tilde{n} = 5$), the values of these functions remain unchanged. However, in the region $1 - \Delta\mu$, the values of the $X_{11}, X_{12}, X_{21}, X_{22}, Y_{11}, Y_{12}, Y_{21}, Y_{22}$ functions increase. Increasing the number of iterations leads to the expansion of the $\Delta\mu$ region, and after two or three more iterations, $\Delta\mu$ covers the entire region $0 \leq \mu \leq 1$. The values of the $X(\mu)$ and

$Y(\mu)$ functions are determined by the iteration method according to the described scheme. A change in the sign of the $Y_{21}(\mu)$ component to negative indicates the achievement of the maximum number of iterations that determine the numerical values of the $X(\mu)$ and $Y(\mu)$ functions. The $X^{(1)}(\mu), Y^{(1)}(\mu), X^{(2)}(\mu), Y^{(2)}(\mu)$ functions show good convergence during iterations, regardless of the τ_1 value. After a certain number of iterations, they reach saturation and with an error of up to 1% coincide with the tabulated values in *Chandrasekhar* and *Elbert* (1954).

For comparison, Chandrasekhar's $\psi, \phi, \chi, \xi, \varepsilon, \eta, \sigma, \theta$ functions were converted into $X_{11}, X_{12}, X_{21}, X_{22}, Y_{11}, Y_{12}, Y_{21}, Y_{22}$ functions, and the following relationships exist between them:

$$X_{11} = \chi, X_{12} = \sqrt{2}\xi, X_{21} = \frac{\psi - \mu^2\chi}{\sqrt{2}(1-\mu^2)}, X_{22} = \frac{\phi - \mu^2\xi}{1-\mu^2}. \quad (14)$$

$$Y_{11} = \sigma, Y_{12} = \sqrt{2}\theta, Y_{21} = \frac{\varepsilon - \mu^2\sigma}{\sqrt{2}(1-\mu^2)}, Y_{22} = \frac{\eta - \mu^2\theta}{1-\mu^2}. \quad (15)$$

2.2. Accuracy verification of the problem solution. Total quantum yield of radiation

In the studies of *Ivchenko et.al.* (1980, 1981) and *Sobirov* and *Yuldashev* (1984), the law of conservation of the total radiation flux, incident and diffusely reflected from a semi-infinite medium, was used to verify the accuracy of analytical and numerical calculations.

If a monochromatic, plane-parallel radiation flux πF falls on the surface of the medium (at the boundary $\tau = 0$), then after multiple scattering, part of the radiation is diffusely reflected from the plane $\tau = 0$, and part of the flux diffusely exits the medium through the plane $\tau = 1$. The total fluxes of diffusely reflected and transmitted radiation from the medium (per unit surface area) are determined by the formulas:

$$\pi\Phi^{ref} = \int_0^1 \mu d\mu \int_0^{2\pi} d\varphi I^{ref}(\tau = 0, \mu, \varphi),$$

$$\pi\Phi^{trans} = \int_0^1 \mu d\mu \int_0^{2\pi} d\varphi I^{trans}(\tau = \tau_1, -\mu, \varphi), \quad (16)$$

where $I^{(ref)}(\tau = 0, \mu, \varphi)$ and $I^{(trans)}(\tau = \tau_1, -\mu, \varphi)$ are the intensities of diffusely reflected and transmitted radiation at the boundary of the medium, determined by Eq.(10).

Solving the radiative transfer equation (Eq.(1)) allows determining only the diffusely scattered part of the incident flux in the medium that has undergone single or multiple scattering. However, part of the incident flux passes through the medium without scattering, which is not considered in Eq.(1). The unscattered part of the primary radiation, without changing the direction of incidence, is attenuated by $\exp(-\tau_1/\mu_0)\pi F$ and exits the medium (*Chandrasekhar*, 1960). We define the ratios of these three fluxes to the incident flux and sum them:

$$\eta^{ref} = \frac{\Phi^{\mathrm{ref}}}{\mu_0 F(+0,\mu_0,\varphi_0)}, \eta^{trans} = \frac{\Phi^{\mathrm{trans}}}{\mu_0 F(+0,\mu_0,\varphi_0)}. \quad (17)$$

$$\eta^{total} = \eta^{ref} + \eta^{trans} + \exp\left(-\frac{\tau_1}{\mu_0}\right). \quad (18)$$

This formula defines the distribution of the primary flux for diffusely reflected, diffusely transmitted, and unscattered fluxes. In analogy to $\widetilde{\omega}_0$, which represents the quantum yield from single scattering, the quantity η_{total}, is called the total quantum yield of radiation in (*Ivchenko et.al.*, 1980). Below, we will adhere to this definition for η.

In the case of a conservative medium ($\widetilde{\omega}_0 = 1$), the total flux is conserved, so in Eq.(18) the condition $\eta_{\mathrm{total}} = 1$ must be satisfied. This condition holds regardless of the optical thickness of the medium, the angle of incidence of the incident flux, and serves as a criterion for assessing the accuracy of analytical and numerical calculations. On the other hand, the relationship described in Eq.(18) allows establishing the law of redistribution of the outgoing secondary flux from the medium depending on the optical thickness of the medium (from the wavelength of the incident radiation).

Table 1 presents the results of numerical calculation of the total quantum yield at various values of the illumination angle of atmospheric layers with natural, unpolarized solar radiation.

According to the data in *Table 1*, one can assess what proportion of the incident radiation is scattered, and what part is diffusely reflected back or passes through the medium. For example, at normal incidence, on average about 10% of the rays from the green part of the spectrum ($\tau_1 = 0.1,\ \lambda = 0.546\ \mu\mathrm{m}$) are scattered, and 90% pass through the medium without scattering. For violet rays ($\tau_1 = 0.5, \lambda = 0.37\ \mu\mathrm{m}$), the proportion of scattered rays increases to approximately 40%.

Table 1. Results of calculating the total quantum yield of diffusely reflected, transmitted, and unscattered radiation at various illumination angles and optical thicknesses, $\widetilde{\omega}_0 = 1$

μ_0	η_{ref}	η_{trans}	$\eta_{ref} + \eta_{trans}$	$\exp(-\tau_1/\mu_0)$	η_{total}
		$\tau_1 = 0.001,\ \lambda = 1.670\ \mu m$			
0	0.50295806	0.4913439	0.99430193	0	0.9943019
0.2	0.01235285	0.0132404	0.02559321	0.9950124	1.0206056
0.4	0.00622429	0.0065941	0.01281842	0.9975031	1.0103215
0.6	0.00416402	0.0043620	0.00852599	0.9983347	1.0068607
0.8	0.00313426	0.0032165	0.00635071	0.9987507	1.0051014
1	0.00267292	0.0019598	0.00463271	0.9990005	1.0036332
		$\tau_1 = 0.01,\ \lambda = 0.920\ \mu m$			
0	0.508344001	0.4859448	0.99428885	0	0.99428885
0.2	0.024403672	0.0261452	0.05054884	0.9512294	1.00177826
0.4	0.012372619	0.0131070	0.02547959	0.9753099	1.00078950
0.6	0.008294686	0.0086864	0.01698112	0.9834715	1.00045258
0.8	0.006250375	0.0064061	0.01265651	0.9875778	1.00023431
1	0.005342862	0.0039199	0.00926272	0.9900498	0.99931256
		$\tau_1 = 0.1,\ \lambda = 0.546\ \mu m$			
0	0.57015844	0.4240466	0.9942055	0	0.9942050
0.2	0.19901661	0.2075493	0.4065658	0.6065306	1.0130965
0.4	0.11129502	0.1174036	0.2286986	0.7788007	1.0074994
0.6	0.07712613	0.0812964	0.1584225	0.8464817	1.0049043
0.8	0.05902330	0.0620124	0.1210357	0.8824969	1.0035326
1	0.04915566	0.0376694	0.0868205	0.9048374	0.9916625
		$\tau_1 = 0.5,\ \lambda = 0.371\ \mu m$			
0	0.68443190	0.2992614	0.98369334	0	0.98369333
0.2	0.51703888	0.4047164	0.92175532	0.0820858	1.00384031
0.4	0.37843796	0.3487235	0.72716148	0.2865048	1.01366627
0.6	0.29298172	0.2868027	0.57978439	0.4345982	1.01438266
0.8	0.23799182	0.2419630	0.47995479	0.5352614	1.01521622
1	0.20055734	0.1893865	0.38994375	0.6065306	0.99647436
		$\tau_1 = 1,\ \lambda = 0.312\ \mu m$			
0	0.73773050	0.2118047	0.94953523	0	0.9495352
0.2	0.62204550	0.3232367	0.94528369	0.0067380	0.9520216
0.4	0.51901118	0.3683299	0.88734110	0.0820850	0.9694261
0.6	0.43571001	0.3592421	0.79495200	0.1888756	0.9838277
0.8	0.37285681	0.3364988	0.70935550	0.2865048	0.9958604
1	0.32561385	0.2874323	0.61304610	0.3678794	1.0098093
		$\tau_1 \to \infty$			
0	0.992526938	0	0.992526938	0	0.992526938
0.2	0.999637976	0	0.999637976	0	0.999637976
0.4	0.999804808	0	0.999804808	0	0.999804808
0.6	0.999927438	0	0.999927438	0	0.999927438
0.8	1.000042373	0	1.000042373	0	1.000042373
1	1.000146482	0	1.000146482	0	1.000146482

From the table, it can be seen that in the long-wavelength part of the spectrum, regardless of the angle of incidence, the proportions of diffusely reflected and transmitted radiation in the total quantum yield are almost identical. In the short-wavelength part of the spectrum, diffusely reflected radiation predominates. This is explained by the fact that with increasing optical thickness of the medium, the flux of transmitted diffuse and unscattered radiation decreases.

For comparison, similar calculations were performed using the tabulated values of the $\psi, \varphi, \chi, \xi, \varepsilon, \eta, \sigma, \theta$ functions from the work of *Chandrasekhar* and *Elbert* (1954). The results of the calculations showed that when the medium is illuminated normally and near this point ($\mu_0 \to 1$), at all values of optical thickness, the value of the total quantum yield exceeds the expected value, reaching up to 9% in certain points (*Table 2.*). However, in our calculations, deviations are observed in the region $\mu_0 \to 1$, which are lower than expected and amount to up to 5%. The probable cause of the disappearance of part of the short-wavelength radiation is the insufficiently accurate accounting for the number of scatterings and the diffuse radiation exiting the medium at $\mu_0 \to 1$, in the iteration method. In the geometry of medium illumination when $\mu_0 \to 1$, short-wavelength radiation travels a long optical path in the medium and undergoes multiple scatterings. It is likely that in the iterative method of solving equations, part of the radiation is not taken into account, which may explain the observed deviation. In the case of a semi-infinite medium ($\tau_1 \to \infty$), the results of our calculations and those using Chandrasekhar's functions coincide, and the law of conservation of total flux is satisfied with high accuracy.

Table 2. Calculation results based on the values of the $\psi, \varphi, \chi, \xi, \varepsilon, \eta, \sigma, \theta$ functions in Chandrasekhar and Elbert (1954)

μ_0	η_{ref}	η_{trans}	$\eta_{ref} + \eta_{trans}$	$\exp(-\tau_1/\mu_0)$	η_{total}
			$\tau_1 = 0.2$		
0	0.61821120	0.3819794	1.00019055	0	1.00019055
0.20	0.32777708	0.3249194	0.65269643	0.3678794	1.02057587
0.44	0.18579127	0.1871951	0.37298640	0.6347364	1.00772282
0.68	0.12879399	0.1377657	0.26655965	0.7451888	1.01174847
0.92	0.09839073	0.1893681	0.28775880	0.8046151	1.09237385
1	0.09119335	0.1623395	0.25353290	0.8187308	1.07226365
			$\tau_1 = 1$		
0	0.765023981	0.2329303	0.99795427	0	0.9979543
0.20	0.648421603	0.3520141	1.00043574	0.0067379	1.0071737
0.44	0.524457435	0.3993407	0.92379817	0.1030308	1.0268290
0.68	0.427572533	0.3808561	0.80837256	0.2297903	1.0381628
0.92	0.357323733	0.4007442	0.75806795	0.3372413	1.0953093
1	0.338355703	0.3627337	0.70108936	0.3678794	1.0689688

According to the data in *Table 1*, it can be concluded that if calculations are carried out using Chandrasekhar's method, some difficulties can be expected in the calculations for $\mu_0 \to 1$, across the entire optical spectrum. Apparently, for this reason, Coulson's monograph does not consider the case, where the angle of incidence of the solar rays is normal to the surface of the medium and for values of angles close to the normal. When performing calculations using our method,

such discrepancies are observed only in the short-wavelength region of the spectrum at $\mu_0 \to 0$.

Coulson's monograph mentions that in the ultraviolet wavelength region, some difficulties are observed in the calculations. He attributes these difficulties to the data in Elterman's table.

The results in *Table 1* allow us to evaluate the proportion of incident radiation that is scattered, diffusely reflected back, or transmitted through the medium. For example, at normal incidence, approximately 10% of the rays from the green part of the spectrum ($\tau_1 = 0.1, \lambda = 0.546$ μm) are scattered, and 90% pass through the medium without scattering. For violet rays ($\tau_1 = 0.5, \lambda = 0.371\ \mu m$), the proportion of scattered rays increases to approximately 40%.

It can be seen from the table that in the long-wavelength part of the spectrum, regardless of the angle of incidence, the proportions of diffusely reflected and transmitted radiation in the total quantum yield are almost identical. In the short-wavelength part of the spectrum, diffusely reflected radiation predominates. This is because, with increasing optical thickness of the medium, the flux of transmitted diffuse and unscattered radiation decreases.

3. Calculation of the angular characteristics of the secondary radiation intensity considering various orders of scattering

The incident unpolarized radiation has the following Stokes parameters:

$$F_l = F_r = (1/2)F, F_U = F_V = 0, \tag{19}$$

and the degree of linear polarization of diffusely reflected and transmitted radiation is determined by the formula:

$$P_{lin} = (I_l - I_r)/(I_l + I_r). \tag{20}$$

Figs. 1 – 4 show the results of calculations of the angular characteristics of the degree of linear polarization of diffusely reflected and transmitted radiation from the medium. The incident, reflected, and transmitted radiation lie in the same meridional plane, in the plane of the solar vertical.

Fig. 1 shows the results of the calculation of the angular distribution of the degree of polarization of transmitted radiation for various illumination angles. For comparison, calculations were made using Coulson's parameters (see Figure 4.6 in *Coulson* (1988)) at an optical thickness of $\tau_1 = 0.15$ ($\lambda = 0.495$ μm).

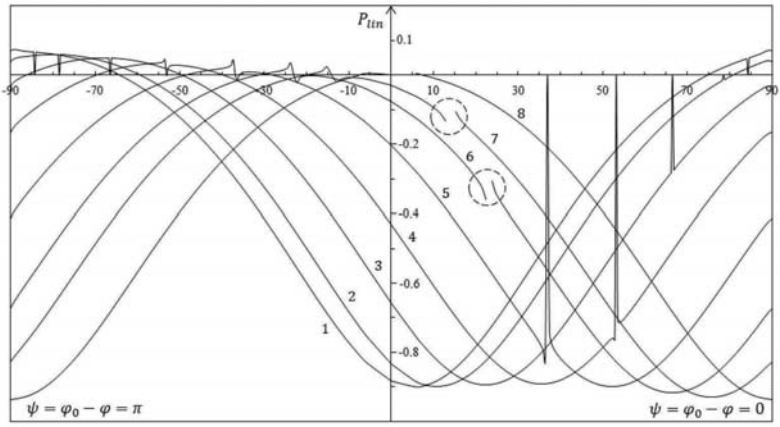

Fig. 1. Angular distribution of the degree of polarization of diffusely transmitted radiation at various illumination angles. Curves 1–8 are calculated for medium illumination angles μ_0 = 0.1, 0.2, 0.4, 0.6, 0.8, 0.92, 0.97, respectively, at τ_1 = 0.15 (λ = 0.495 μm), $\widetilde{\omega}_0 = 1$. The calculations are based on the Coulson's parameter values (Figure 4.6 in *Coulson* (1988)).

It can be observed that all angular distributions of the degree of polarization, calculated at different illumination angles, coincide with Coulson's results with high accuracy. However, in our calculations, when the polar illumination angle is equal to the observation angle ($\tilde{\mu} = \mu = \mu_0$), an anomaly is observed in the value of the degree of polarization. Near this point, the degree of polarization changes abruptly. For a clearer representation of this phenomenon, in curves 6 and 7, the regions around the point $\tilde{\mu}$, where the degree of polarization behaves anomalously, are highlighted separately.

With a change in the angle of illumination, the width of the anomalous region changes: it decreases when $\mu_0 \to 0$ and increases when $\mu_0 \to 1$.

For comparison, in *Fig. 2*, the results of similar calculations of the angular distribution of the degree of polarization are presented for an optical thickness of $\tau_1 = 1$ ($\lambda = 0.312$ μm). From the figure, it is evident that with an increase in optical thickness, the angular width of the anomalous region expands, and the jump in the degree of polarization value around the point $\tilde{\mu} = \mu = \mu_0$ increases.

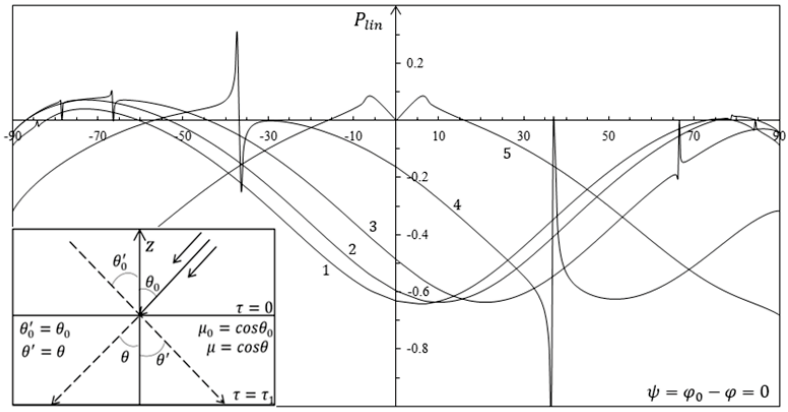

Fig. 2. Angular distribution of the degree of polarization of diffusely transmitted radiation at various illumination angles. Curves 1–5 are calculated for medium illumination angles μ_0= 0.1, 0.2, 0.4, 0.8, 1, respectively, at τ_1 = 1 (λ = 0.312 μm), $\widetilde{\omega}_0 = 1$.

For the parameters $\tau = 1$ and $\mu_0 \approx 0.8$, the angular width of the anomalous region in the half-plane $\psi = \pi$ is $\Delta\tilde{\theta} \approx 4°$, and in the half-plane $\psi = 0$, $\Delta\tilde{\theta} \approx 6°$. In the case of $\tau = 0.15$ and $\mu_0 \approx 0.8$, the angular widths are $\Delta\tilde{\theta} \approx 1°$ and $\Delta\tilde{\theta} \approx 3°$, respectively. The angular width of the anomalous region in the solar plane is larger than in the anti-solar half-plane.

In the geometry of normal illumination and observation ($\mu = \mu_0 = 1$), the degree of polarization is zero. The jump in the degree of polarization takes on a symmetrical form. With a deviation of the observation angle from the normal, at $\mu < 1$, the degree of polarization first assumes a positive value, then it transitions to the negative region through neutral points.

The anomaly in the degree of polarization is observed for all values of optical thickness, as well as in the case of a non-conservative medium ($\widetilde{\omega}_0 < 1$). With a decrease in the albedo value, the anomalous polarization diminishes.

It should be noted that the aforementioned feature is observed for all azimuthal angles of the hemisphere around the lower boundary of the atmosphere at $\tilde{\mu} = \mu = \mu_0$.

The presence of a singularity in the solutions of the transfer equation for transmitted radiation at $\tilde{\mu} = \mu = \mu_0$ is known (*Natraj et.al.*, 2009; *Kattawar et al.*, 1976), but in these works, the jump in the degree of polarization around this point is not discussed. Apparently, this feature was not established. If the indicated jump in the degree of polarization is indeed observed, then during observations through a polarimeter along the solar vertical, it is possible to detect a difference in the degree of polarization of solar radiation at symmetric points near the sun. This

feature was observed during double Mandelstam-Brillouin scattering of exciton polaritons in crystals with cubic symmetry (*Ivchenko* and *Sobirov*, 1985).

In the angular distribution of the degree of polarization along the plane of the solar vertical, at certain points, the degree of polarization changes sign, with the degree of polarization equaling zero at these points. These neutral points (Brewster, Babinet, and Arago) serve as indicators of the atmospheric state. Besides these points, the presence of a fourth point, near the Arago point, was also proposed. The presence of double Arago points was theoretically first shown in the work of *Dave* and *Furukawa* (1966) when studying the scattering of ultraviolet rays in the atmosphere. However, these calculations were performed outside the framework of the $X(\mu), Y(\mu)$–function theory. This point was discovered in observations only recently, in 2002, and the topic of neutral points constantly remains in the focus of specialists (*Horvath et al.*, 2002; *Horvath et al.*, 2011).

Unlike the Brewster and Babinet points, the observation of double Arago points requires higher orders of scattering. For this reason, these points are observed only in the short-wave part of the optical spectrum. Our calculation results show that the presence of double Arago points can be demonstrated within the framework of the $X(\mu), Y(\mu)$ – function theory in the range of illumination angle values $0 < \mu_0 \leq 0.2$ and optical thickness $0.85 < \tau_1 < 1.15$. *Fig. 3* shows the formation of double Arago points in the angular distribution of the degree of polarization of transmitted radiation, depending on the number of scatterings. It should be noted that Coulson's works discuss only one Arago point.

Fig. 4 presents the results of calculations of diffusely reflected solar radiation from atmospheric layers for the parameter values used in *Fig. 1*. For all values of illumination and observation angles, as well as optical thicknesses, in the angular polarization characteristics of diffusely reflected radiation, a jump in the degree of polarization is not observed, with only one Arago point being present.

In conclusion, it should be noted that the developed method for calculating the $X(\mu), Y(\mu)$ – functions significantly simplifies the calculation of the intensity and degree of polarization of diffusely reflected and transmitted solar radiation from atmospheric layers for all points of the hemisphere adjacent to the lower and upper surfaces of the atmosphere.

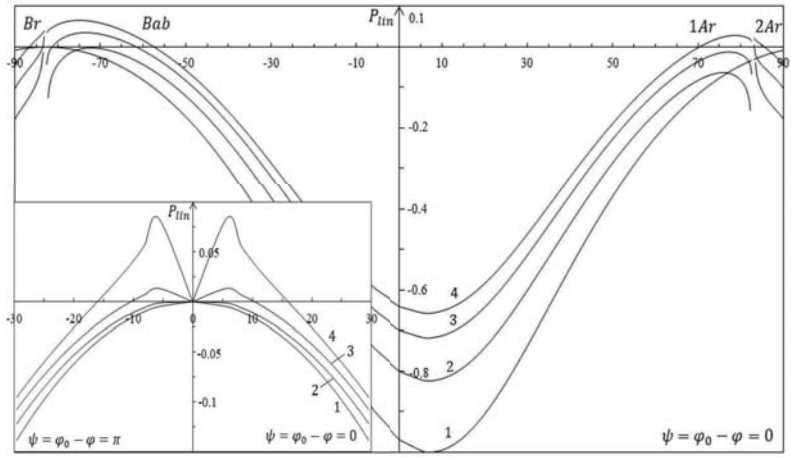

Fig. 3. Formation of double Arago points depending on the number of scatterings. Curves 1–4 correspond to the number of iterations n = 1, 2, 3, 4 (scattering order $\nu = 1, 3, 7, 15$,respectively) for $\tau_1 = 0.9$ and $\mu_0 = 0.125$. The inset shows the formation of the region with positive polarization depending on the multiplicity of scattering for $\tau_1 = 1$ and $\mu_0 = 1$ (curve 5 in *Fig. 2*).

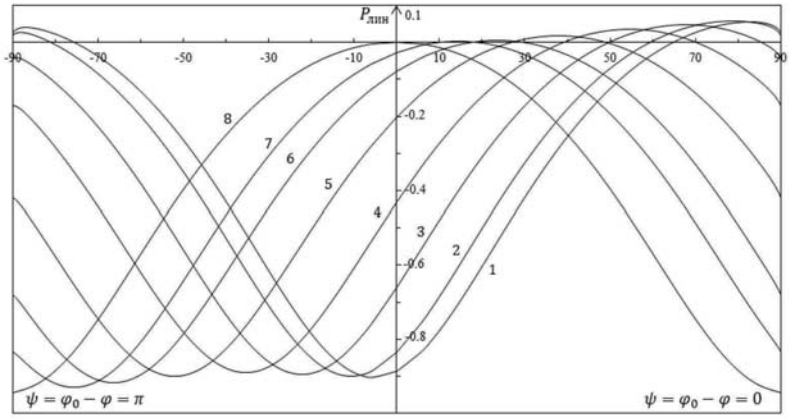

Fig. 4. Angular distribution of the degree of polarization of diffusely reflected radiation at different illumination angles. Curves 1–8 are calculated for the parameter values indicated in *Fig. 1*.

4. Conclusions

1. The solutions of the radiative transfer equation for polarized radiation in a medium with finite optical thickness, obtained using the factorization method, have been analyzed. Based on the obtained equations, the angular distribution of the degree of polarization of diffusely reflected and transmitted radiation from layers of the atmosphere of natural, unpolarized solar radiation along the solar vertical was investigated.

2. It has been shown that in the case of forward scattering of incident radiation, a feature is observed in the angular distribution of the degree of polarization of diffusely transmitted radiation. At μ=μ_0, the degree of polarization of the transmitted radiation changes abruptly within a narrow angular width of observations.

3. The positions of neutral points in the angular characteristics of secondary radiation have been studied. It has been shown that in certain regions of illumination angle and optical thickness values in the angular distribution of the degree of polarization of diffusely transmitted radiation, it is possible to simultaneously observe two Arago points.

4. The results of numerical calculations show that the iteration method is an effective method for determining the numerical values of the *X(μ), Y(μ)* functions obtained by the factorization method. The calculation method is very simple and does not require a long time for computer computations.

ORCID:
Jurabek Y. Rozikov, https://orcid.org/0000-0003-3820-2962
Makhmud M. Sobirov, https://orcid.org/0000-0002-6447-0728
Valijon U. Ruziboyev, https://orcid.org/0000-0002-6199-1165

References

Chandrasekhar, S., 1960: Radiative transfer. Dover Publications Inc, New York

Natraj, V., Li, K.F., and *Yung, Y.L.*, 2009: Rayleigh scattering in planetary atmospheres: Corrected tables through accurate computation of *X* and *Y* functions. *The Astrophysical Jornal*, 691:1909-1920. https://doi.org/10.1088/0004-637X/691/2/1909

Natraj, V. and *Hovenier, J.W.*, 2012: Polarized light reflected and transmitted by thick Rayleigh scattering atmospheres. *The Astrophysical Journal*, 748:28 (16pp). https://doi.org/10.1088/0004-637X/748/1/28

Chandrasekar, S. and *Elbert, D.D.*, 1954: The illumination polarization of the sunlit sky on Rayleigh scattering. *Transactions of the American Philosophical Society, New Series 44*(6) 643-728.

Coulson, K.L., 1988: Polarization and intensity of light in the atmosphere. A. Deepak Publishing, Hampton, VA.

Coulson, K.L., Dave, J.V., and *Sekera, Z.*, 1960: Tables Related to Radiation Emerging from a Planetary Atmosphere with Rayleigh Scattering. Univ. California Press, Berkeley, CA

Yan, L., Yang, B., Zhang, F., Xiang, Y., and *Chen, W.*, 2020: Polarization Remote Sensing Physics. Peking University Press. Springer. https://doi.org/10.1007/978-981-15-2886-6

Yan, L., Wu, T., and *Wang, X.*, 2019: Polarization Remore Sesing for Land Observation. In Understanding of Atmospheric Systems with Efficient Numerical Methods for Observation and Prediction. IntechOpen. https://doi.org/10.5772/intechopen.79937

Mishchenko, M.I., 1987: Electromagnetic Scattering in Random Dispersive Media: Fundamental Theory and Applications (PhD thesis). National Academy of Sciences of Ukraine (published 2012). (in Russian)

Mishchenko, M.I., Travis, L.D., and *Lacis, A.A.*, 2006: Multiple scattering of light by particles: Radiativ transfer and coherent backscattering. Cambrige University Press

Sobirov, M.M. and Rozikov, J.Y., 2020: Nekotoriye voprosi teorii perenosa polyarizovannogo izlucheniya v izotropnoy srede s konechnoy opticheskoy tolshinoy. *Nauchno - texnicheskiy jurnal, Ferganskiy PI 24* (4), 15-24. (in Russian)

Lenoble, J., 1970: Importance de la polarization dans le rayonnement diffuse par une atmosphere planetair. *Journal of Quantativ Spektroskopy and Radiativ Transfer 10*, 533–551. (in French)

Ivchenko, Y.L., Pikus, G.Y., and *Yuldashev, N.X.*, 1980: Perenos polyarizovannogo izlucheniya v kristallax v eksitonnoy oblasti spektra. Vliyaniye pereizlucheniya. *Jurnal eksperimentalnoy i teoreticheskoy fiziki 79*, 1573-1590. (in Russian)

Ivchenko, Y.L., Pikus, G.Y., and *Yuldashev, N.X.*, 1981: Perenos polyarizovannogo izlucheniya v kristallax v eksitonnoy oblasti spektra. Poyaritonniye effekti. *Jurnal eksperimentalnoy i teoreticheskoy fiziki 80*, 1228-1246. (in Russian)

Sobirov, M.M. and *Yuldashev, N.X.*, 1984: Teoriya perenosa polyarizovannogo izlucheniya v kubicheskix kristallax v prodolnom magnitnom pole v oblasti eksitonnogo rezonansa. *Jurnal eksperimentalnoy i teoreticheskoy fiziki 87*, 677-690. (in Russian)

Pikus, G.Y., Sobirov, M.M., and *Yuldashev, N.X.*, 1985: Kinetika polyarizovannogo izlucheniya pri rezonansnom impulsnom vozbujdenii eksitonov v kristallax. *Jurnal eksperimentalnoy i teoreticheskoy fiziki 97*, 635-641.

Elterman, L., 1968: UV, visibe, and IR attenuation for altitudes to 50 km. *AFCRL-68-0153, Env. Res. Pap. No. 285*. U.S. Air Force.

Sobirov, M.M., Rozikov, J.Y., and *Ruziboyev, V.U.*, 2021: Polyarizatsionniye xarakteristiki diffuzno otrajennogo i propushyennogo izlucheniya v srede s konechnoy opticheskoy tolshinoy. Uzbekskiy fizicheskiy jurnal 23(2) 11-20. https://doi.org/10.35134/jitekin.v11i1.26

Sobirov, M. M., Rozikov, J. Y., Yusupova, D. A., and *Ruziboyev, V. U.*, 2023: Calculation of spectral and angular distribution of diffusely reflected, diffusely transmitted, and unscattered fluxes of solar radiation in atmospheric layers. *Applied Solar Energy 59(5)*, 761–769. https://doi.org/10.3103/S0003701X23601187

Sobirov M. M., Rozikov J. Y., Ruziboyeva, V. U., and *Kamolova, M.M.*, 2024: Calculation of the Spectral and Angular Distribution of Diffusely Reflected and Transmitted Solar Radiation Fluxes from Atmospheric Layers. Problems in the Textile and Light Industry in the Context of Integration of Science and Industry and Ways to Solve Them AIP Conf. Proc. 3045, pp.020008-1–020008-5. https://doi.org/10.1063/5.0197368

Kattawar, G.W., Plass, G.N., and *Hitzfelder, S.J.*,1976: Multiple scattered radiation emerging from Rayiegih and continental haze layers. Radiance, polarization, and neutral points. *Applied Optics 15(3)*, 632-647. https://doi.org/10.1364/AO.15.000632

Ivchenko, Y.L. and *Sobirov, M.M.*, 1985: Osobennost v spektre dvuxfononnogo Mandelshtamm - Brillyuenovskogo rasseyaniya nazad. *Fizika tvyordogo tela 27*, 1096-1104. (in Russian)

Dave, J.V. and *Furukawa, P. M.*, 1966: Intensity and polarization of the radiation emerging from an optically thick atmosphere. *Journal of the Optical Society of America 56*, 394-400. https://doi.org/10.1364/JOSA.56.000394

Horvath, G., Bernath, B., Suhai, B., Barta, A., and *Wehner, R.*, 2002: First observation of the fourth neutral polarization point in the atmosphere. *Journal of the Optical Society of America 19(10)*, 2085–2099. https://doi.org/10.1364/JOSAA.19.002085

Horvath, G., Bernath, B., Suhai, B., Barta, A., and *Wehner, R.*, 2011: Neutral points in an atmosphere–ocean system. 2: Downwelling light field. *Applied Optics 50(3)*, 335–346. https://doi.org/10.1364/AO.50.000335

DOI:10.28974/idojaras.2026.2.5

IDŐJÁRÁS

Quarterly Journal of the HungaroMet Hungarian Meteorological Service
Vol. 130, No. 2, April – June, 2026, pp. 169–223

Advancing drought forecasting in Spain: Integration of meteorological indices and Random Forest algorythm for future projections

Gözde Nur Akşan* and **Fatih Dikbaş**

Pamukkale University,Faculty of Civil Engineering
Kınıklı, Kınıklı Campus, University St. 11, 20160 Pamukkale, Denizli, Turkey

**Corresponding author E-mail: gozdeaksann@gmail.com*

(Manuscript received in final form on January 31, 2025)

Abstract— Drought is a serious environmental issue that negatively impacts water resources, agricultural production, ecosystems, and economic activities as a result of prolonged periods of low precipitation. In particular, the depletion of water resources and difficulties in accessing water pose significant threats to societies. In this context, developing effective forecasting systems in regions at risk of drought is critical for managing water resources more efficiently and taking timely measures. This study examines the potential of integrating various drought indices and machine learning techniques to improve the accuracy of meteorological drought predictions. Using data from 54 meteorological stations in Spain for the 1973–2023 period, drought analyses were conducted based on the standardized precipitation index (SPI), standardized precipitation evapotranspiration index (SPEI), and reconnaissance drought index (RDI). Future drought predictions were made using the Random Forest (RF) algorithm. The RF algorithm successfully analyzed historical climate data to understand the temporal and spatial dynamics of drought occurrences. Additionally, a newly developed drought mapping approach demonstrated that short-term droughts are more prevalent in northern Spain compared to the southern regions. The findings highlight the likelihood of increased drought severity in specific areas and its potential impacts on agricultural production and water management. This study serves as a crucial guide for policymakers aiming to develop drought management strategies and contributes to effective planning to mitigate future drought impacts. Furthermore, the developed software is provided as open source alongside the article.

Key-words: Spain, standardized precipitation index (SPI), standardized precipitation evapotranspiration index (SPEI), reconnaissance drought index (RDI), Random Forest algotythm, future drought prediction, climate change

1. Introduction

Climate change and drought analysis are of great importance for environmental and economic sustainability. Rising temperatures and changing precipitation patterns threaten agricultural production, drinking water resources, and the balance of ecosystems. Therefore, developing drought management strategies and preventive measures against these risks is critical for the efficient use of water resources and the success of climate adaptation policies.

Climate change significantly impacts water resources worldwide. Sustainable management of water resources is particularly vital for predicting and mitigating the effects of climatic risks such as droughts, extreme precipitation, and temperature increases. Studies on water resource management and drought prediction are indispensable for both short-term operational decisions and long-term strategic planning (*Wang et al.*, 2019; *Zhang et al.*, 2019; *Alivi et al.*, 2021).

Drought is one of the most significant and destructive consequences of climate change. Prolonged droughts can lead to declines in agricultural production, reductions in water reserves, losses in hydroelectric energy production, and challenges in meeting water demand. This situation necessitates continuous monitoring of water resources, along with conducting drought analyses and forecasts, to ensure sustainable management of water and make effective decisions.

Drought is a complex and multidimensional environmental issue characterized by prolonged water scarcity, threatening the sustainable use of natural resources. Often associated with low precipitation levels and high evaporation rates, drought can manifest differently depending on climatic conditions. Meteorological drought is defined as a prolonged period during which a region receives precipitation significantly below its normal levels. Agricultural drought occurs when insufficient soil moisture adversely impacts agricultural production, while hydrological drought arises from the depletion of surface and groundwater resources (*Wilhite* and *Glantz*, 1985; *Mishra* and *Singh*, 2010). Given the increasing severity of drought events, continuous monitoring, analysis, and forecasting are essential to developing effective strategies for water resource management.

Spain is one of the European countries most affected by drought due to its semi-arid and arid regions. In recent years, rising temperatures and changes in rainfall patterns have placed significant pressure on water resources, leading to more frequent and severe droughts. These changes have resulted in water shortages, agricultural yield losses, and reductions in hydroelectric energy production, particularly in the southern and eastern regions of the country (*Vicente-Serrano et al.*, 2014; *Lorenzo-Lacruz et al.*, 2013). Increased water demand further necessitates a reassessment of current water management policies to ensure sustainability.

Drought indices play a significant role in climate change studies. In this study, statistical and machine learning-based methods were employed to detect

and predict long-term drought variations in Spain. For drought analysis, commonly used indices such as the standardized precipitation index (SPI), standardized precipitation evapotranspiration index (SPEI), and reconnaissance drought index (RDI) were evaluated. These indices serve as effective tools for identifying drought and its severity by utilizing water balance components such as precipitation, temperature, and evapotranspiration (*Sierra-Soler et al.*, 2016; *Zarch et al.*, 2015; *Zuo et al.*, 2018).

Long-term precipitation and temperature datasets from the meteorological stations included in the study were utilized to calculate drought indices. These indices are used to identify imbalances in the water budget and assess drought severity, considering climatic variables. Calculated over various time scales (1, 3, 6, 9, and 12 months), they provide insights into the intensity and duration of drought.

While SPI and SPEI analyze drought processes associated with precipitation and evapotranspiration, RDI better represents agricultural drought by also accounting for water demand. The use of these indices supports strategic decision-making in both agriculture and water resource management. Future drought values in Spain were predicted using the Random Forest algorithm, one of the Supervised Learning methods in machine learning. By forecasting future drought conditions in Spain, this study aims to support data-driven decision-making processes in water management and agriculture, ensuring the sustainability of vital resources amid the growing challenges of climate change.

2. Materials and methods

2.1. Study area

Spain, located in southwestern Europe, is a country distinguished by its diverse geographical and environmental features. It spans from 36°00’ to 43°47’ north latitude and 3°19’ west to 7°20’ east longitude. To the northeast, it shares borders with France and Andorra, to the west with Portugal, while it is surrounded by the Mediterranean Sea to the south and east, and the Atlantic Ocean to the northwest (*Fig. 1*).

The country is known for its varied landscapes, including vast mountain ranges such as the Pyrenees and Sierra Nevada, as well as large plateaus like the Meseta Central. With over 4,000 kilometers of coastline, Spain is also a significant maritime country. Its geographical diversity encompasses a range of climates, from the hot, dry summers and mild, rainy winters characteristic of the Mediterranean climate to the more temperate and oceanic climate of the north. Average temperatures vary from 10 °C in the northern regions to 25 °C in the south. Similarly, annual precipitation varies significantly; in the arid southeast, rainfall may be as low as 300 mm, while in the mountainous north, it can exceed 1,500 mm.

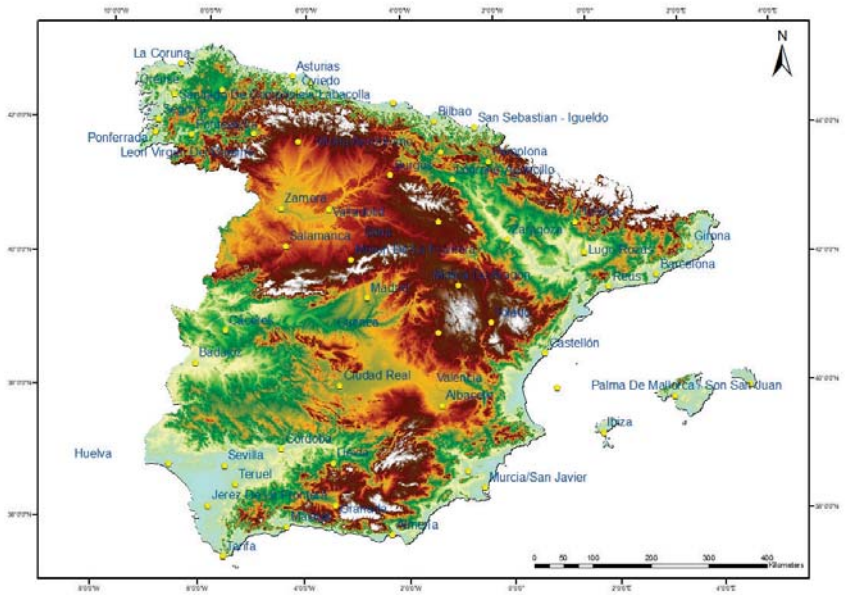

Fig. 1. A topographic map showing the locations of the meteorological stations examined in Spain. The authors used the administrative shapefile downloaded from the European Commission - Copernicus EU-DEM to create the map of Spain.

Spain's unique climate and topography have significant impacts on agriculture, the economy, and natural resource management. While some regions face challenges such as drought, others experience occasional flooding. This variability makes Spain a focal point for research on climate change, agriculture, water resource management, and disaster preparedness. These issues underscore the need for innovative solutions to protect livelihoods and promote sustainable development across the country.

Spain has faced increasing challenges related to drought due to climate change and the overexploitation of water resources. Recent studies highlight the intensifying drought conditions in Spain in terms of frequency and severity due to climate change-induced rising temperatures and reduced rainfall, which have significant implications for agriculture, water management, and public health. More than 60% of Spain's agricultural land has been affected by water shortages, with over 3.5 million hectares experiencing significant damage. Irrigated crops are particularly vulnerable. Urban water demand remains a high priority, with restrictions being implemented only during extreme *emergencies (García Galiano* and *Broekman*, 2023). *Jiménez-Donaire et al.* (2020) emphasize that future climatic changes will likely increase the frequency, duration, and intensity of agricultural droughts, necessitating the adoption of novel drought indices for better assessment. *Paneque* (2015) discusses the evolution of Spain's drought

management strategies, advocating a shift from traditional infrastructure-based approaches to more sustainable, risk-based models. *Salvador et al.* (2020) quantify the impact of droughts on daily mortality rates in Spain, using indices like SPI and SPEI to reveal significant correlations. *García Galiano* and *Broekman* (2023) explore the dual impacts of rising temperatures and overexploitation of water resources, contributing to prolonged drought conditions. Additionally, the European Commission's Joint Research Centre (2024) underscores the critical impact of prolonged drought and record temperatures on the Mediterranean region, including Spain, affecting water availability, agriculture, and ecosystems. Projections indicate reduced precipitation and higher temperatures, leading to longer and more severe drought periods, and the findings collectively underline the urgent need for integrated and adaptive management strategies to mitigate the multifaceted impacts of drought in Spain.

2.2. Datasets

Climate records for 54 stations in Spain from 1973 to 2023 were collected from the European Climate Assessment and Dataset (ECAandD) and Wetter und Klima – Deutscher Wetterdienst – Startseite sources. The climatic variables obtained include daily precipitation (mm) and daily average temperature (°C). Using these data, potential evapotranspiration (PET) values were determined using the Thornthwaite method (*Thornthwaite,* 1948).

Table 1. The numbers of training and testing data

	SPAIN		
	SPI, SPEI, and RDI data		
	Training data (80%)	**Testing data (20%)**	**Total data**
1-month	491	120	611
3-month	489	120	609
6-month	487	119	606
9-month	484	119	603
12-month	482	118	600

The calculated drought indices were divided such that 80% of the data was used for training the machine learning model, and 20% was used for testing (see *Table 1*).

2.3. Standardized precipitation index (SPI)

The standardized precipitation index (SPI) is a commonly used index in drought analysis that expresses precipitation anomalies in terms of standard deviations. Developed by *McKee et al.* in 1993, SPI allows for determining the severity and

duration of drought based solely on precipitation data. The SPI can be calculated for time scales ranging from one month to several years, capturing both short-term droughts (affecting agriculture) and long-term ones (affecting water resources and ecosystems) and therefore it is used in short, medium and long-term drought analysis.

2.3.1. SPI calculation steps

1. Data collection: A minimum of 30 years of precipitation data is required for SPI calculation. This data is used to determine the mean and standard deviation for each time period.
2. Normalization of precipitation: The precipitation data for a region is normalized by comparing it to the long-term average. SPI performs this normalization using the Gaussian distribution and calculates the degree of deviation from the long-term mean of precipitation (*Thom,* 1966; *McKee et al.,* 1993).
3. Interpretation of SPI Values: Positive SPI values indicate wet conditions, while negative values indicate dry conditions (*Sırdaş* and *Şen,* 2003). SPI values can be classified as follows (*Table 2*):

Table 2. Standardized precipitation index (SPI) values and classification (*Jain et al.,* 2015; *Adnan et al.,* 2018)

Classification	**SPI value range**
Extremely dry	$SPI \leq -2.0$
Very dry	$-2.0 < SPI \leq -1.5$
Moderately dry	$-1.5 < SPI \leq -1.0$
Near normal	$-1.0 < SPI < 1.0$
Moderately wet	$1.0 \leq SPI < 1.5$
Very wet	$1.5 \leq SPI < 2.0$
Extremely wet	$SPI \geq 2.0$

2.3.2. Features and advantages of SPI

The standardized precipitation index (SPI), with its flexible and simple structure, is a widely used index for meteorological drought detection and analysis. Its ability to be applied over different time scales makes SPI an ideal tool for agriculture, water management, and hydrological analysis. For instance, monthly SPI values can be used for short-term drought detection, while a 12-month SPI is more suitable for long-term assessments. Since SPI relies solely on precipitation data, it simplifies the calculation process and eliminates the need for large and complex datasets. Additionally, its normalized structure allows for spatial comparisons between different climatic regions and seasons. These characteristics

make SPI suitable for a wide range of applications, from detecting sudden precipitation deficits to evaluating agricultural and hydrological droughts.

SPI offers diversity by being calculable over different time scales. The 1-month SPI represents short-term precipitation anomalies and provides information on sudden impacts such as crop loss. The 6-month SPI analyzes seasonal and medium-term precipitation trends, offering a more sensitive assessment compared to the Palmer drought severity index (PDSI). For long-term analysis, the 12-month SPI is associated with long-term hydrological processes such as reservoir levels, river flows, and groundwater levels. These variations of SPI provide flexible solutions tailored to different needs based on the time scale, offering high adaptability in drought analysis.

In this context, the convenience offered by SPI, its wide range of applications, and the ability to perform multi-scale analysis contribute to a better understanding of meteorological and hydrological drought processes. Especially with the increasing impacts of climate change, the use of SPI has become even more critical in environmental and economic decision-making processes.

2.4. Standardized precipitation evapotranspiration index (SPEI)

The standardized precipitation evapotranspiration index (SPEI) is a widely used index for drought detection that takes into account not only precipitation but also other climatic variables such as temperature. While SPEI is based on the fundamental principles of SPI, it provides a more climate-sensitive indicator by considering the effects of factors such as temperature increases and evaporation (evapotranspiration), recognizing that drought is influenced not only by a lack of precipitation but also by these additional factors (*Beguería et al.*, 2014; *Telesca et al.*, 2012; *Vicente-Serrano et al.*, 2010, 2011, 2012, 2014, 2020).

2.4.1. SPEI calculation steps

1. Data collection: The calculation of SPEI requires both precipitation and potential evapotranspiration (PET) data. PET is determined based on temperature and other meteorological factors. For PET calculation, the Thornthwaite (*Thornthwaite,* 1948) or Penman-Monteith (*Allen et al.,* 1998) methods are commonly used.
2. Water budget calculation: SPEI determines the water budget by calculating the difference between precipitation and PET for each time period (e.g., 1, 3, 6, 12 months). When this difference is positive, it indicates a water surplus, while a negative difference indicates a water deficit, representing drought conditions.

$$D_n^k = \sum_{i=0}^{k-1} (P_{n-i} - PET_{n-i}) \quad (1)$$

3. Probability distribution and standardization: The water budget differences are standardized to fit a normal probability distribution, which results in the calculation of the SPEI value. This standardization allows for the comparison of drought events across different time periods and spatial locations.

$$SPEI = W - \frac{C_0 + C_1 W + C_2 W^2}{1 + d_1 W + d_2 W^2 + d_3 W^3}, \quad (2)$$

where C_0 = 2.515517, C_1 = 0.802853, C_2 = 0.010328, d_1 = 1.432788, d_2 = 0.189269, d_3 = 0.001308 are constants.

If $P \leq 0.5$ then $W = \sqrt{-2In[P]}$

If $P > 0.5$ then $W = \sqrt{-2In[1-P]}$

P is the probability of exceeding a specific *D* value (*Wang et al.*, 2021).

4. Interpretation of SPEI values: Similar to SPI, the SPEI can have positive or negative values, and based on these values, drought or excessive rainfall conditions are classified in the same manner as shown in *Table 2*.

2.*4.2. Features and advantages of SPEI*

The standardized precipitation evapotranspiration index (SPEI) is a powerful tool for assessing the impact of climate change on drought by considering temperature increases. By incorporating factors such as precipitation, temperature, and evapotranspiration, SPEI becomes more sensitive to climate change. This comprehensive approach not only allows for a more accurate detection of drought severity but also provides a significant advantage for climate change studies. Like the SPI, the SPEI can be calculated over both short (e.g., 1 month) and long (e.g., 12 months or more) time scales, offering flexible applications for both meteorological and agricultural drought analyses.

The SPEI has a wide range of applications in meteorological, agricultural, and hydrological drought analyses. By considering not only precipitation deficits but also the effects of temperature and evaporation, it allows for a more accurate assessment of the impacts of drought on agricultural production and water

resources. This feature makes the SPEI an ideal indicator, especially for climate change studies. Over the long term, the effect of temperature increases on drought severity can be effectively analyzed using the SPEI.

The different time scales of the SPEI provide an opportunity for detailed assessment according to specific needs. The one-month SPEI is ideal for detecting short-term precipitation and evaporation imbalances, highlighting immediate drought conditions. The six-month SPEI focuses on seasonal and medium-term water balance analyses, playing a crucial role in agricultural and irrigation planning. The twelve-month SPEI, on the other hand, analyzes long-term trends in precipitation and evapotranspiration, relating to long-term hydrological processes such as reservoir levels, river flows, and groundwater.

Overall, the versatile nature of the SPEI and its sensitivity to climate change make it a unique tool for drought analysis and resource management. By addressing the effects of temperature increases and changes in water balance, it provides valuable contributions to both scientific research and policy development processes.

2.5. Reconnaissance drought index (RDI)

The reconnaissance drought index (RDI) is an index used in drought analysis, based on the relationship between precipitation (P) and potential evapotranspiration (PET), which better represents situations where variables like temperature affect drought. RDI was developed to identify conditions like agricultural and hydrological drought, where water demand exceeds supply, and is one of the indices analyzing the water balance (precipitation – evapotranspiration difference) (*Tsakiris* and *Vangelis*, 2004, 2005*; Tsakiris et al.*, 2007). There are three different expressions of RDI: the RDI starting value (α_k), the Normalized RDI (RDI_n), and the Standardized RDI (RDI_{st}) (*Zarei et al.*, 2016).

2.5.1. RDI calculation steps

1. Data collection: To calculate the RDI, precipitation (P) and potential evapotranspiration (PET) data are required. PET data is typically calculated using meteorological variables such as temperature, wind speed, humidity, and solar radiation. These data can be obtained using models like Thornthwaite or Penman-Monteith.
2. Climatic water budget: The RDI calculates the water budget by dividing the total precipitation (P) by the total potential evapotranspiration (PET) for a specific time period. The basic formula is as follows:

$$\alpha_k^{(i)} = \frac{\sum_{j=1}^{j=k} P_{ij}}{\sum_{j=1}^{j=k} PET_{ij}}, \text{i} = 1 \text{ to N} \quad (3)$$

The RDI initial value (α_k) is calculated in a time basis of k (months) as the following equation. where P_{ij} and PET_{ij} the precipitation and potential evapotranspiration of the *j*th month of the hydrological year and the precipitation and potential evapotranspiration of the *i*th year and *N* is total number of years. The hydrological year for the Mediterranean region starts in October, hence for October *k*=1. Here, RDI_n represents the RDI value for a specific time period. This formula measures the capacity of precipitation to meet evapotranspiration.

$$RDI_n^{(i)} = \frac{\alpha_k^{(i)}}{\alpha_k} - 1 \quad (4)$$

3. Gamma distribution and standardization: RDI values are standardized according to the Gamma distribution to analyze the anomalies in the water budget for a specific region and period (*Tigkas et al.,* 2013). This standardization process results in the calculation of the Standardized RDI (RDI_{st}). RDI_{st} allows for the comparison of drought events across different geographic regions and time periods (*Tsakiris* and *Vangelis*, 2005).
4.

$$RDI_{st}^{(i)} = \frac{y_k^{(i)} - \bar{y}_k}{\sigma_{yk}} = In\left(\alpha_k^{(i)}\right) \quad (5)$$

where y_k is the $In(\alpha_k)$, $\bar{y}_k$ is the arithmetic mean of y_k and σ_{yk} is its standard deviation.

5. Interpretation of RDI values: Like SPI and SPEI, RDI_{st} also has positive and negative values and uses the same classification (*Table 2*).

2.5.2. Features and advantages of RDI

The reconnaissance drought index (RDI) reflects drought severity in a more realistic manner by considering not only precipitation data but also meteorological variables such as temperature and evapotranspiration. Its ability to account for the increase in evapotranspiration caused by rising temperatures makes RDI a suitable tool for analyzing the impacts of climate change. Like SPI and SPEI, RDI can be used for both short-term (e.g., 1 month) and long-term (e.g., 12 months or longer) drought analyses. This flexibility provides a wide range of applications in meteorological and agricultural drought assessments. Furthermore, RDI's combined evaluation of water supply (precipitation) and water demand (evapotranspiration) offers a unique advantage, particularly in the context of agricultural and water resources management.

The RDI plays a critical role in agricultural and hydrological drought analyses. In terms of agricultural drought, it directly measures the water demand

of plants, allowing for a detailed assessment of the impact of drought on agricultural production. In the context of hydrological drought, it serves as an important decision support tool in managing reservoirs, lakes, and groundwater resources. Additionally, in climate change studies, RDI stands out as an effective indicator for analyzing the long-term effects of rising temperatures and changing water budgets.

The different time scales of the RDI allow for a more detailed and scaled analysis of drought processes. A one-month RDI is used to assess short-term water imbalances, particularly effective in monitoring sudden impacts such as agricultural water stress. A six-month RDI reveals seasonal water imbalances, supporting critical decisions in agriculture and natural resource management. A twelve-month RDI analyzes long-term changes in the water balance, providing a foundation for strategic planning regarding reservoir levels, groundwater, and river flows.

Overall, the multidimensional structure of the RDI and its comprehensive approach, which incorporates climate variables, make it a valuable tool for the sustainable management of water resources and the mitigation of agricultural drought impacts. The flexibility it provides in both short-term and long-term applications makes the RDI a key component in drought analysis and management.

2.6. Machine learning

Machine learning is a field of technology capable of analyzing large amounts of data, discovering patterns, and predicting future events. In drought analysis and prediction, machine learning plays a crucial role, especially in the sustainable management of water resources. The machine learning models used in this field aim to predict future drought conditions by analyzing past trends in climate data. These predictions help develop strategies to reduce drought risk and manage water resources more effectively. In this study, the Random Forest algorithm has been chosen to make future drought predictions. The reason for this choice is its ability to handle complex and multivariable data. Primarily, it offers strong performance in regression problems, allowing for accurate predictions of drought intensity and duration based on drought indices. Additionally, this model stands out for its ability to identify important features in high-dimensional datasets, which helps select the most effective meteorological and environmental factors for analysis, thus improving the model's accuracy. Furthermore, since Random Forest can detect anomalies, it is effective in identifying extreme drought events and unusual climate conditions. With these capabilities, it emerges as a reliable and flexible method for drought analysis and prediction.

Random Forest is a powerful and flexible machine learning method used for both classification and regression problems within supervised learning algorithms. This algorithm is an ensemble model made up of multiple decision trees (*Breiman*,

2001). Random Forest aims to make more accurate and balanced predictions by reducing the weaknesses of individual decision trees. The term "random" refers to the model's process of making random selections between both data subsets and features, which helps reduce the risk of overfitting (*Pedregosa et al.*, 2011).

2.6.1. The basic features of the Random Forest algorithm

- Ensemble structure: Random Forest combines multiple independent decision trees. Each tree is trained on a randomly selected subset of data and a random subset of features. As a result, the trees make different predictions, which enhances the overall performance of the model.
- Bagging (bootstrap aggregating): Bagging is a technique where the model is trained on different subsets of data. In Random Forest, each decision tree is trained using random samples drawn from the original dataset. This method reduces the model's variance and helps achieve more generalized results.
- Random feature selection: When building each decision tree, a random subset of features is considered at each node, rather than using all features. This increases the diversity of the model, reduces the dependence between the trees, and enhances the overall performance.

2.6.2. Working steps of Random Forest algorithm

1. Creating trees with subsets of the dataset: Random Forest creates multiple decision trees using randomly selected subsets of the original dataset through the bootstrap method.
2. Training the trees: Each tree is trained independently based on these subsets. At each node of the tree, a random subset of features is selected, and the best feature for splitting is chosen.
3. Combining predictions: The model combines the outputs of each decision tree. In classification problems, the majority vote of the trees is considered. In regression problems, the average of the predictions made by all trees is taken.
4. Determining the final result: The model produces the final result by majority vote (for classification) or by averaging the predictions (for regression).

2.6.3. Advantages of Random Forest

- Prevention of overfitting: Decision trees are prone to overfitting, but Random Forest mitigates this issue. When multiple different trees are created, the model’s overall tendency prevents it from becoming overly sensitive to noise in the dataset.
- Low variance: Trees trained on different subsets of data through bagging reduce variance, which enhances the model’s ability to generalize.
- Feature importance ranking: Random Forest can measure the importance of each feature in the model. This is particularly useful for identifying key features as well as irrelevant ones in the dataset.

- Success with imbalanced datasets: Random Forest can yield effective results when working with imbalanced datasets. Some trees may give more weight to the rarer classes, improving performance on these classes.
- Parallel processing capability: Since the trees are trained independently, Random Forest can be run in parallel, which provides a time advantage when working with large datasets.

2.6.4. Disadvantages of Random Forest

- Slower predictions: Since Random Forest uses a large number of decision trees, the prediction time may be longer compared to individual decision trees.
- Memory usage: The creation of multiple trees requires more memory, which can be demanding, especially with large datasets.
- Interpretability: While a single decision tree is relatively simple and interpretable, the hundreds or even thousands of trees in a Random Forest model make it less interpretable.

2.6.5. Application areas of Random Forest

- Classification problems: It is commonly used in classification problems such as medical diagnosis, customer segmentation, and credit risk assessment.
- Regression problems: Random Forest is also highly successful in regression problems where predictions need to be made, such as in climate change studies, housing price forecasting, and agricultural productivity.
- Feature selection: Random Forest can be used to identify important features in high-dimensional datasets.
- Anomaly detection: It is an effective method for detecting anomalous data points.

2.6.6. Parameters of Random Forest

n_estimators: It specifies the number of decision trees to be used in the model.
Recommended value range:

- 5–30 (for small datasets).
- 10–100 (for large and complex datasets).

max_depth: It limits the maximum depth of each decision tree.
Suggested value range:

- 5–30 (for small datasets).
- 10–100 (for large and complex datasets).

random_state: It is a fixed seed value used in random number generation.
Recommended value range:

- It can be any fixed number.

In the modeling process with the Random Forest algorithm, the steps in the flowchart in *Fig. 2* have been followed.

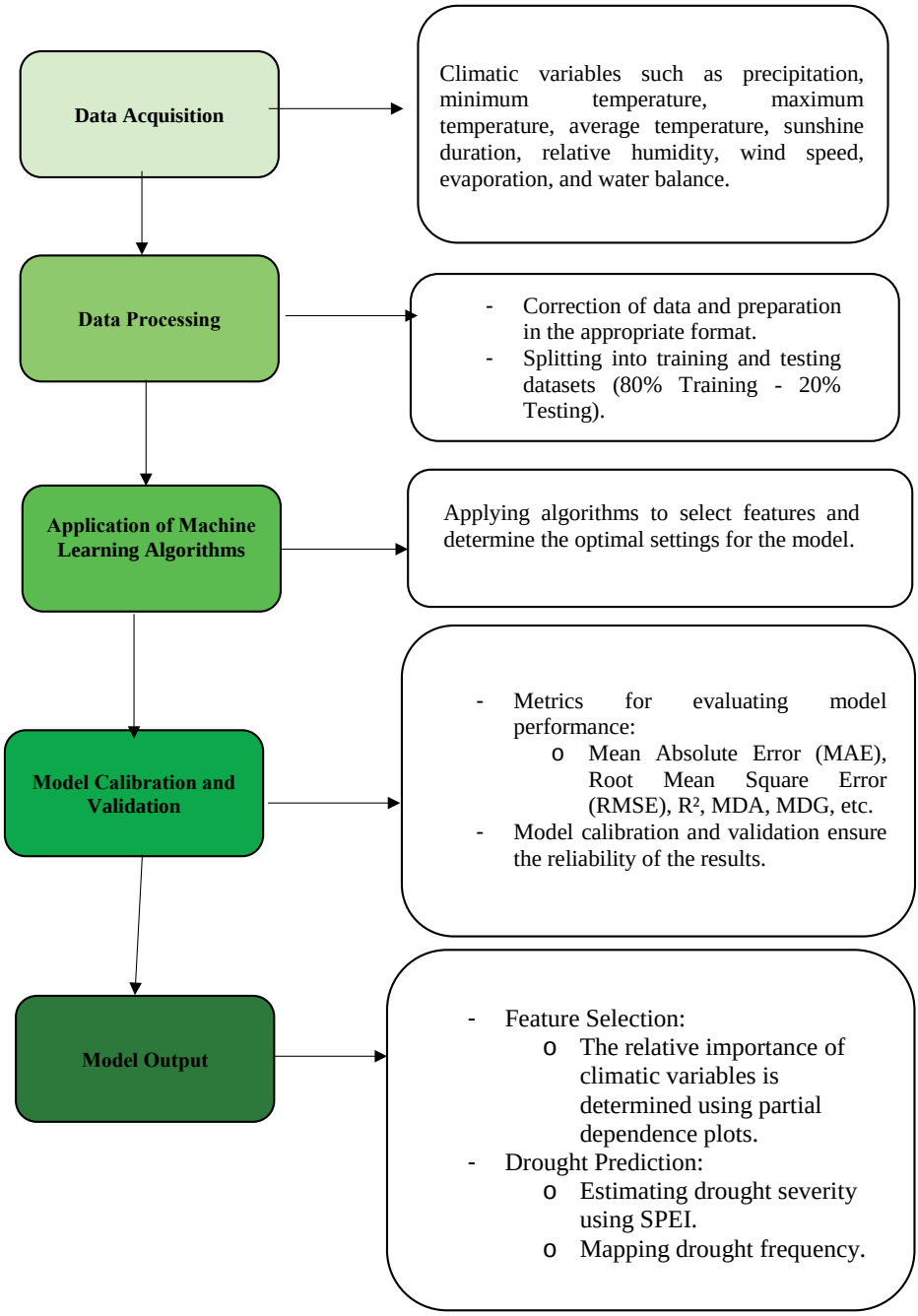

Fig. 2. Flowchart of the Random Forest algorithm implementation.

In this study, the Random Forest algorithm was applied using a Python-based code developed to model time series data and make future drought predictions (see *Appendix 1*). The model was designed to work with drought indices such as SPI (standardized precipitation index), SPEI (standardized precipitation evapotranspiration index), and RDI (reconnaissance drought index). In the first step, the datasets for these indices were scaled, and input (features) and target variables were created using 12 months of historical data. The dataset was split into 80% training and 20% testing subsets.

The regression variant of the Random Forest algorithm, the RandomForestRegressor, was configured as an ensemble model consisting of 10 decision trees (n_estimators=10). Each decision tree was trained on different subsets of the dataset and branched up to a maximum depth of 55 (max_depth=55) to enhance prediction performance. After the model training was completed, predictions were made on the test data and compared with the actual SPI, SPEI, and RDI values through inverse scaling. The predicted values were visualized along the time axis, generating graphs to understand drought trends in past and future periods.

The model generated monthly predictions covering a 50-year future period, presented as a continuous time series. In addition to the forecasts, the model's performance was evaluated using Root Mean Square Error (RMSE), Mean Absolute Error (MAE), and R^2 metrics. For instance, the RMSE value was low on the training data, and the R^2 score exceeded 0.85, indicating the model's strong accuracy and predictive capability.

The obtained results provide a comprehensive evaluation for validating past drought trends and generating future projections. All predictions and analysis outcomes were saved in an Excel file along with graphical representations, enabling researchers to examine the data more conveniently. This approach once again highlights the effectiveness of the Random Forest algorithm in handling multidimensional climatic variables.

2.7. Model evaluation metrics

Model validation is an important step in testing the accuracy and reliability of machine learning models. In this process, researchers have utilized various statistical metrics (*Nabavi-Pelesaraei et al.*, 2018; *Chen et al.*, 2021). To evaluate the performance and reliability of the applied models, we used RMSE, MAE, and R^2 metrics:

- Root mean square error (RMSE): The square root of the average of the squared errors of prediction. A low RMSE value indicates that the model has more accurate predictions.

$$RMSE = \sqrt{\frac{\sum_{i=1}^{N}\left(Y_{obs} - Y_{pred}\right)^2}{N}} \quad (6)$$

- Mean absolute error (MAE): The average of the absolute differences between the actual and predicted values. A low MAE indicates better model accuracy.

$$MAE = \frac{\sum_{i=1}^{N}\left|Y_{obs} - Y_{pred}\right|}{N} \quad (7)$$

- R^2 (coefficient of determination): Represents how much of the variance in the data is explained by the model. The closer R^2 is to 1, the higher the accuracy of the model.

$$R^2 = \frac{\sum_{i=1}^{N}(Y_{obs} - \overline{Y_{obs}})\left(Y_{pred} - \overline{Y_{pred}}\right)}{\sqrt{\sum_{i=1}^{N}(Y_{obs} - \overline{Y_{obs}})^2}\sqrt{\sum_{i=1}^{N}\left(Y_{pred} - \overline{Y_{pred}}\right)^2}} \quad (8)$$

In the above equations, Y_{obs} represents the actual dependent variable, Y_{pred} represents the predicted dependent variable, and N denotes the number of observations. As a general rule, models with lower RMSE and MAE values, and higher R^2 values, are considered more accurate and reliable for prediction during the testing phase.

3. Results and discussion

3.1. Frequency analysis of drought indices

The frequency analysis results of SPI, SPEI, and RDI values for the selected time scales at the Spanish stations have been calculated, and the relative frequency results are presented in *Tables 3 to 19* of *Appendix 2*. The results have been classified according to the dry and wet categories. For all frequencies, considering dryness, the range of values has varied from 0% to 32% for SPI, 16% to 33% for SPEI, and 6% to 26% for RDI.

Upon detailed examination, according to the SPI analysis results, the highest relative frequency in the moderate dryness category is 12%, observed at the Huesca station on the 12-month timescale. Meanwhile, the highest relative

frequency in the extreme dryness category is 8%, observed at the Barcelona and Sevilla stations, also on the 12-month timescale.

According to the SPEI results, the highest relative frequency in the moderate dryness category is 12%, observed at the Valladolid and Huesca stations on the 1-month and 3-month timescales, respectively. In the extreme dryness category, the highest relative frequency is 6%, observed at the Barcelona station on the 12-month timescale.

According to the RDI analysis results, the highest relative frequency in the moderate dryness category is 14%, observed at the Bilbao station on the 6-month timescale. In the extreme dryness category, the highest relative frequency is 6%, observed at different stations across all timescales.

3.2. The observed and future changes of meteorological drought events according to time series.

For each station examined in Spain, time series graphs containing observed data, training data, test data, and forecast values determined by the Random Forest method were generated for each 1, 3, 6, 9, and 12-month time period by the developed software (a total of 810 graphs for 54 stations). As an example, the SPI, SPEI, and RDI time series graphs for the 1-month calculation period at the Ibiza station are presented in *Fig. 3*. Upon examining the SPI, SPEI, and RDI outputs, it was observed that, as the time scale increased, the drought trend generally became more pronounced, the frequency of drought periods decreased, but there was a relative increase in the duration and severity of drought.

The wet and dry periods, which were relatively ambiguous at the one- and three-month time scales, began to become more distinct starting from the six-month time scale. When comparing the SPI, SPEI, and RDI values at the selected time scales, although the temporal development of both indices showed similarities, some small differences were observed in the characteristic features of drought periods (frequency, magnitude, and severity). The differences in the fluctuations and continuity characteristics of these indices representing drought features tend to decrease as the time scale increases.

a)

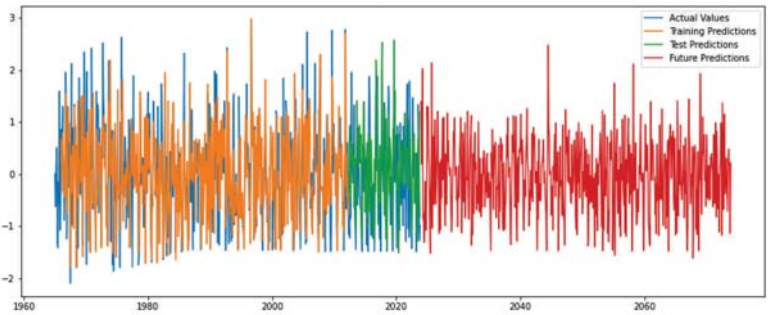

b)

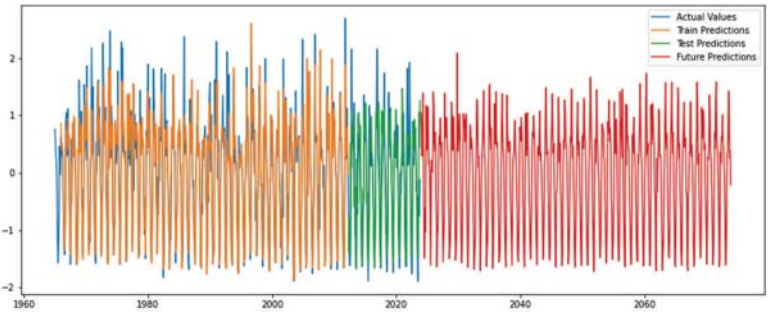

c)

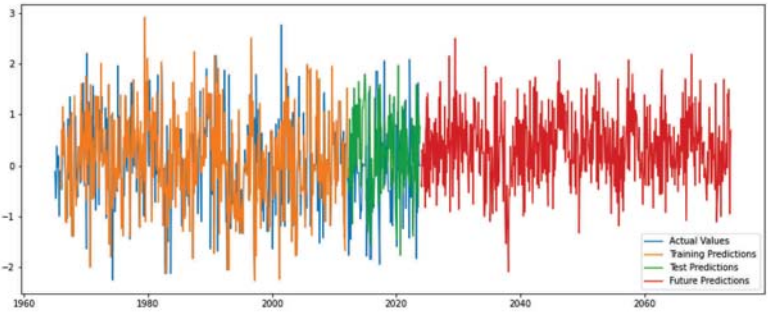

Fig. 3. Time series graphs for the Ibiza Station: a) 1-month SPI, b) 1-month SPEI, c) 1-month RDI.

3.3. The temporal and spatial pattern of drought intensity and frequency.

Using the selected model based on region-specific SPI, SPEI, and RDI, as well as the influential meteorological parameters, drought intensity was mapped for Spain from 1973 to 2023 based on observed data and from 2024 to 2073 based on predicted future data across different time scales (*Figs. 7, 8*, and *9*).

By summing the dryness values (SPI <= -1) experienced in the region and dividing by the total time, the SPI-based temporal drought values proposed in this study were determined. According to the SPI-based temporal drought values, spatially, it was found that short-term drought intensity occurred in the northern part of the country, while longer-term drought occurred in the central, eastern, and southern regions. For longer periods, the calculations indicated that drought shifted to the central and southern areas of Spain, and in future predictions, drought risks were observed to emerge particularly in the western regions. In the periodic evaluation, it was determined that the intensity of drought predicted to occur in the future would increase (*Fig 4*).

When looking at the SPEI-based temporal drought values, it has been determined that short-term drought observed spatially is more prominent in the central and southern parts of the country, while longer-term drought is more pronounced in the western and northern regions. Future predictions indicate that the intensity of drought is shifting from the southern part of the country towards the eastern and western regions. In the periodical assessment, the SPEI-based temporal drought value is expected to peak at -1.43 during the 12-month period (*Fig 5*).

Looking at the RDI-based temporal drought values, it has also been determined that short-term drought events are particularly impactful in the northern regions of the country, while longer-term drought, as seen in the maps, is more intense in the eastern and western regions, affecting the entire country. In the periodical assessment, it has been concluded that the intensity of future droughts is expected to increase compared to the observed drought intensity (*Fig 6*).

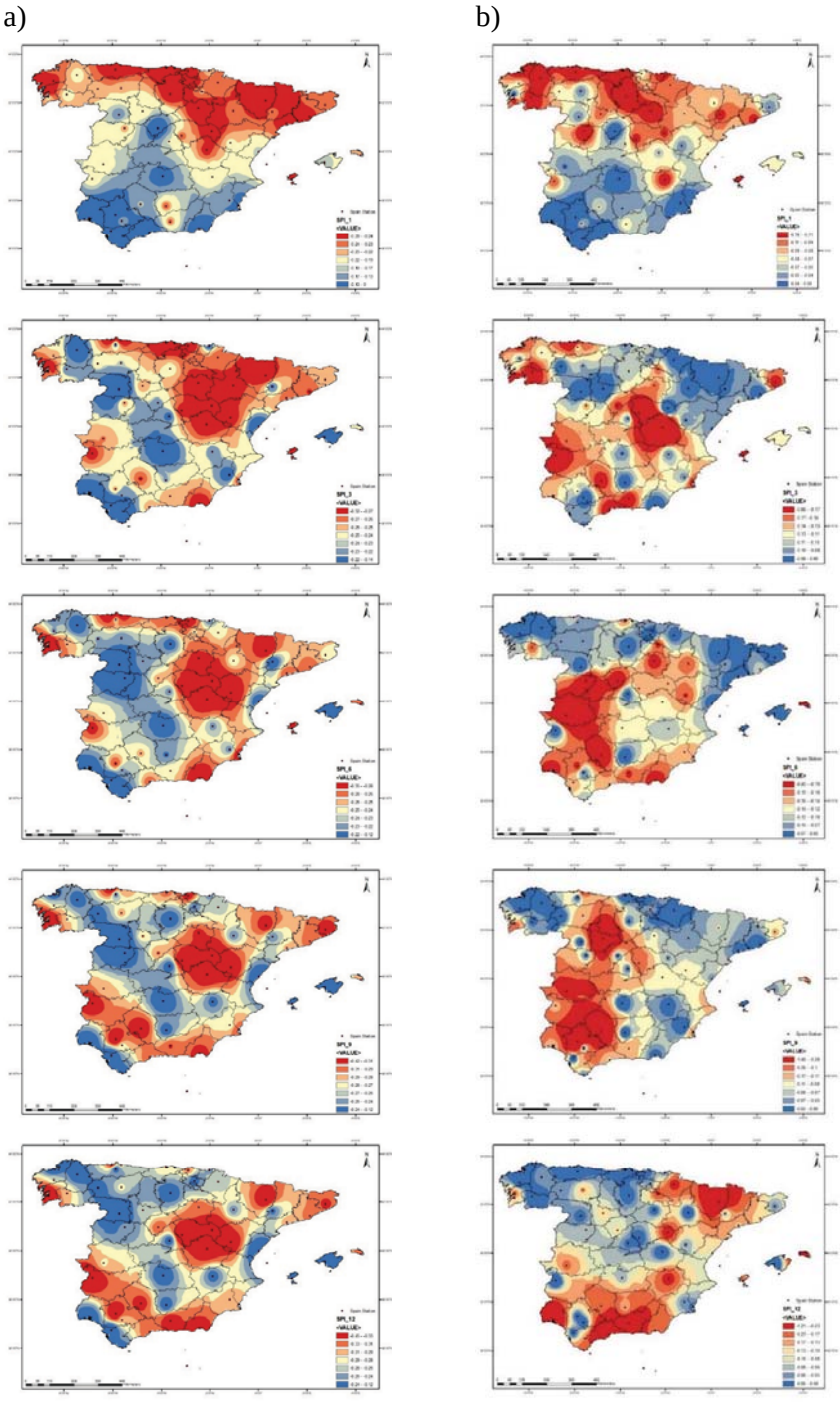

Fig. 4. Detection of drought over time based on SPI (a) observed (b) future

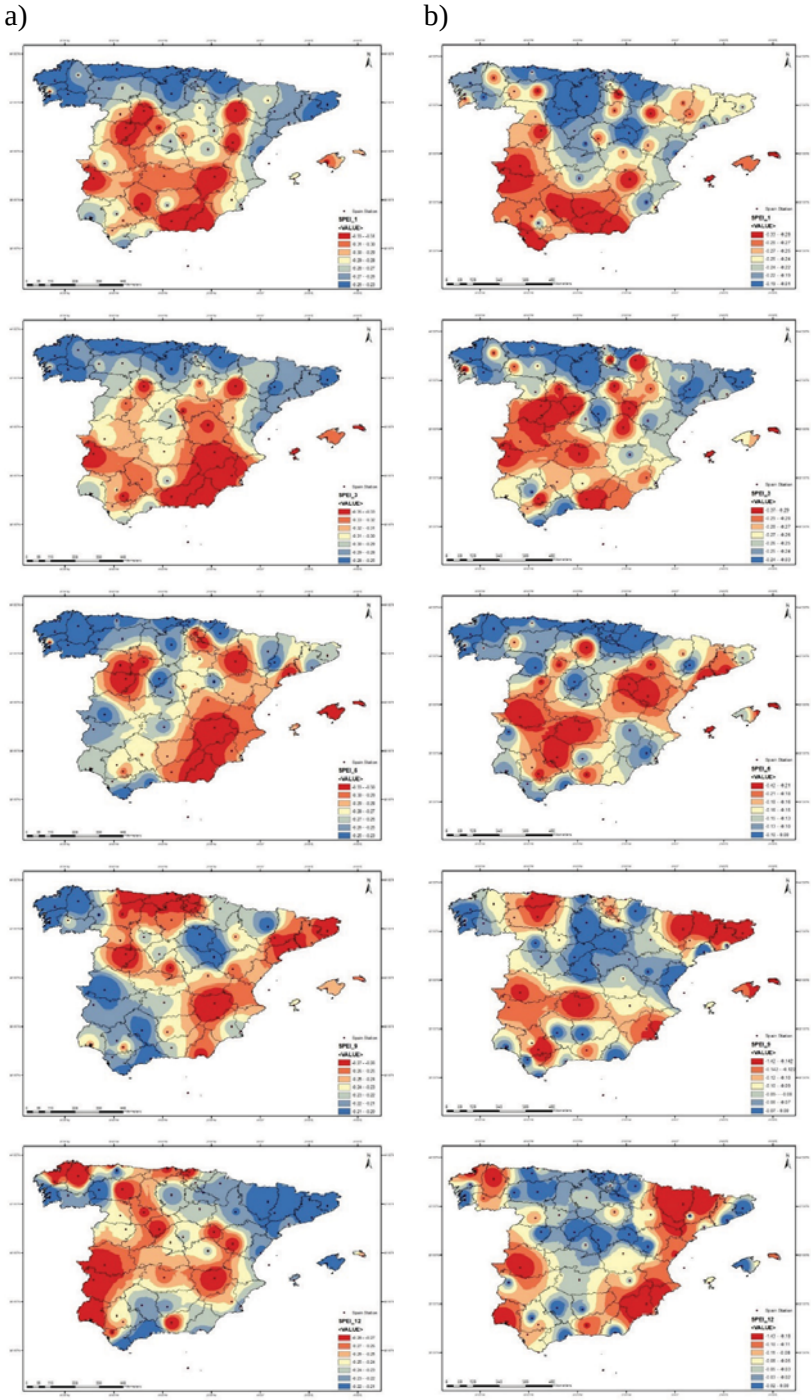

Fig. 5. Detection of drought over time based on SPEI (a) observed (b) future

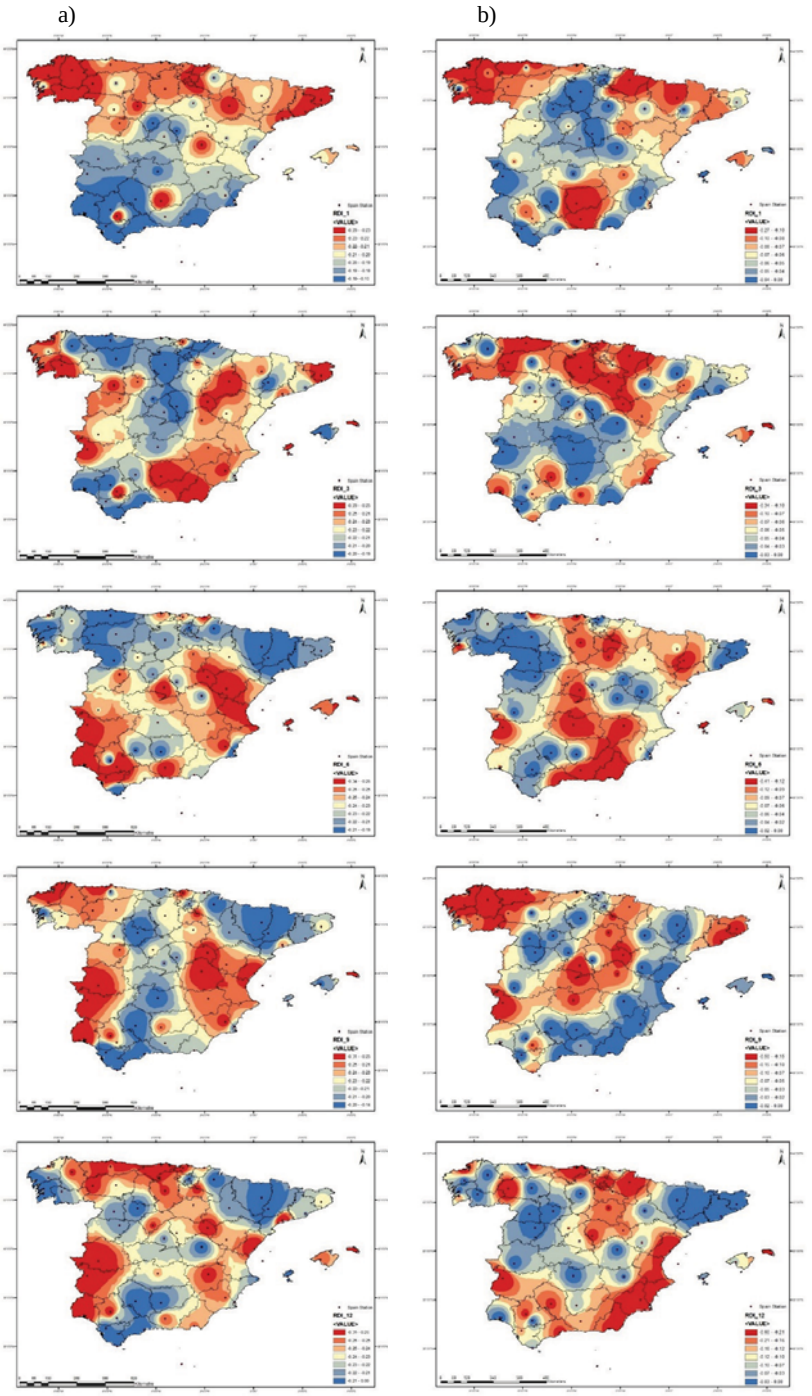

Fig. 6. Detection of drought over time based on RDI (a) observed (b) future.

3.4. Performance of machine learning models

Among machine learning methods, Random Forest is highly successful in modeling multiple variables and complex relationships. In this study, the Random Forest algorithm was used to predict drought indices and make future drought predictions. 80% of the data was used for training, while 20% was reserved for testing. The performance of the obtained test data was evaluated. To assess the model's performance, the R^2, MAE, and RMSE performance metrics were used. The results obtained are shown in *Figs. 10*, *11*, and *12*. It was found that the R^2 values for the 1-month results were lower compared to other time scales.

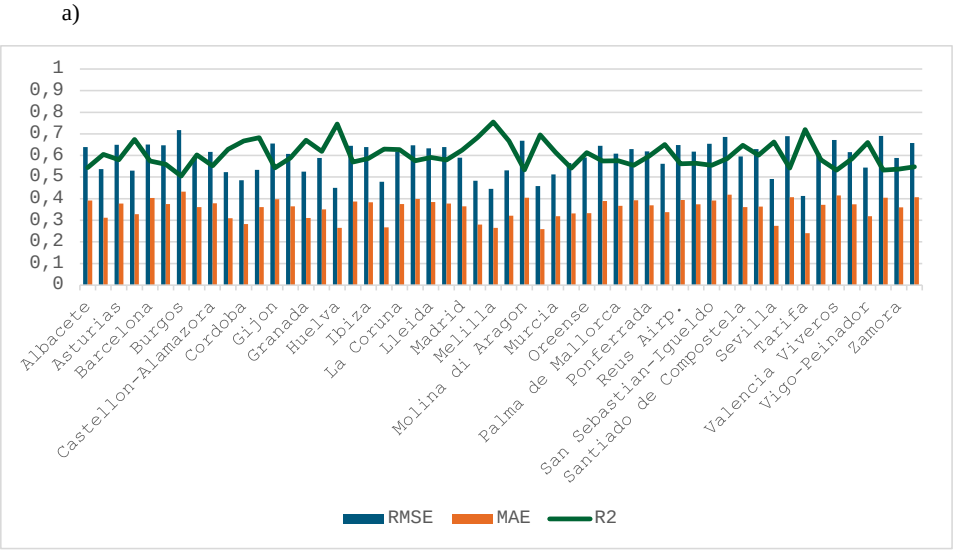

Fig. 7. Evaluation metrics for stations a) evaluation for 1-month SPI, b) evaluation for 3-month SPI, c) evaluation for 6-month SPI, d) evaluation for 9-month SPI, e) evaluation for 12-month SPI

b)

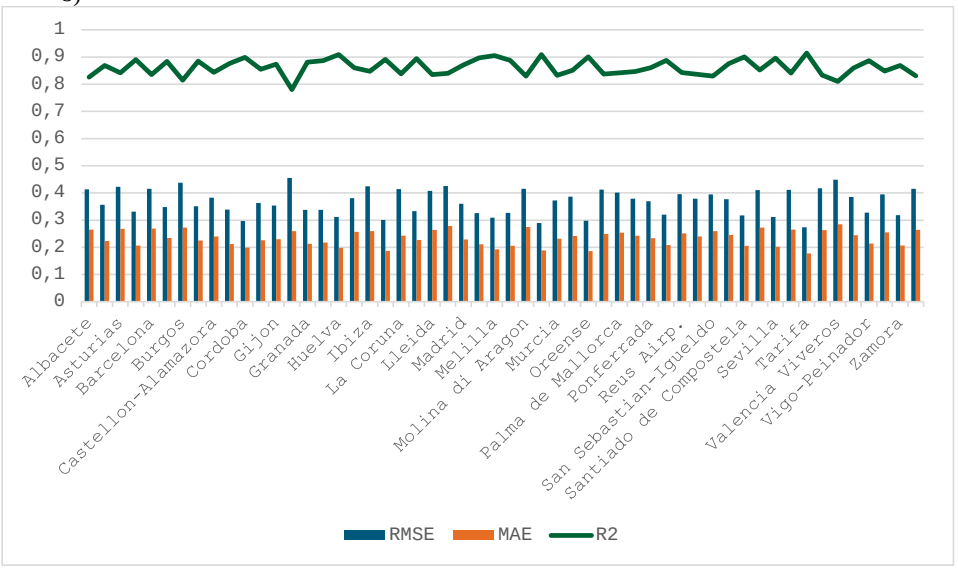

c)

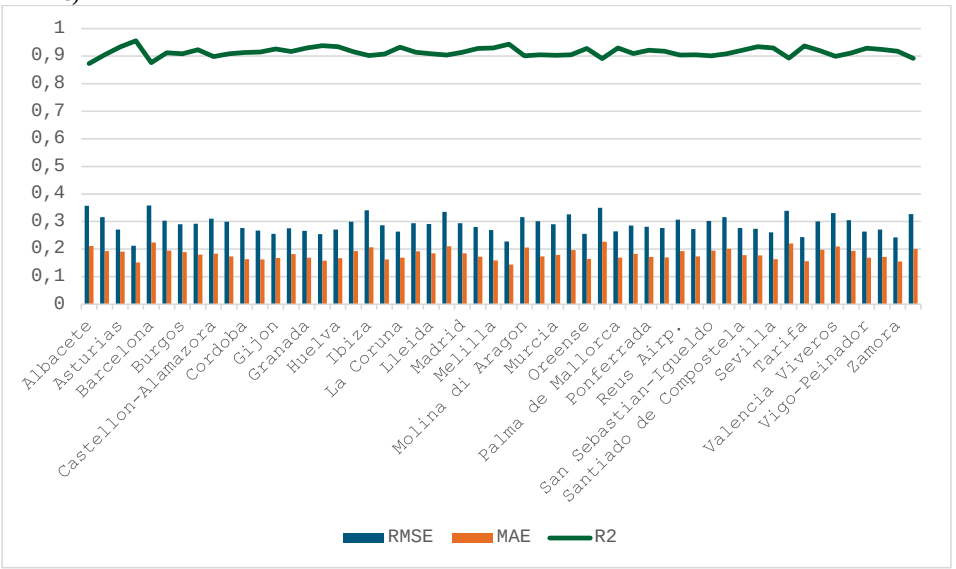

Fig. 7. Continued

d)

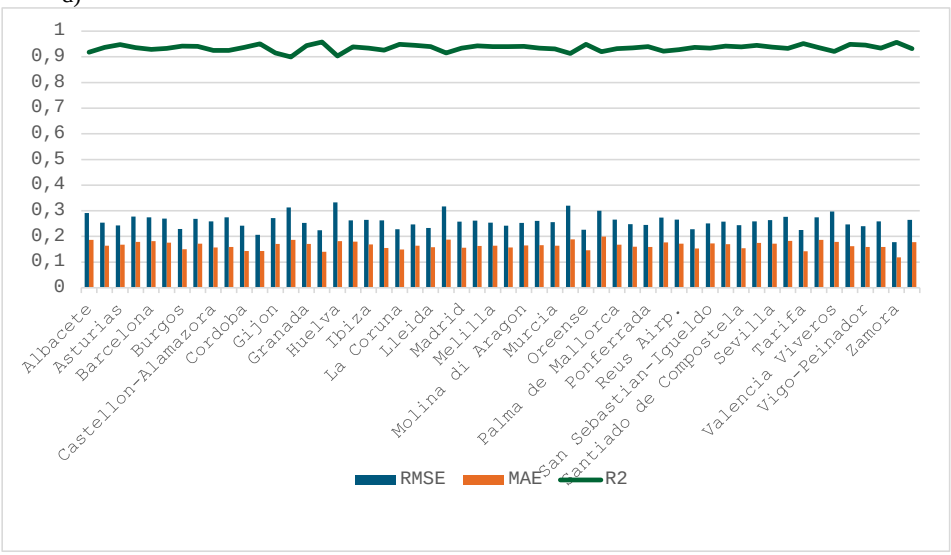

e)

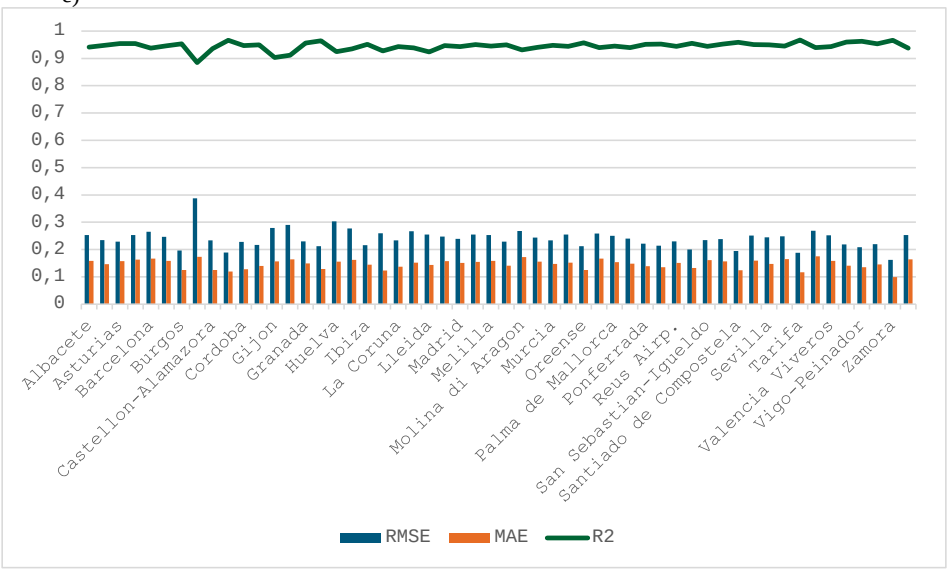

Fig. 7. Evaluation metrics for stations a) evaluation for 1-month SPI, b) evaluation for 3-month SPI, c) evaluation for 6-month SPI, d) evaluation for 9-month SPI, e) evaluation for 12-month SPI (continued)

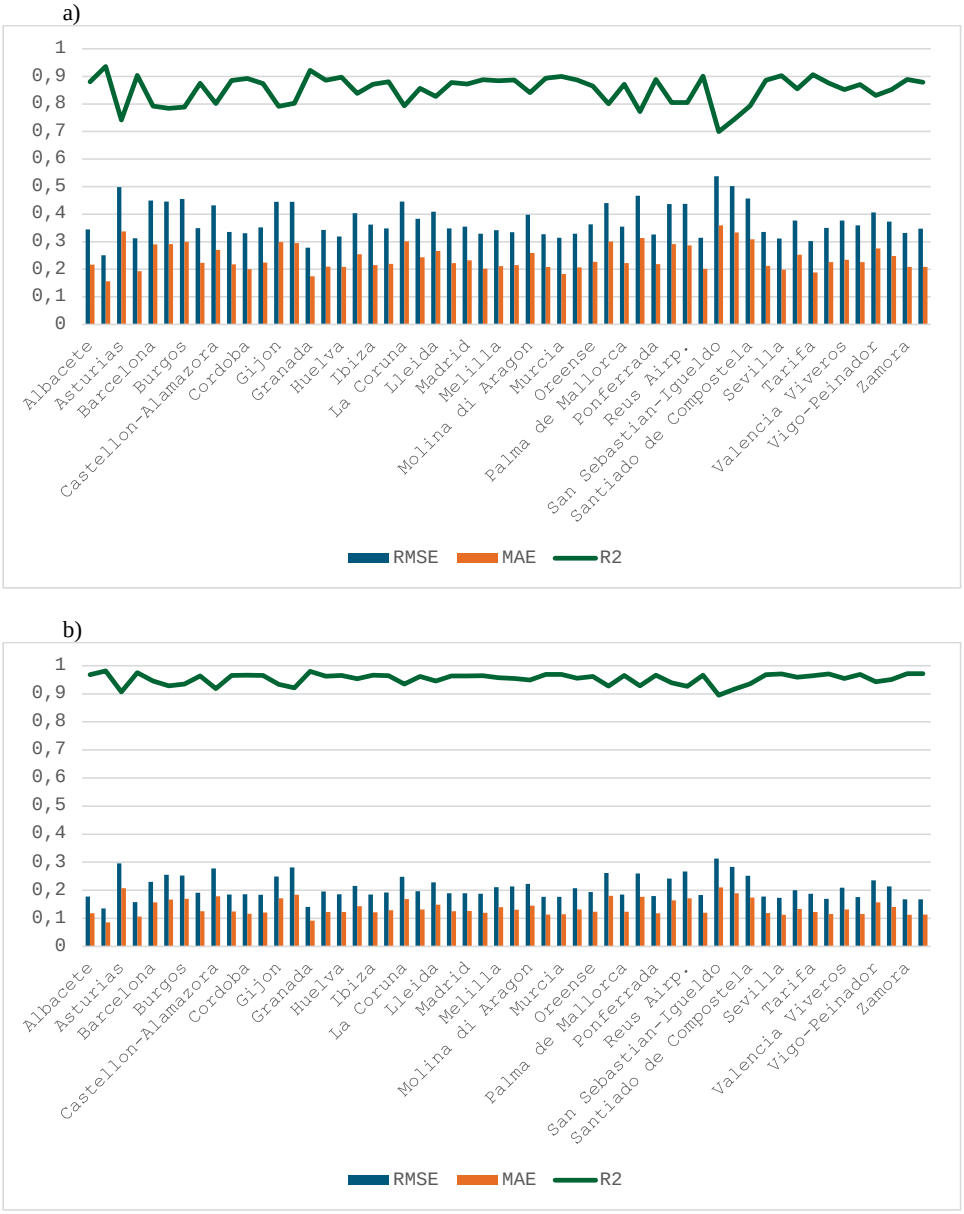

Fig. 8. Evaluation metrics for stations a) evaluation for 1-month SPEI, b) evaluation for 3-month SPEI, c) evaluation for 6-month SPEI, d) evaluation for 9-month SPEI, e) evaluation for 12-month SPEI

c)

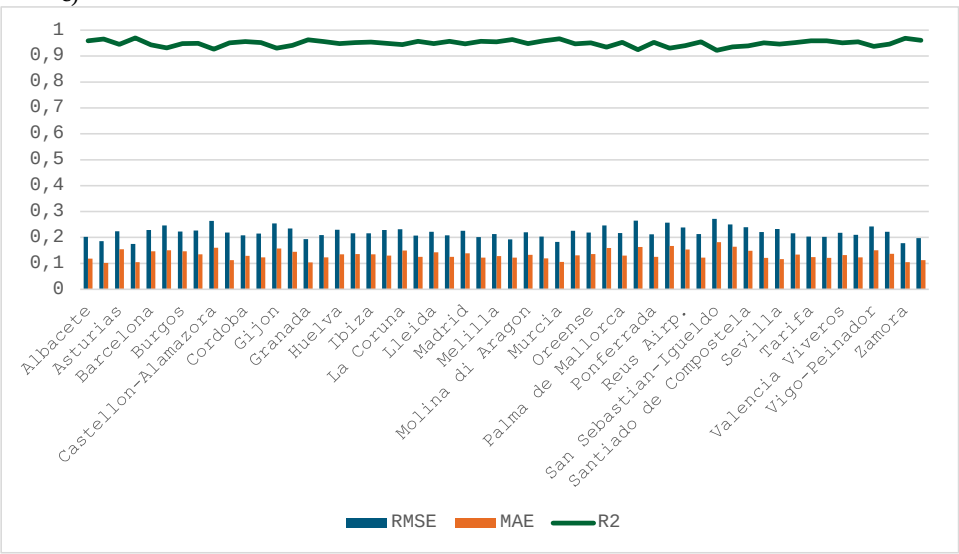

d)

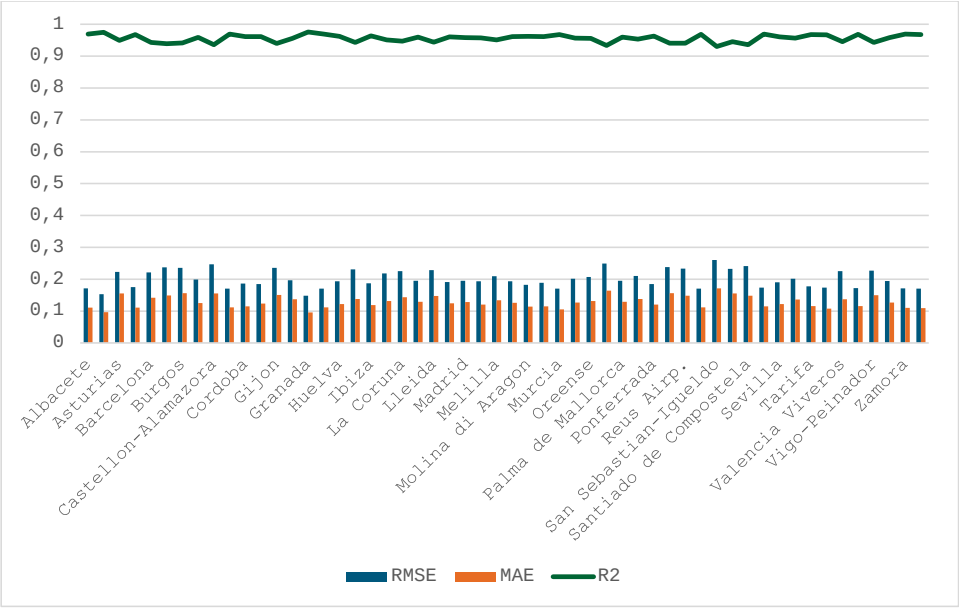

Fig. 8. Continued

e)

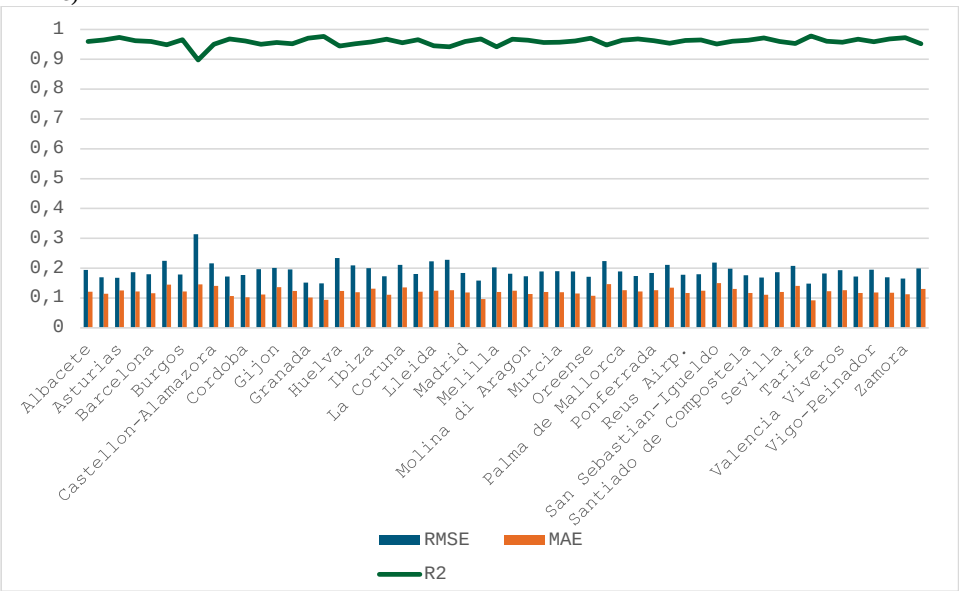

Fig. 8. Continued

a)

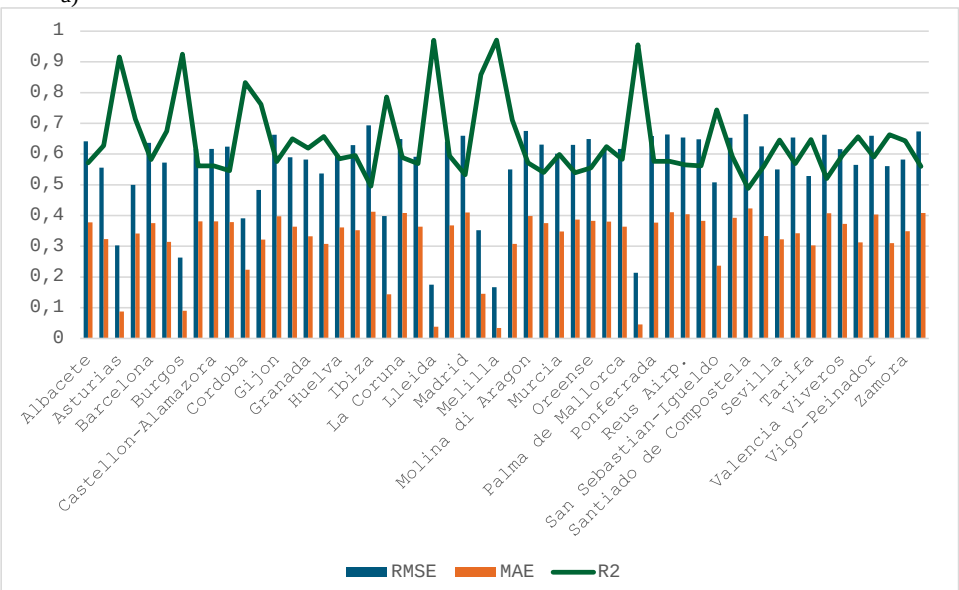

Fig. 9. Evaluation metrics for stations a) evaluation for 1-month RDI, b) evaluation for 3-month RDI, c) evaluation for 6-month RDI, d) evaluation for 9-month RDI, e) evaluation for 12-month RDI

b)

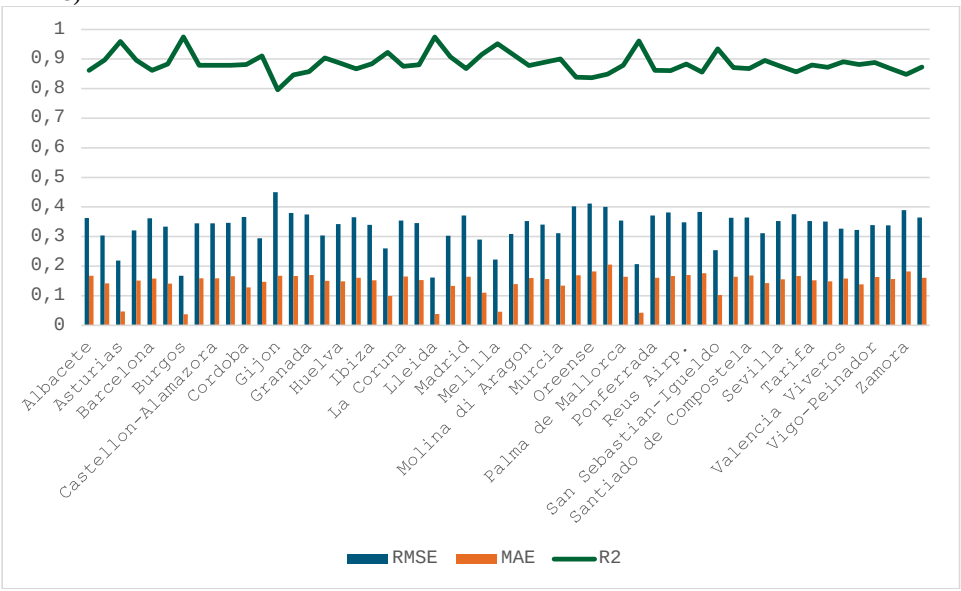

c)

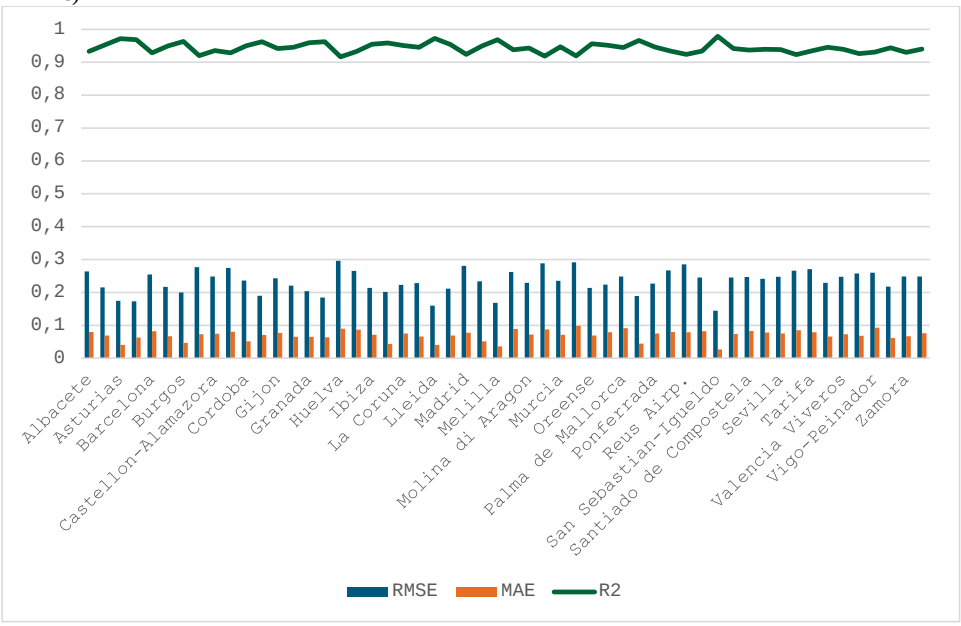

Fig. 9. Continued

d)

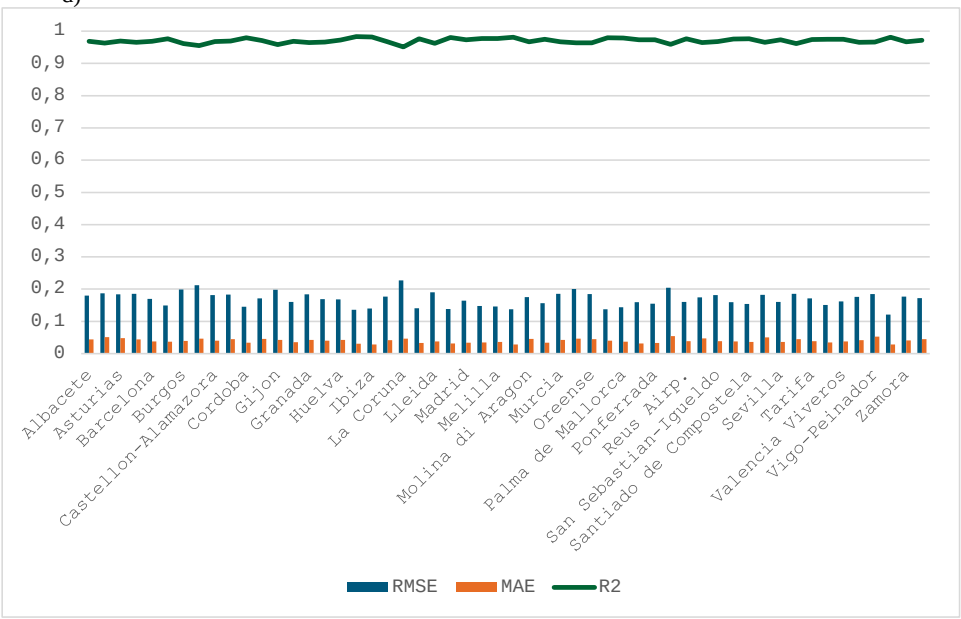

e)

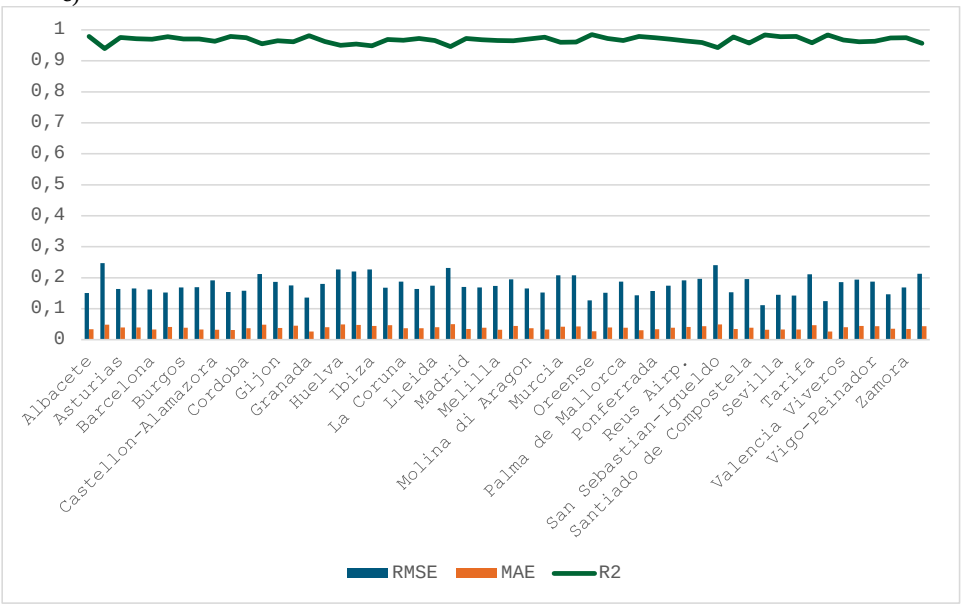

Fig. 9. Evaluation metrics for stations a) evaluation for 1-month RDI, b) evaluation for 3-month RDI, c) evaluation for 6-month RDI, d) evaluation for 9-month RDI, e) evaluation for 12-month RDI (*c*ontinued)

3.5. Correlation of stations

The correlation coefficients between the stations in Spain were calculated for SPI, SPEI, and RDI values across 1, 3, 6, 9, and 12-month time scales (*Appendix 3*, *Figs. 14*, *15*, and *16*). The relationships between meteorological stations were examined across different time scales. The results show that many stations have very high correlation values in terms of drought behavior.

4. Summary and conclusions

This study combines SPI, SPEI, and RDI indices (*Zhou et al., 2013; Tao et al., 2014; Nandgude et al., 2020*) with the Random Forest machine learning algorithm to understand the meteorological drought dynamics in different regions of Spain and make future predictions. One of the most unique contributions of the study is the introduction of a new mapping approach applied for the first time in drought analysis. This method, by identifying the temporal and spatial patterns of drought with high accuracy, offers significant advantages both scientifically and practically.

The results indicate that drought intensity and duration will increase in different regions of Spain, particularly in the southern and central areas, where long-duration drought events will become increasingly severe. Additionally, the northern regions are found to be at a higher risk of short-term droughts. The new drought mapping method, by visualizing these spatial differences, has allowed for the development of region-specific intervention strategies for decision-makers. The maps provide more detailed information about drought intensity and frequency at the regional level, facilitating effective planning at the local scale. Based on time series, this method offers a powerful tool for understanding the temporal variations in drought trends and it can be adapted to different drought indices and time scales, creating a wide range of applications for various environmental and climatic scenarios.

The findings suggest that different regions of Spain should be classified based on their drought risk. With the new mapping method, the following recommendations can be made for developing short- and long-term water management strategies:

1. **Drought management strategies**: In southern regions, investments in water-saving technologies and sustainable agricultural practices should be prioritized to reduce the risk of prolonged droughts. In northern regions, early warning systems and crisis management plans can be developed to mitigate the impacts of short-term droughts.
2. **Guidance for policymakers**: The new mapping method provides concrete guidance for regional policymakers in the process of creating risk reduction

strategies. For example, the distribution and prioritization of water resources can be optimized based on these maps.

3. **Advancement of machine learning methods**: The success of the Random Forest algorithm could be enhanced by incorporating more complex models (e.g., Deep Learning) in the future. This would improve the accuracy of predictions and the reliability of regional forecasts.
4. **Addressing climate change**: The findings show that the drought mapping method is an effective tool for identifying the regional impacts of climate change and developing adaptation strategies for these impacts. It can serve as a fundamental data source for climate change adaptation plans.
5. **Future research**: The drought mapping method can be generalized by testing it in different geographical areas and drought conditions. Additionally, integrating this method with different meteorological datasets and modeling techniques will allow for more comprehensive results.

In conclusion, this study makes significant contributions to both scientific literature and practical policies. The newly developed drought mapping method provides a clearer representation of Spain's drought conditions and risks, aiding in the development of sustainable water management and agricultural policies. Such innovative approaches not only offer a strong model for Spain but also serve as a valuable tool for other regions facing similar climatic challenges.

References

Adnan, S., Ullah, K., Shuanglin, L., Gao, S., Khan, A. H., and *Mahmood, R.,* 2018: Comparison of various drought indices to monitor drought status in Pakistan. *Climate Dynamics*, 51, 1885–1899. https://doi.org/10.1007/s00382-017-3987-0

Alivi, A., Yıldız, O., and *Aktürk, G.*, 2021: Fırat-Dicle havzasında yıllık ortalama akımlar üzerinde iklim değişikliği etkilerinin iklim elastikiyeti metodu ile incelenmesi. *Gazi Üniversitesi Mühendislik Mimarlık Fakültesi Dergisi*, 36, 1449–1466. https://doi.org/10.17341/gazimmfd.739556 (In Turkish)

Allen, R. G., Pereira, L. S., Raes, D., and *Smith, M.*, 1998: Crop evapotranspiration: guidelines for computing crop water requirements. FAO Drainage and Irrigation Paper 56, *Food and Agriculture Organization*, Rome.

Beguería, S., Vicente-Serrano, S. M., Reig, F., and *Latorre, B.*, 2014: Standardized precipitation evapotranspiration index (SPEI) revisited: Parameter fitting, evapotranspiration models, tools, datasets and drought monitoring. *International Journal of Climatology*, 34(10), 3001–3023. https://doi.org/10.1002/joc.3887

Breiman, L., 2001: Random forests. *Machine Learning*, 45(1), 5–32. https://doi.org/10.1023/A:1010933404324

Chen, Y., Chen W., Rahmati, O., Falah, F., and *Kulakowski D.*, 2021: Toward the development of deep learning analyses for snow avalanche releases in mountain regions. *Geocarto International*, 3, 1–26.

García Galiano, S. and *Broekman, A.*, 2023: Drought in Spain: Rising Temperatures and Overexploitation. *Science Media Centre Spain*. Available at: https://sciencemediacentrespain.org/drought-spain

Jain, V. K., Pandey, R. P., Jain, M. K., and *Byun, H. R.*, 2015: Comparison of drought indices for appraisal of drought characteristics in the Ken River Basin. *Weather and Climate Extremes*, 8, 1–11. https://doi.org/10.1016/j.wace.2015.05.002

Jiménez-Donaire, M.P., Giráldez, J.V., and *Vanwalleghem, T.*, 2020: Impact of Climate Change on Agricultural Droughts in Spain. *Water*, 12(3), 867. https://doi.org/10.3390/w12113214

Joint Research Centre, European Commission, 2024: Prolonged drought and record temperatures have critical impact in the Mediterranean. Available at: https://ec.europa.eu/jrc/en/news/prolonged-drought-record-temperatures

Lorenzo-Lacruz, J., Morán-Tejeda, E., Vicente-Serrano, S. M., and *López-Moreno, J. I.*, 2013: Streamflow droughts in the Iberian Peninsula between 1945 and 2005: spatial and temporal patterns. Hydrology and Earth System Sciences, 17(1), 119–134. https://doi.org/10.5194/hess-17-119-2013

McKee, T. B., Doesken, N. J., and *Kleist, J.*, 1993: The relationship of drought frequency and duration to time scales. In Proceedings of the Ninth Conference on Applied Climatology, Anaheim, California, 179–184.

Mishra, A. K. and *Singh, V. P.*, 2010: A review of drought concepts. *Journal of Hydrology*, 391(1–2), 202–216. https://doi.org/10.1016/j.jhydrol.2010.07.012

Nabavi-Pelesaraei, A., Rafee, S., Mohtasebi, S. S., Hosseinzadeh-Bandbafa, H., and *Chau, K.*, 2018: Integration of artificial intelligence methods and life cycle assessment to predict energy output and environmental impacts of paddy production. *Science of the Total Environment*, 631–632, 1279–1294. https://doi.org/10.1016/j.scitotenv.2018.03.088

Paneque, P., 2015: Drought Management Strategies in Spain. *Water*, 7(6), 3082-3106. https://doi.org/10.3390/w7126655

Pedregosa, F., Varoquaux, G., Gramfort, A., Michel, V., Thirion, B., Grisel, O., Blondel, M., Prettenhofer, P., Weiss, R., Dubourg, V., Vanderplas, J., Passos, A., Cournapeau, D., Brucher, M., Perrot, M., and *Duchesnay, E.*, 2011: Scikit-learn: machine learning in Python. Journal of Machine Learning Research, 12, 2825–2830.

Salvador, C., Nieto, R., Linares, C., Díaz, J., and *Gimeno, L.*, 2020: Quantification of the Effects of Droughts on Daily Mortality in Spain. International Journal of Environmental Research and Public Health, 17(13), 4698. https://doi.org/10.3390/ijerph17176114

Sırdaş, S. and *Şen, Z.*, 2003: Meteorolojik kuraklık modellemesi ve Türkiye uygulaması. *İTÜDERGİSİ/d*, 2, 95–103. (In Turkish)

Sierra-Soler, A., Adamowski, J., Malard, J., Qi, Z., Saadat, H., and *Pingale, S.* (2016). Assessing agricultural drought at a regional scale using LULC classification, SPI, and vegetation indices: Case study in a rainfed agro-ecosystem in Central Mexico. *Geomatics, Natural Hazards and Risk*, 7(4), 1460–1488. https://doi.org/10.1080/19475705.2015.1073799

Telesca, L., Lovallo, M., Lopez-Moreno, I., and *Vicente-Serrano, S.*, 2012: Investigation of scaling properties in monthly streamflow and Standardized Streamflow Index (SSI) time series in the Ebro basin (Spain). *Physica A*, 391(4), 1662–1678. https://doi.org/10.1016/j.physa.2011.10.023

Thom, H. C. S., 1966: Some Methods of Climatological Analysis. WMO Technical Note, No. 81, World Meteorological Organization, Geneva, Switzerland, 63.

Thornthwaite, C. W., 1948: An Approach toward a Rational Classification of Climate. *Geographical Review*, 38(1), 55–94. https://doi.org/10.2307/210739

Tigkas, D., Vangelis, H., and *Tsakiris, G.*, 2013: The Drought Indices Calculator (DrinC). In Proceedings of 8th International Conference of EWRA: Water Resources Management in an Interdisciplinary and Changing Context, 1333–1342.

Tsakiris, G. and *Vangelis, H.*, 2004: Towards a drought watch system based on spatial SPI. *Water Resources Management*, 18(1), 1–12. https://doi.org/10.1023/B:WARM.0000015410.47014.a4

Tsakiris, G. and *Vangelis, H.*, 2005: Establishing a drought index incorporating evapotranspiration. *European Water*, 9(10), 3–11.

Tsakiris, G., Pangalou, D., and *Vangelis, H.*, 2007: Regional drought assessment based on the Reconnaissance Drought Index (RDI). *Water Resources Management*, 21(5), 821–833. https://doi.org/10.1007/s11269-006-9105-4

Vicente-Serrano, S. M., Beguería, S., and *López-Moreno, J. I.*, 2011: Comment on "Characteristics and trends in various forms of the Palmer Drought Severity Index (PDSI) during 1900-2008" by Aiguo

Dai. *Journal of Geophysical Research: Atmospheres*, 116, D19112. https://doi.org/10.1029/2011JD016410

Vicente-Serrano, S. M., Beguería, S., López-Moreno, J. I., Angulo, M., and *El Kenawy, A.*, 2010: A new global 0.5° gridded dataset (1901–2006) of a multiscalar drought index: Comparison with current drought index datasets based on the Palmer Drought Severity Index. *Journal of Hydrometeorology*, 11(4), 1033–1043. https://doi.org/10.1175/2010JHM1224.1

Vicente-Serrano, S. M., Beguería, S., Lorenzo-Lacruz, J., Camarero, J. J., López-Moreno, J. I., Azorin-Molina, C., Revuelto, J., Morán-Tejeda, E., and *Sanchez-Lorenzo, A.*, 2012: Performance of drought indices for ecological, agricultural, and hydrological applications. Earth Interactions, 16(10), 1–27. https://doi.org/10.1175/2012EI000434.1

Vicente-Serrano, S. M., López-Moreno, J. I., Beguería, S., Lorenzo-Lacruz, J., Sanchez-Lorenzo, A., García-Ruiz, J. M., Azorin-Molina, C., Morán-Tejeda, E., Revuelto, J., Trigo, R., Coelho, F., and *Espejo, F.*, 2014: Evidence of increasing drought severity caused by temperature rise in southern Europe. Environmental Research Letters, 9(4), 044001. https://doi.org/10.1088/1748-9326/9/4/044001

Vicente-Serrano, S. M., McVicar, T. R., Miralles, D. G., Yang, Y., and *Tomas-Burguera, M.*, 2020: Unraveling the influence of atmospheric evaporative demand on drought and its response to climate change. Wiley Interdisciplinary Reviews: Climate Change, 11(2), e632. https://doi.org/10.1002/wcc.632

Wang, L., Yu, H., Yang, M., Yang, R., Gao, R., and *Wang Y.*, 2019: A drought index: the standardized precipitation evapotranspiration runoff index. *Journal of Hydrology*, 571, 651–668. https://doi.org/10.1016/j.jhydrol.2019.02.023

Wang, W., Guo, B., Zhang, Y., Zhang, L., Ji, M., Xu, Y., Zhang, X., and *Zhang, Y.* 2021: The sensitivity of the SPEI to potential evapotranspiration and precipitation at multiple timescales on the Huang-Huai-Hai Plain, China. *Theoretical and Applied Climatology*, 143, 87–99. https://doi.org/10.1007/s00704-020-03394-y

Wilhite, D. A. and *Glantz, M. H.*, 1985: Understanding: the Drought Phenomenon: The Role of Definitions. *Water International*, 10, 111–120. https://doi.org/10.1080/02508068508686328

Zarch, M. A. A., Sivakumar, B., and *Sharma, A.*, 2015: Droughts in a warming climate: A global assessment of Standardized Precipitation Index (SPI) and Reconnaissance Drought Index (RDI). *Journal of Hydrology*, 526, 183–195. https://doi.org/10.1016/j.jhydrol.2014.09.071

Zarei, A. R., Shabani, A., and *Moghimi, M. M.*, 2021: Accuracy Assessment of the SPEI, RDI and SPI Drought Indices in Regions of Iran with Different Climate Conditions. *Pure and Applied Geophysics*, 178, 1387–1403. https://doi.org/10.1007/s00024-021-02704-3

Zhang, Y., Li, H., and *Reggiani, P.*, 2019: Climate variability and climate change impacts on land surface. *Hydrology and Earth System Sciences*, 11, 1492. https://doi.org/10.3390/w11071492

Zuo, D., Cai, S., Xu, Z., Li, F., Sun, W., Yang, X., Kan, G., and *Liu, P.*, 2018: Spatiotemporal patterns of drought at various time scales in Shandong Province of Eastern China. *Theoretical and Applied Climatology*, 131(1–2), 271–284. https://doi.org/10.1007/s00704-016-1969-5

APPENDIX 1

```
import numpy as np
import pandas as pd
from sklearn.ensemble import RandomForestRegressor
from sklearn.preprocessing import MinMaxScaler
from sklearn.metrics import mean_squared_error, mean_absolute_error, r2_score
from sklearn.model_selection import train_test_split
import matplotlib.pyplot as plt
import os

# Load data
data = pd.read_csv('spi_data.csv')

# Convert to DateTime format
data['date'] = pd.to_datetime(data['date'])
data.set_index('date', inplace=True)

# Extract SPI values
spi_values = data['spi'].values.reshape(-1, 1)

# Scale data
scaler = MinMaxScaler(feature_range=(0, 1))
spi_scaled = scaler.fit_transform(spi_values)

# Prepare training and test data
def create_dataset(dataset, look_back=1):
    X, Y = [], []
    for i in range(len(dataset) - look_back):
        a = dataset[i:(i + look_back), 0]
        X.append(a)
        Y.append(dataset[i + look_back, 0])
    return np.array(X), np.array(Y)

look_back = 12  # 1 year
X, y = create_dataset(spi_scaled, look_back)

# Split into training and test sets
X_train, X_test, y_train, y_test = train_test_split(X, y, test_size=0.20, shuffle=False)
```

```
# Create and train the model
model = RandomForestRegressor(n_estimators=10, max_depth=55, random_state=900)
model.fit(X_train, y_train)

# Make predictions
train_predict = model.predict(X_train)
test_predict = model.predict(X_test)

# Inverse scale the predictions
train_predict = scaler.inverse_transform(train_predict.reshape(-1, 1))
y_train = scaler.inverse_transform(y_train.reshape(-1, 1))
test_predict = scaler.inverse_transform(test_predict.reshape(-1, 1))
y_test = scaler.inverse_transform(y_test.reshape(-1, 1))

# Add predictions to the time axis
train_predict_plot = np.empty_like(spi_values)
train_predict_plot[:, :] = np.nan
train_predict_plot[look_back:len(train_predict) + look_back, :] = train_predict

test_predict_plot = np.empty_like(spi_values)
test_predict_plot[:, :] = np.nan
test_predict_plot[len(train_predict) + look_back:len(test_predict) + len(train_predict) + look_back, :] = test_predict

# Plot the predictions
plt.figure(figsize=(15, 6))
plt.plot(data.index, spi_values, label='Actual Values')
plt.plot(data.index, train_predict_plot, label='Training Predictions')
plt.plot(data.index, test_predict_plot, label='Test Predictions')
plt.legend()
plt.savefig('prediction_results_spi.png')
plt.show()

# Create a list for future predictions
future_predictions = []
last_data = spi_scaled[-look_back:].reshape(1, look_back)

for _ in range(50 * 12):  # 50 years, monthly predictions
    future_pred = model.predict(last_data)
    future_predictions.append(future_pred[0])
    last_data = np.append(last_data[:, 1:], future_pred.reshape(1, -1), axis=1)
```

```
# Inverse scale future predictions
future_predictions = scaler.inverse_transform(np.array(future_predictions).reshape(-1, 1))

# Combine future predictions with time series
future_dates = pd.date_range(start=data.index[-1] + pd.DateOffset(months=1), periods=50*12, freq='M')
future_spi = pd.DataFrame(data=future_predictions, index=future_dates, columns=['spi'])

# Create a new DataFrame to show results from 2023 onward
start_date = '2023-12-01'
result_index = data.index.append(future_spi.index)
results = pd.DataFrame(index=result_index)

# Add actual values
results['Actual Values'] = np.nan
results['Actual Values'].loc[data.index] = data['spi']

# Add training and test predictions
results['Training Predictions'] = np.nan
results['Test Predictions'] = np.nan

train_predict_index = data.index[look_back:len(train_predict) + look_back]
test_predict_index = data.index[len(train_predict) + look_back:len(train_predict) + look_back + len(test_predict)]

results.loc[train_predict_index, 'Training Predictions'] = train_predict.flatten()
results.loc[test_predict_index, 'Test Predictions'] = test_predict.flatten()

# Add future predictions
results['Future Predictions'] = np.nan
results.loc[future_spi.index, 'Future Predictions'] = future_predictions.flatten()

# Save results to Excel
results.to_excel('spi_prediction_results_1.xlsx')

# Plot future predictions separately
plt.figure(figsize=(15, 6))
plt.plot(future_spi.index, future_spi['spi'], label='Future Predictions', color='red')
plt.title('Future Predictions')
```

```
plt.xlabel('Date')
plt.ylabel('SPI Value')
plt.legend()
plt.savefig('future_predictions_spi.png')
plt.show()

# Plot combined results
plt.figure(figsize=(15, 6))
plt.plot(results.index, results['Actual Values'], label='Actual Values')
plt.plot(results.index, results['Training Predictions'], label='Training Predictions')
plt.plot(results.index, results['Test Predictions'], label='Test Predictions')
plt.plot(results.index, results['Future Predictions'], label='Future Predictions')
plt.legend()
plt.savefig('SPI_1.png')
plt.show()

# Calculate performance metrics
train_rmse = np.sqrt(mean_squared_error(y_train, train_predict))
train_mae = mean_absolute_error(y_train, train_predict)
train_r2 = r2_score(y_train, train_predict)

print(f"Training RMSE: {train_rmse}")
print(f"Training MAE: {train_mae}")
print(f"Training R2: {train_r2}")

# Create folder for saving plots
os.makedirs('plots_spi', exist_ok=True)

# Save plots to folder
plt.figure(figsize=(15, 6))
plt.plot(data.index, spi_values, label='Actual Values')
plt.plot(data.index, train_predict_plot, label='Training Predictions')
plt.plot(data.index, test_predict_plot, label='Test Predictions')
plt.legend()
plt.savefig('plots_spi/prediction_results_spi.png')
plt.show()

plt.figure(figsize=(15, 6))
plt.plot(results.index, results['Future Predictions'], label='Future Predictions')
plt.legend()
plt.savefig('plots_spi/future_predictions_spi.png')
plt.show()
```

```
plt.figure(figsize=(15, 6))
plt.plot(results.index, results['Actual Values'], label='Actual Values')
plt.plot(results.index, results['Training Predictions'], label='Training Predictions')
plt.plot(results.index, results['Test Predictions'], label='Test Predictions')
plt.plot(results.index, results['Future Predictions'], label='Future Predictions')
plt.legend()
plt.savefig('plots_spi/SPI_1.png')
plt.show()
```

APPENDIX 2

Table 3. Percentage classification values of drought based on 1-month SPI results (%)

		Menorca	Molina di Aragon	Moron de la Frontera	Murcia	Murcia-San Javier	Oreense	Oviedo	Palma de Mallorca	Pamplona-Noain	Ponferrada	Pontevedra	Reus Airp.	Salamanca	San Sebastian-Igueldo	Santander	Santiado de Compostela	Segovia	Sevilla	Soria	Tarifa	Toledo	Valencia Viveros	Valladolid	Vigo-Peinador	Vitoria	Zamora	Zaragoza
Extremely Wet	> 2.0	1.1	1.3	1.6	2.0	2.1	2.8	2.1	2.3	1.5	2.6	2.0	1.1	1.3	2.8	2.8	1.5	1.6	1.5	2.6	1.0	2.0	2.6	2.1	1.8	2.5	2.1	1.3
Very Wet	1.5 – 2.0	3.9	4.1	3.1	3.4	4.1	5.9	5.7	4.9	3.6	4.3	4.4	4.6	4.1	5.1	4.4	3.4	4.6	2.6	3.8	2.8	4.9	5.2	2.8	3.9	4.9	4.9	4.3
Moderately Wet	1.0 – 1.5	9.2	7.9	8.0	9.8	9.5	8.0	8.0	9.2	6.2	8.2	7.7	8.2	9.0	8.3	7.0	7.5	9.5	8.8	9.3	8.2	8.0	8.8	8.8	7.2	8.2	7.7	10.3
Near Normal	-1.0 – 1.0	69.1	66.4	87.2	70.5	77.4	67.9	66.4	70.4	73.3	71.4	71.7	67.3	68.7	68.9	66.1	70.7	66.9	87.1	68.6	88.1	68.6	68.2	71.0	73.3	65.8	73.0	69.2
Moderately Dry	-1.5 – -1.0	10.8	12.9	0.0	14.2	6.9	9.3	11.0	9.0	9.2	7.7	8.0	11.8	11.1	9.2	12.4	9.7	10.6	0.0	8.0	0.0	10.1	7.7	9.0	6.9	9.0	10.5	8.5
Severely Dry	-2.0 – -1.5	5.9	5.9	0.0	0.0	0.0	5.6	4.9	4.3	5.9	3.8	4.6	7.0	5.7	3.8	4.7	5.2	6.7	0.0	5.2	0.0	6.4	7.4	6.2	5.4	7.4	1.8	4.6
Extremely Dry	< -2.0	0.0	1.5	0.0	0.0	0.0	0.5	1.8	0.0	0.3	2.1	1.6	0.0	0.0	2.0	2.5	2.0	0.0	0.0	2.5	0.0	0.0	0.0	0.0	0.0	1.5	2.3	0.0
	Total %	100	100	100	100	100	100	100	100	100	100	100	100	100	100	100	100	100	100	100	100	100	100	100	100	100	100	100

		Albacete	Almeria	Asturias	Badajoz Airp.	Barcelona	Bilbao	Burgos	Caceres	Castellon-Alamazora	Ciudad	Cordoba	Cuenca	Gijon	Girona	Granada	Guadalajara	Huelva	Huesca	Ibiza	Jerez de la Frontera	La Coruna	Leon-Virgen del Camino	Lleida	Logrono-Agoncillo	Madrid	Malaga	Melilla
Extremely Wet	> 2.0	2.6	1.6	1.8	2.6	2.3	2.6	1.8	3.4	2.8	2.0	1.5	1.5	2.3	2.0	2.0	0.7	2.5	1.3	2.0	1.5	2.3	2.1	2.3	2.0	2.1	1.6	1.8
Very Wet	1.5 – 2.0	4.7	4.9	5.1	2.6	5.1	4.1	3.6	3.8	4.4	3.8	2.9	2.8	3.6	3.6	3.9	3.6	3.3	3.9	4.1	4.6	6.1	4.1	4.3	5.9	4.3	4.1	4.3
Moderately Wet	1.0 – 1.5	9.0	6.7	8.8	7.0	8.3	8.2	7.7	10.1	10.1	6.7	8.2	8.3	10.0	8.7	5.7	8.7	9.3	6.7	8.7	7.4	8.5	7.4	9.0	8.5	6.2	8.3	8.3
Near Normal	-1.0 – 1.0	68.4	83.3	66.6	72.0	66.0	66.4	68.9	65.5	68.9	76.6	70.4	69.9	68.7	70.2	69.9	68.1	84.9	67.1	65.8	86.6	67.8	70.5	66.8	69.4	72.7	85.9	69.9
Moderately Dry	-1.5 – -1.0	9.5	3.4	10.8	15.7	10.8	12.3	8.8	17.2	8.7	11.0	17.0	11.0	10.8	7.5	18.5	16.2	0.0	11.9	16.9	0.0	8.2	10.0	11.8	8.2	10.0	0.0	15.7
Severely Dry	-2.0 – -1.5	5.7	0.0	4.6	0.0	5.2	4.3	5.7	0.0	5.1	0.0	0.0	6.5	3.3	6.4	0.0	2.8	0.0	8.7	2.6	0.0	4.9	5.4	4.9	3.8	4.7	0.0	0.0
Extremely Dry	< -2.0	0.0	0.0	2.3	0.0	2.3	2.1	3.4	0.0	0.0	0.0	0.0	0.0	1.3	1.6	0.0	0.0	0.0	0.3	0.0	0.0	2.3	0.5	1.0	2.3	0.0	0.0	0.0
	Total %	100	100	100	100	100	100	100	100	100	100	100	100	100	100	100	100	100	100	100	100	100	100	100	100	100	100	100

Table 4. Percentage classification values of drought based on 3-month SPI results (%)

		Albacete	Almeria	Asturias	Badajoz Airp.	Barcelona	Bilbao	Burgos	Caceres	Castellon-Alamazora	Ciudad	Cordoba	Cuenca	Gijon	Girona	Granada	Guadalajara	Huelva	Huesca	Ibiza	Jerez de la Frontera	La Coruna	Leon-Virgen del Camino	Lleida	Logrono-Agoncillo	Madrid	Malaga	Melilla
Extremely Wet	> 2.0	2.0	2.6	3.6	3.0	2.0	2.1	1.6	4.9	3.3	1.8	1.1	0.8	2.8	1.5	2.6	1.0	3.3	0.3	2.1	1.5	2.8	2.5	1.3	1.1	2.5	1.8	2.0
Very Wet	1.5 – 2.0	5.6	3.4	4.9	3.1	5.4	5.3	2.8	4.8	3.6	3.4	2.5	2.6	3.6	5.4	3.0	2.3	3.6	2.8	4.3	2.3	5.7	3.3	3.8	4.9	2.0	3.1	3.3
Moderately Wet	1.0 – 1.5	9.4	7.1	6.2	4.9	8.9	7.4	8.0	6.7	11.3	6.2	6.4	5.9	8.2	8.5	6.1	6.1	7.4	7.1	9.5	8.0	11.3	7.4	9.7	13.6	7.1	6.9	9.4
Near Normal	-1.0 – 1.0	66.3	67.3	64.4	70.0	63.2	62.4	71.6	67.2	69.8	75.0	71.9	71.4	65.5	68.0	71.6	70.1	71.6	66.7	63.5	73.9	63.5	68.5	65.8	63.2	73.4	70.0	68.1
Moderately Dry	-1.5 – -1.0	10.2	10.3	12.8	10.7	10.2	11.5	7.7	8.5	6.4	10.0	10.5	10.5	12.3	9.9	9.5	11.0	8.5	11.2	11.3	9.4	10.5	12.0	12.2	9.7	8.9	10.0	10.7
Severely Dry	-2.0 – -1.5	3.9	6.2	4.9	5.3	5.3	6.7	5.3	5.6	4.3	3.4	5.6	6.1	4.9	4.1	4.4	7.4	5.6	9.0	4.9	4.9	3.6	3.3	3.6	4.6	4.9	7.1	4.6
Extremely Dry	< -2.0	2.6	3.0	3.1	3.1	5.1	4.6	3.3	2.3	1.3	0.0	2.0	2.6	2.6	2.6	2.8	2.1	0.0	3.0	4.3	0.0	2.5	3.1	3.6	2.8	1.3	1.3	2.0
	Total %	100	100	100	100	100	100	100	100	100	100	100	100	100	100	100	100	100	100	100	100	100	100	100	100	100	100	100

		Menorca	Molina di Aragon	Moron de la Frontera	Murcia	Murcia-San Javier	Oreense	Oviedo	Palma de Mallorca	Pamplona-Noain	Ponferrada	Pontevedra	Reus Airp.	Salamanca	San Sebastian-Igueldo	Santander	Santiado de Compostela	Segovia	Sevilla	Soria	Tarifa	Toledo	Valencia Viveros	Valladolid	Vigo-Peinador	Vitoria	Zamora	Zaragoza
Extremely Wet	> 2.0	0.5	1.3	2.0	2.6	3.1	1.8	3.9	3.1	0.8	2.3	2.1	1.5	1.3	2.3	2.5	1.6	2.3	1.5	2.1	0.2	2.0	1.8	1.5	2.3	2.0	1.1	1.1
Very Wet	1.5 – 2.0	4.3	3.4	2.0	3.0	4.3	5.1	3.8	4.6	5.1	5.3	3.8	3.3	2.8	6.1	4.6	3.8	5.4	3.0	4.8	2.8	5.1	5.6	3.9	3.8	3.8	5.1	3.1
Moderately Wet	1.0 – 1.5	9.4	7.1	7.2	7.6	7.2	9.0	9.2	11.8	5.9	8.5	7.7	7.1	7.2	8.5	8.0	7.7	6.6	5.9	7.9	8.2	6.7	8.5	8.2	6.7	9.4	8.4	9.4
Near Normal	-1.0 – 1.0	70.4	67.0	72.6	72.2	67.3	71.1	67.5	68.5	68.8	68.1	70.8	70.1	70.4	66.7	62.6	69.5	67.2	71.4	67.7	73.9	66.8	68.5	67.3	69.1	64.5	74.7	70.0
Moderately Dry	-1.5 – -1.0	8.5	10.3	8.7	8.7	9.7	8.2	11.2	6.9	11.5	9.7	9.9	9.5	11.5	10.7	12.3	9.4	10.5	9.5	10.7	7.4	10.3	9.0	10.3	11.0	11.8	7.2	10.5
Severely Dry	-2.0 – -1.5	3.8	7.2	5.9	4.1	6.7	3.1	2.3	4.3	5.1	3.4	3.9	5.7	4.6	3.4	6.4	5.1	5.1	6.6	4.1	6.6	6.2	4.1	6.1	5.3	4.6	3.0	3.9
Extremely Dry	< -2.0	3.1	3.6	1.6	1.8	1.6	1.6	2.1	0.8	2.8	2.6	1.8	2.8	2.1	2.3	3.6	3.0	3.0	2.1	2.8	1.0	2.8	2.5	2.6	1.8	3.9	0.5	2.0
	Total %	100	100	100	100	100	100	100	100	100	100	100	100	100	100	100	100	100	100	100	100	100	100	100	100	100	100	100

Table 5. Percentage classification values of drought based on 6-month SPI results (%)

		Albacete	Almeria	Asturias	Badajoz Airp.	Barcelona	Bilbao	Burgos	Caceres	Castellon-Alamaziora	Ciudad	Cordoba	Cuenca	Gijon	Girona	Granada	Guadalajara	Huelva	Huesca	Ibiza	Jerez de la Frontera	La Coruna	Leon-Virgen del Camino	Lleida	Logrono-Agoncillo	Madrid	Malaga	Melilla
Extremely Wet	> 2.0	2.1	2.3	3.0	2.5	0.8	1.8	0.3	5.4	1.3	1.5	0.7	0.3	2.1	2.0	2.3	0.8	4.3	0.0	1.5	1.7	3.0	2.5	0.7	1.7	0.8	2.1	1.7
Very Wet	1.5 – 2.0	3.8	3.5	4.3	2.5	7.3	4.5	3.3	4.5	5.9	2.1	3.1	1.2	4.5	4.5	3.8	1.0	2.5	0.8	2.6	2.1	4.6	2.8	2.8	4.3	3.1	3.5	4.0
Moderately Wet	1.0 – 1.5	9.7	6.9	7.3	5.3	9.9	6.8	6.6	8.3	8.9	8.6	5.6	4.8	6.9	10.2	5.6	5.8	7.3	4.6	5.9	6.1	13.2	7.6	9.9	10.7	6.6	5.8	7.6
Near Normal	-1.0 – 1.0	68.0	66.3	62.2	70.0	62.5	62.9	74.3	67.5	71.3	74.1	74.9	71.9	66.0	65.8	69.8	70.0	73.3	69.1	70.1	75.2	63.9	67.8	66.8	68.5	72.8	67.5	69.8
Moderately Dry	-1.5 – -1.0	9.6	11.4	13.0	11.1	10.1	10.9	10.1	6.9	6.4	10.9	7.6	14.4	10.9	10.7	11.6	12.7	7.6	13.7	10.4	10.4	9.6	10.9	12.4	6.1	11.7	12.9	10.4
Severely Dry	-2.0 – -1.5	5.1	5.3	6.1	5.4	4.6	7.4	3.8	4.1	4.5	2.8	5.8	5.0	6.1	5.1	4.3	5.6	4.1	8.1	5.4	3.5	4.0	5.8	4.6	4.8	4.3	6.1	4.5
Extremely Dry	< -2.0	1.7	4.3	4.1	3.3	4.8	5.8	1.7	3.3	1.7	0.0	2.3	2.5	3.5	1.7	2.6	4.1	1.0	3.6	4.0	1.0	1.8	2.6	2.8	4.0	0.7	2.1	2.6
	Total %	100	100	100	100	100	100	100	100	100	100	100	100	100	100	100	100	100	100	100	100	100	100	100	100	100	100	100

		Menorca	Molina di Aragon	Moron de la Frontera	Murcia	Murcia-San Javier	Oreense	Oviedo	Palma de Mallorca	Pamplona-Noain	Ponferrada	Pontevedra	Reus Airp.	Salamanca	San Sebastian-Igueldo	Santander	Santiado de Compostela	Segovia	Sevilla	Soria	Tarifa	Toledo	Valencia Viveros	Valladolid	Vigo-Peinador	Vitoria	Zamora	Zaragoza
Extremely Wet	> 2.0	0.2	0.3	1.3	1.5	1.3	1.7	4.3	3.5	1.2	1.8	1.5	1.0	1.2	2.5	1.2	1.8	1.2	1.5	2.0	0.0	1.3	3.0	1.0	1.8	1.7	0.7	1.8
Very Wet	1.5 – 2.0	2.6	2.3	2.6	5.3	5.9	4.3	5.8	5.3	1.7	5.3	3.3	3.3	1.8	4.3	3.3	2.6	3.6	2.1	3.5	1.3	3.6	4.1	3.0	2.6	2.3	4.0	3.8
Moderately Wet	1.0 – 1.5	8.3	5.6	7.4	8.3	9.9	10.4	9.1	10.4	5.3	10.7	9.2	4.1	6.4	7.9	8.4	8.7	8.3	6.8	8.3	10.2	8.1	11.1	7.8	9.2	9.1	8.1	7.3
Near Normal	-1.0 – 1.0	70.0	68.3	70.3	67.5	65.8	70.0	63.9	70.6	74.4	68.3	68.0	72.6	77.1	70.3	65.7	67.7	68.0	67.8	69.0	71.9	65.3	68.3	69.3	65.5	66.2	77.2	72.4
Moderately Dry	-1.5 – -1.0	10.4	12.4	11.4	12.4	10.1	10.1	9.6	6.1	9.1	7.9	10.4	10.9	7.3	8.4	10.6	11.1	10.2	12.5	10.4	10.6	12.7	7.4	10.6	11.4	10.1	8.1	9.6
Severely Dry	-2.0 – -1.5	6.4	5.8	4.5	4.3	4.6	2.3	5.8	3.5	4.1	4.3	4.6	5.1	4.0	5.0	7.9	5.1	5.3	6.4	3.1	4.8	6.1	3.8	4.3	5.3	5.9	1.8	4.3
Extremely Dry	< -2.0	2.1	5.3	2.5	0.8	2.3	1.3	1.7	0.7	4.3	1.7	3.0	3.0	2.3	1.7	3.0	3.0	3.5	2.8	3.8	1.2	2.8	2.3	4.1	4.1	4.8	0.2	0.8
	Total %	100	100	100	100	100	100	100	100	100	100	100	100	100	100	100	100	100	100	100	100	100	100	100	100	100	100	100

Table 6. Percentage Classification Values of Drought Based on 9-Month SPI Index Results (%)

		Albacete	Almeria	Asturias	Badajoz Airp.	Barcelona	Bilbao	Burgos	Caceres	Castellon-Alamazora	Ciudad	Cordoba	Cuenca	Gijon	Girona	Granada	Guadalajara	Huelva	Huesca	Ibiza	Jerez de la Frontera	La Coruna	Leon-Virgen del Camino	Lleida	Logrono-Agoncillo	Madrid	Malaga	Melilla
Extremely Wet	> 2.0	2.7	3.2	3.2	2.7	0.3	1.7	0.3	5.5	1.7	1.0	0.0	0.2	1.5	2.3	2.8	0.8	4.6	0.0	1.3	1.3	2.0	2.2	0.3	1.7	1.0	2.5	2.2
Very Wet	1.5 – 2.0	5.3	1.8	1.2	2.8	6.3	1.8	1.5	6.3	5.3	3.5	3.6	1.0	3.3	4.5	3.3	1.0	4.5	0.2	2.0	2.0	4.6	3.3	2.3	4.8	2.7	2.7	2.8
Moderately Wet	1.0 – 1.5	8.8	5.1	6.8	5.6	11.9	6.8	6.6	9.6	12.6	6.6	4.5	4.1	11.3	8.6	5.8	4.6	5.8	4.0	7.1	5.8	11.9	7.5	10.9	10.9	6.8	7.1	8.1
Near Normal	-1.0 – 1.0	68.0	67.8	64.7	63.0	60.7	62.4	76.1	61.7	68.7	75.5	71.0	72.0	65.0	63.3	66.0	66.7	72.1	68.2	71.6	74.8	66.2	61.5	66.2	66.7	72.8	62.9	64.7
Moderately Dry	-1.5 – -1.0	8.6	10.4	13.4	12.8	9.1	11.9	9.5	9.8	6.8	10.9	10.9	13.1	9.5	11.4	10.3	15.8	7.6	15.6	10.9	11.3	9.0	15.1	10.8	7.6	12.6	12.4	13.8
Severely Dry	-2.0 – -1.5	4.5	7.0	6.1	8.1	6.6	9.3	4.1	4.1	2.7	2.5	6.3	6.8	5.5	8.0	7.6	6.6	3.3	6.6	4.1	4.0	4.5	6.6	7.1	4.5	3.5	8.0	5.0
Extremely Dry	< -2.0	2.2	4.6	4.6	5.0	5.0	6.1	1.8	3.0	2.3	0.0	3.6	2.8	4.0	1.8	4.1	4.5	2.0	5.5	2.8	0.8	1.8	3.8	2.3	3.8	0.7	4.5	3.5
	Total %	100	100	100	100	100	100	100	100	100	100	100	100	100	100	100	100	100	100	100	100	100	100	100	100	100	100	100

		Menorca	Molina di Aragon	Moron de la Frontera	Murcia	Murcia-San Javier	Oreense	Oviedo	Palma de Mallorca	Pamplona-Noain	Ponferrada	Pontevedra	Reus Airp.	Salamanca	San Sebastian-Igueldo	Santander	Santiado de Compostela	Segovia	Sevilla	Soria	Tarifa	Toledo	Valencia Viveros	Valladolid	Vigo-Peinador	Vitoria	Zamora	Zaragoza
Extremely Wet	> 2.0	0.0	0.2	2.3	1.3	1.2	1.7	4.6	4.3	1.3	2.0	1.0	0.0	0.5	1.7	1.2	2.0	1.8	0.5	1.8	0.0	3.0	1.5	0.5	1.7	1.5	0.8	1.5
Very Wet	1.5 – 2.0	1.8	0.8	0.7	4.6	4.3	4.8	5.8	5.6	1.8	5.0	3.5	2.3	1.3	5.0	3.0	2.2	3.8	2.8	2.7	0.7	2.8	8.5	2.5	2.3	2.8	2.8	4.1
Moderately Wet	1.0 – 1.5	9.5	6.8	6.3	7.8	11.3	9.1	9.3	9.1	3.2	9.3	9.0	6.6	6.6	9.3	7.0	6.8	5.6	6.5	10.4	5.3	5.3	8.0	7.1	8.0	4.6	8.3	7.8
Near Normal	-1.0 – 1.0	70.8	65.7	68.8	68.0	67.8	69.8	63.8	72.1	73.5	69.2	66.8	71.3	75.3	70.6	67.0	65.7	69.2	62.0	63.8	72.8	63.5	66.3	69.5	62.0	70.5	78.3	71.6
Moderately Dry	-1.5 – -1.0	8.1	11.8	12.8	11.9	9.6	10.0	10.0	5.3	10.1	8.8	10.3	11.9	9.8	8.1	11.8	13.3	10.9	16.1	11.8	12.9	14.3	10.1	10.6	14.1	9.3	6.6	9.1
Severely Dry	-2.0 – -1.5	5.8	7.5	7.0	5.1	3.8	3.8	4.1	2.3	5.6	4.1	6.1	5.0	3.8	3.2	6.1	6.1	5.1	7.3	7.0	6.8	7.0	3.6	5.8	8.0	6.3	3.2	4.1
Extremely Dry	< -2.0	4.0	7.3	2.2	1.2	2.0	0.8	2.3	1.2	4.5	1.7	3.3	2.8	2.7	2.2	4.0	4.0	3.5	4.8	2.5	1.5	4.1	2.0	4.0	4.0	5.0	0.0	1.7
	Total %	100	100	100	100	100	100	100	100	100	100	100	100	100	100	100	100	100	100	100	100	100	100	100	100	100	100	100

Table 7. Percentage classification values of drought based on 12-month SPI results (%)

		Albacete	Almeria	Asturias	Badajoz Airp.	Barcelona	Bilbao	Burgos	Caceres	Castellon-Alamaziora	Ciudad	Cordoba	Cuenca	Gijon	Girona	Granada	Guadalajara	Huelva	Huesca	Ibiza	Jerez de la Frontera	La Coruna	Leon-Virgen del Camino	Lleida	Logrono-Agoncillo	Madrid	Malaga	Melilla
Extremely Wet	> 2.0	2.0	2.5	1.7	2.7	0.2	2.5	0.2	5.8	1.2	0.8	0.0	0.0	0.7	1.8	3.7	0.8	6.0	0.0	0.2	1.8	2.2	1.8	0.2	2.2	0.3	2.0	2.7
Very Wet	1.5 – 2.0	6.0	2.7	3.3	3.2	5.8	2.2	1.0	7.0	3.8	2.2	1.2	0.7	4.2	3.5	3.2	0.8	4.8	0.0	2.8	1.7	2.3	3.8	2.0	5.7	2.7	4.8	3.8
Moderately Wet	1.0 – 1.5	9.3	5.3	6.2	4.2	10.2	4.3	4.8	12.3	14.2	8.0	7.2	3.3	9.5	8.7	6.3	3.7	7.2	1.5	4.8	2.5	12.5	6.2	7.0	11.0	5.0	6.0	6.2
Near Normal	-1.0 – 1.0	66.8	64.5	67.3	63.7	65.0	65.5	78.3	59.3	70.7	75.2	73.5	72.3	67.7	64.8	59.2	64.7	69.2	66.2	74.3	76.2	69.8	65.0	70.3	66.2	75.3	59.5	61.5
Moderately Dry	-1.5 – -1.0	12.0	12.3	12.0	10.7	8.5	11.7	9.8	8.7	4.3	10.8	9.2	12.2	8.7	11.7	13.8	18.5	9.2	15.3	10.8	12.8	7.7	10.7	13.3	6.3	11.0	14.8	15.7
Severely Dry	-2.0 – -1.5	1.8	6.2	3.7	9.3	2.7	7.2	4.5	3.7	4.5	3.0	4.2	7.8	5.5	5.3	7.3	5.5	3.0	11.8	4.5	3.7	4.7	7.2	5.3	5.3	5.2	6.3	7.2
Extremely Dry	< -2.0	2.0	6.5	5.8	6.3	7.7	6.7	1.3	3.2	1.3	0.0	4.8	3.7	3.8	4.2	6.5	6.0	0.7	5.2	2.5	1.3	0.8	5.3	1.8	3.3	0.7	6.5	3.2
	Total %	100	100	100	100	100	100	100	100	100	100	100	100	100	100	100	100	100	100	100	100	100	100	100	100	100	100	100

		Menorca	Molina di Aragon	Moron de la Frontera	Murcia	Murcia-San Javier	Oreense	Oviedo	Palma de Mallorca	Pamplona-Noain	Ponferrada	Pontevedra	Reus Airp.	Salamanca	San Sebastian-Igueldo	Santander	Santiado de Compostela	Segovia	Sevilla	Soria	Tarifa	Toledo	Valencia Viveros	Valladolid	Vigo-Peinador	Vitoria	Zamora	Zaragoza
Extremely Wet	> 2.0	0.0	0.0	0.7	1.8	2.2	1.8	5.0	5.5	1.3	2.0	2.3	0.3	0.0	3.3	1.7	1.8	2.3	0.2	1.3	0.0	1.0	1.7	0.2	2.8	0.7	0.3	0.5
Very Wet	1.5 – 2.0	0.3	0.7	3.0	2.8	3.2	3.7	4.7	5.0	1.5	3.5	0.5	0.2	1.7	3.7	3.0	1.7	2.3	1.3	2.5	0.0	3.2	6.3	2.0	1.3	2.8	1.8	5.0
Moderately Wet	1.0 – 1.5	10.2	3.2	6.2	9.3	8.0	8.7	9.8	11.5	3.7	11.0	4.8	5.7	4.2	7.5	6.0	3.8	6.5	6.8	10.0	3.7	6.7	13.2	6.0	3.0	5.0	8.7	7.8
Near Normal	-1.0 – 1.0	70.2	67.7	64.8	68.8	70.3	73.5	66.2	67.7	71.8	67.3	72.0	72.0	75.3	72.8	68.8	67.8	69.5	61.7	64.8	75.5	63.2	64.5	72.3	69.2	71.7	79.5	72.3
Moderately Dry	-1.5 – -1.0	8.7	12.7	13.8	8.2	10.5	10.2	8.2	6.5	10.3	9.2	9.5	13.5	10.2	8.7	9.7	14.0	9.7	13.7	11.3	11.8	15.2	9.5	9.7	10.5	10.2	8.2	10.5
Severely Dry	-2.0 – -1.5	6.0	9.8	9.2	7.5	3.8	1.3	4.7	3.5	7.0	5.5	6.3	5.8	5.5	2.2	5.0	6.5	5.0	8.3	6.2	6.8	6.7	3.0	5.8	5.8	6.7	1.5	3.2
Extremely Dry	< -2.0	4.7	6.0	2.3	1.5	2.0	0.8	1.5	0.3	4.3	1.5	4.5	2.5	3.2	1.8	5.8	4.3	4.7	8.0	3.8	2.2	4.2	1.8	4.0	7.3	3.0	0.0	0.7
	Total %	100	100	100	100	100	100	100	100	100	100	100	100	100	100	100	100	100	100	100	100	100	100	100	100	100	100	100

Table 8. Percentage classification values of drought based on 1-month SPEI results (%)

		Albacete	Almeria	Asturias	Badajoz Airp.	Barcelona	Bilbao	Burgos	Caceres	Castellon-Alamaziora	Ciudad	Cordoba	Cuenca	Gijon	Girona	Granada	Guadalajara	Huelva	Huesca	Ibiza	Jerez de la Frontera	La Coruna	Leon-Virgen del Camino	Lleida	Logrono-Agoncillo	Madrid	Malaga	Melilla
Extremely Wet	> 2.0	1.5	1.1	1.3	2.1	2.9	2.1	1.5	3.1	2.3	1.5	2.1	1.8	1.3	2.5	1.6	0.5	2.0	1.5	2.1	1.1	1.5	1.6	1.8	1.3	1.8	2.3	2.0
Very Wet	1.5 – 2.0	3.4	3.6	5.2	2.9	3.9	4.9	4.4	3.1	4.9	3.3	2.5	2.5	5.7	3.9	2.6	4.1	4.4	3.8	4.4	4.7	7.0	3.8	4.9	4.9	3.6	3.3	5.2
Moderately Wet	1.0 – 1.5	9.5	7.2	12.9	7.9	7.9	10.8	9.7	11.5	8.5	7.9	7.0	9.3	10.8	9.5	9.3	8.8	8.2	7.0	7.4	7.4	10.1	9.2	9.3	8.2	7.7	8.7	9.0
Near Normal	-1.0 – 1.0	62.4	64.0	61.0	62.5	66.0	61.5	64.8	60.1	64.6	63.8	65.0	65.1	61.2	66.1	62.2	65.0	63.2	65.1	64.6	65.0	60.2	64.5	61.2	63.8	63.0	63.2	61.4
Moderately Dry	-1.5 – -1.0	12.9	14.2	14.2	16.4	9.0	12.6	10.8	14.7	9.8	14.4	15.5	9.7	16.4	9.2	15.4	12.9	16.7	11.3	11.3	13.9	14.1	11.8	13.9	12.1	14.1	15.2	17.3
Severely Dry	-2.0 – -1.5	10.3	9.8	5.1	8.2	9.2	7.5	8.2	7.4	7.7	9.0	7.9	11.5	3.9	7.5	8.8	8.7	5.6	11.3	10.1	7.9	7.0	9.0	8.8	9.7	9.5	7.2	4.9
Extremely Dry	< -2.0	0.0	0.0	0.2	0.0	1.1	0.5	0.7	0.2	2.1	0.2	0.0	0.2	0.7	1.3	0.0	0.0	0.0	0.0	0.0	0.0	0.0	0.2	0.0	0.0	0.3	0.2	0.2
	Total %	100	100	100	100	100	100	100	100	100	100	100	100	100	100	100	100	100	100	100	100	100	100	100	100	100	100	100

		Menorca	Molina di Aragon	Moron de la Frontera	Murcia	Murcia-San Javier	Oreense	Oviedo	Palma de Mallorca	Pamplona-Noain	Ponferrada	Pontevedra	Reus Airp.	Salamanca	San Sebastian-Igueldo	Santander	Santiado de Compostela	Segovia	Sevilla	Soria	Tarifa	Toledo	Valencia Viveros	Valladolid	Vigo-Peinador	Vitoria	Zamora	Zaragoza
Extremely Wet	> 2.0	1.1	0.8	1.8	2.1	2.3	1.3	1.5	2.6	1.0	1.8	1.3	2.3	1.1	2.1	2.0	1.3	1.1	1.8	1.5	1.3	1.1	2.6	1.8	1.6	2.0	1.8	1.1
Very Wet	1.5 – 2.0	3.8	3.1	3.9	2.9	3.3	6.2	5.1	3.4	4.4	4.7	6.7	4.1	3.4	6.2	6.4	5.6	3.3	3.1	3.8	3.1	3.8	4.6	2.9	5.7	4.7	4.1	3.6
Moderately Wet	1.0 – 1.5	9.5	10.0	7.7	6.7	7.4	9.0	11.6	9.3	10.1	9.2	10.6	7.9	9.3	10.8	8.3	10.8	11.1	8.3	9.0	11.3	7.0	6.5	7.2	10.8	11.1	7.9	8.2
Near Normal	-1.0 – 1.0	63.5	65.0	63.0	66.4	64.5	62.0	62.2	62.7	66.4	63.8	62.4	65.1	63.2	64.0	60.4	62.5	61.5	63.8	64.6	64.5	63.5	64.0	63.5	62.4	60.6	63.0	63.0
Moderately Dry	-1.5 – -1.0	12.3	11.3	16.5	10.5	13.9	14.9	13.9	12.4	10.3	12.6	14.7	10.1	13.6	10.5	17.2	13.6	13.1	14.2	11.1	17.2	14.6	11.1	12.9	14.1	13.3	12.9	13.6
Severely Dry	-2.0 – -1.5	9.8	9.7	6.9	11.1	8.7	6.5	5.4	9.5	7.5	7.7	4.3	10.1	9.3	5.2	5.4	6.2	9.8	8.7	9.8	2.6	9.8	10.8	11.6	5.4	8.2	10.1	10.5
Extremely Dry	< -2.0	0.0	0.2	0.2	0.2	0.0	0.0	0.3	0.0	0.2	0.2	0.0	0.3	0.0	1.1	0.3	0.0	0.0	0.0	0.2	0.0	0.2	0.3	0.0	0.0	0.2	0.2	0.0
	Total %	100	100	100	100	100	100	100	100	100	100	100	100	100	100	100	100	100	100	100	100	100	100	100	100	100	100	100

Table 9. Percentage classification values of drought based on 3-month SPEI results (%)%)

		Albacete	Almeria	Asturias	Badajoz Airp.	Barcelona	Bilbao	Burgos	Caceres	Castellon-Alamaziora	Ciudad	Cordoba	Cuenca	Gijon	Girona	Granada	Guadalajara	Huelva	Huesca	Ibiza	Jerez de la Frontera	La Coruna	Leon-Virgen del Camino	Lleida	Logrono-Agoncillo	Madrid	Malaga	Melilla
Extremely Wet	> 2.0	0.7	0.3	1.6	1.1	1.6	1.5	1.0	1.8	1.5	0.8	1.3	0.7	1.6	1.8	1.1	0.3	1.8	0.8	0.7	1.5	1.1	1.5	0.8	0.5	0.8	1.6	1.1
Very Wet	1.5 – 2.0	2.0	2.5	5.1	3.3	3.9	4.8	3.6	6.6	4.9	3.3	3.3	3.0	5.9	3.8	2.5	3.0	5.3	2.6	4.1	2.8	7.4	3.8	3.1	3.3	3.6	2.8	4.1
Moderately Wet	1.0 – 1.5	10.8	13.0	10.2	9.0	10.2	11.0	9.5	7.4	10.3	8.7	5.7	10.7	10.2	10.2	11.3	9.5	8.9	8.9	11.7	9.2	12.0	8.2	13.3	13.6	8.5	8.7	12.3
Near Normal	-1.0 – 1.0	62.1	56.8	62.4	61.2	60.1	59.4	63.4	60.0	61.6	62.6	65.0	60.8	59.9	64.2	59.4	63.7	60.4	62.9	59.8	62.4	58.6	64.5	58.6	58.3	62.9	62.9	59.0
Moderately Dry	-1.5 – -1.0	14.3	19.4	14.6	16.9	13.5	13.6	13.6	15.9	13.1	14.0	16.7	16.6	15.9	12.6	18.4	15.6	17.7	13.1	15.6	18.1	13.1	14.3	14.6	16.6	14.8	16.9	19.2
Severely Dry	-2.0 – -1.5	10.2	8.0	5.1	8.4	10.2	9.5	8.2	7.4	8.0	10.2	7.9	8.2	6.4	7.1	7.2	7.9	5.9	11.7	8.2	6.1	7.1	7.7	9.4	7.6	8.9	7.1	3.9
Extremely Dry	< -2.0	0.0	0.0	1.0	0.0	0.5	0.2	0.7	0.0	0.5	0.2	0.0	0.2	0.0	0.3	0.0	0.0	0.0	0.0	0.0	0.0	0.7	0.0	0.2	0.2	0.5	0.0	0.0
	Total %	100	100	100	100	100	100	100	100	100	100	100	100	100	100	100	100	100	100	100	100	100	100	100	100	100	100	100

		Menorca	Molina di Aragon	Moron de la Frontera	Murcia	Murcia-San Javier	Oreense	Oviedo	Palma de Mallorca	Pamplona-Noain	Ponferrada	Pontevedra	Reus Airp.	Salamanca	San Sebastian-Igueldo	Santander	Santiado de Compostela	Segovia	Sevilla	Soria	Tarifa	Toledo	Valencia Viveros	Valladolid	Vigo-Peinador	Vitoria	Zamora	Zaragoza
Extremely Wet	> 2.0	0.0	0.5	1.3	1.0	1.3	1.5	1.3	1.1	0.5	2.0	1.0	1.8	0.5	1.8	0.7	1.3	0.3	1.3	0.8	0.5	0.5	1.8	0.5	1.3	1.0	0.5	0.3
Very Wet	1.5 – 2.0	3.3	2.5	3.8	2.1	4.8	4.1	4.6	3.6	4.3	3.4	6.1	3.0	2.3	5.9	6.9	5.6	3.8	3.4	3.6	3.4	3.3	3.4	3.6	6.7	4.8	3.4	2.3
Moderately Wet	1.0 – 1.5	13.1	11.2	9.5	11.8	9.0	11.7	12.2	11.7	10.7	12.5	12.3	9.7	13.0	10.2	10.0	10.8	12.5	8.0	9.5	12.3	10.3	10.3	8.2	9.4	13.0	10.5	12.8
Near Normal	-1.0 – 1.0	58.6	61.7	61.4	58.5	60.1	60.6	61.7	59.4	64.7	59.4	60.1	62.4	60.8	60.9	60.4	61.9	58.8	62.9	61.9	59.9	61.6	59.9	61.1	61.9	57.0	62.4	59.4
Moderately Dry	-1.5 – -1.0	17.4	14.3	17.1	16.1	16.1	15.6	13.5	15.1	12.0	16.3	13.8	13.3	15.6	13.8	13.6	13.6	15.6	16.4	16.1	21.5	13.6	14.3	15.6	14.3	16.4	13.8	16.4
Severely Dry	-2.0 – -1.5	7.6	9.9	6.9	10.5	8.7	6.6	6.7	9.0	7.6	6.4	6.7	9.9	7.9	6.2	8.2	6.7	9.0	7.9	7.7	2.3	10.5	10.2	11.0	6.4	7.7	9.4	8.7
Extremely Dry	< -2.0	0.0	0.0	0.0	0.0	0.0	0.0	0.0	0.0	0.3	0.0	0.0	0.0	0.0	1.1	0.2	0.0	0.0	0.0	0.3	0.0	0.2	0.0	0.0	0.0	0.2	0.0	0.0
	Total %	100	100	100	100	100	100	100	100	100	100	100	100	100	100	100	100	100	100	100	100	100	100	100	100	100	100	100

Table 10. Percentage classification values of drought based on 6-month SPEI results (%)%)

		Albacete	Almeria	Asturias	Badajoz Airp.	Barcelona	Bilbao	Burgos	Caceres	Castellon-Alamazora	Ciudad	Cordoba	Cuenca	Gijon	Girona	Granada	Guadalajara	Huelva	Huesca	Ibiza	Jerez de la Frontera	La Coruna	Leon-Virgen del Camino	Lleida	Logrono-Agoncillo	Madrid	Malaga	Melilla
Extremely Wet	> 2.0	0.5	0.2	1.8	0.5	0.7	1.0	0.2	0.7	0.8	0.2	0.2	0.2	0.8	1.7	0.3	0.5	1.3	0.0	0.5	0.3	1.7	0.7	0.3	0.2	0.3	1.2	1.2
Very Wet	1.5 – 2.0	2.5	2.0	4.3	3.1	4.3	3.5	3.1	6.8	4.6	2.5	2.5	2.0	4.0	4.3	3.5	1.8	5.0	2.0	3.5	3.6	4.8	4.6	3.0	3.5	2.3	4.6	3.0
Moderately Wet	1.0 – 1.5	14.9	14.5	11.4	13.9	13.0	13.2	11.2	13.0	13.0	12.0	12.0	13.5	13.2	11.1	13.5	15.2	12.2	12.2	14.5	13.2	14.7	12.2	15.3	14.7	12.4	7.9	12.7
Near Normal	-1.0 – 1.0	54.6	50.3	61.4	57.1	57.6	57.9	63.5	59.2	59.2	60.1	59.9	59.7	59.1	63.0	56.8	59.4	57.4	59.1	58.1	60.1	58.4	61.1	59.7	56.3	58.1	61.6	59.6
Moderately Dry	-1.5 – -1.0	21.6	29.5	15.8	21.6	14.5	17.2	14.4	15.8	15.5	17.7	21.5	20.0	15.8	12.5	22.3	17.5	20.0	19.0	20.1	19.8	13.7	16.7	15.2	20.1	18.6	19.3	20.0
Severely Dry	-2.0 – -1.5	5.9	3.5	4.0	3.5	8.9	6.8	7.4	4.0	6.3	7.4	3.8	4.5	6.4	6.9	3.5	5.6	4.0	6.9	3.1	2.8	6.3	4.6	6.3	5.0	7.9	4.8	3.3
Extremely Dry	< -2.0	0.0	0.0	1.3	0.3	1.0	0.5	0.2	0.5	0.5	0.2	0.2	0.2	0.7	0.5	0.2	0.0	0.2	0.8	0.2	0.2	0.5	0.2	0.2	0.3	0.3	0.7	0.3
	Total %	100	100	100	100	100	100	100	100	100	100	100	100	100	100	100	100	100	100	100	100	100	100	100	100	100	100	100

		Menorca	Molina di Aragon	Moron de la Frontera	Murcia	Murcia-San Javier	Oreense	Oviedo	Palma de Mallorca	Pamplona-Noain	Ponferrada	Pontevedra	Reus Airp.	Salamanca	San Sebastian-Igueldo	Santander	Santiado de Compostela	Segovia	Sevilla	Soria	Tarifa	Toledo	Valencia Viveros	Valladolid	Vigo-Peinador	Vitoria	Zamora	Zaragoza
Extremely Wet	> 2.0	0.0	0.2	0.3	0.0	0.5	1.0	0.5	0.7	1.0	1.3	1.5	0.7	0.3	1.8	0.5	1.8	0.8	0.2	0.2	0.0	0.3	1.2	0.0	1.7	0.2	0.0	0.2
Very Wet	1.5 – 2.0	2.5	2.3	3.5	2.1	5.8	4.6	6.1	4.5	2.0	4.1	4.1	4.0	2.5	4.8	5.1	3.5	3.1	3.5	3.8	3.5	3.0	4.0	2.3	4.3	4.3	3.5	1.8
Moderately Wet	1.0 – 1.5	15.5	13.7	14.9	15.5	11.6	14.2	12.2	14.7	10.6	14.0	15.0	11.1	15.5	9.4	12.4	12.2	13.4	12.5	13.0	12.9	11.1	12.2	13.0	14.2	14.7	14.2	15.7
Near Normal	-1.0 – 1.0	56.9	61.7	58.7	53.5	56.4	58.7	60.6	56.4	65.7	59.6	61.4	59.1	56.3	64.4	57.6	61.9	57.1	57.3	58.7	65.3	57.8	55.4	53.8	60.7	55.1	56.1	54.1
Moderately Dry	-1.5 – -1.0	20.0	13.9	17.8	22.4	19.6	18.3	17.3	19.8	14.0	17.0	13.2	19.0	22.6	12.0	17.0	15.0	20.8	22.1	19.3	16.2	19.3	20.5	24.4	14.4	20.8	22.4	23.6
Severely Dry	-2.0 – -1.5	5.1	7.8	4.5	6.3	5.6	2.8	2.6	3.6	5.8	3.8	4.3	5.9	2.6	6.1	6.8	4.6	4.0	4.3	4.1	2.1	8.3	6.3	5.8	4.0	4.6	3.8	4.3
Extremely Dry	< -2.0	0.0	0.5	0.3	0.2	0.5	0.3	0.7	0.3	1.0	0.2	0.5	0.3	0.2	1.5	0.7	1.0	0.8	0.2	0.8	0.0	0.3	0.5	0.7	0.8	0.3	0.0	0.3
	Total %	100	100	100	100	100	100	100	100	100	100	100	100	100	100	100	100	100	100	100	100	100	100	100	100	100	100	100

Table 11. Percentage classification values of drought based on 9-month SPEI results (%)

		Albacete	Almeria	Asturias	Badajoz Airp.	Barcelona	Bilbao	Burgos	Caceres	Castellon-Alamazora	Ciudad	Cordoba	Cuenca	Gijon	Girona	Granada	Guadalajara	Huelva	Huesca	Ibiza	Jerez de la Frontera	La Coruna	Leon-Virgen del Camino	Lleida	Logrono-Agoncillo	Madrid	Malaga	Melilla
Extremely Wet	> 2.0	0.7	0.3	1.5	0.2	1.2	1.2	0.0	1.0	1.3	0.3	0.0	0.0	0.7	2.0	0.3	0.8	0.7	0.2	0.5	0.7	1.5	1.8	1.3	0.5	0.5	1.3	2.2
Very Wet	1.5 – 2.0	4.6	2.8	4.3	5.8	4.5	3.0	3.0	9.1	4.8	3.8	4.1	3.8	3.2	5.3	4.8	4.1	7.0	2.2	5.1	3.6	6.1	5.1	4.1	7.0	2.8	5.0	2.2
Moderately Wet	1.0 – 1.5	11.8	11.9	10.0	11.3	10.0	10.9	8.6	10.4	10.4	8.0	10.4	11.1	12.9	7.8	12.3	11.3	11.4	10.6	13.3	11.1	10.4	9.5	10.0	11.4	9.6	7.0	12.8
Near Normal	-1.0 – 1.0	59.7	60.2	65.5	60.2	61.2	60.2	67.2	61.9	67.2	65.2	63.5	64.2	63.7	67.2	60.9	63.8	60.5	64.7	62.0	64.8	62.2	63.3	66.5	60.4	61.9	65.3	64.1
Moderately Dry	-1.5 – -1.0	15.6	17.2	12.1	16.1	13.9	14.4	14.3	10.1	8.0	13.6	15.9	14.1	14.1	10.4	14.9	12.6	13.1	13.4	13.1	14.1	11.9	13.6	10.8	12.8	14.9	12.8	11.9
Severely Dry	-2.0 – -1.5	8.0	7.0	5.0	5.8	7.1	8.8	5.8	6.3	6.3	7.5	5.3	5.6	6.3	6.1	5.5	5.8	6.3	7.0	5.1	5.1	6.1	5.6	6.0	7.0	8.8	6.8	5.8
Extremely Dry	< -2.0	0.7	0.5	1.7	0.7	2.2	1.5	1.2	1.2	2.0	1.7	0.7	1.2	1.2	1.2	1.2	1.5	1.0	2.0	0.8	0.5	1.7	1.0	1.3	1.0	1.5	1.8	0.8
	Total %	100	100	100	100	100	100	100	100	100	100	100	100	100	100	100	100	100	100	100	100	100	100	100	100	100	100	100

		Menorca	Molina di Aragon	Moron de la Frontera	Murcia	Murcia-San Javier	Oreense	Oviedo	Palma de Mallorca	Pamplona-Noain	Ponferada	Pontevedra	Reus Airp.	Salamanca	San Sebastian-Igueldo	Santander	Santiado de Compostela	Segovia	Sevilla	Soria	Tarifa	Toledo	Valencia Viveros	Valladolid	Vigo-Peinador	Vitoria	Zamora	Zaragoza
Extremely Wet	> 2.0	0.5	0.5	0.0	0.0	1.0	1.3	1.0	0.8	1.2	2.3	2.2	0.5	0.2	1.7	1.0	2.2	0.8	0.3	0.0	0.0	0.7	0.5	0.0	2.3	1.2	0.3	0.5
Very Wet	1.5 – 2.0	3.5	3.5	5.0	4.8	5.3	5.6	4.6	6.1	3.0	4.5	4.3	3.3	5.0	4.8	3.8	3.0	5.1	5.0	6.0	2.3	4.6	5.8	4.8	4.5	4.5	4.8	4.0
Moderately Wet	1.0 – 1.5	12.3	10.6	11.8	11.3	10.3	10.6	12.8	11.8	6.6	10.3	11.3	10.6	13.9	10.1	9.5	10.1	10.4	10.0	11.1	11.6	8.0	9.0	10.1	10.8	10.3	11.6	13.8
Near Normal	-1.0 – 1.0	63.5	66.7	62.9	60.4	62.9	64.0	63.5	62.5	70.3	65.5	64.5	64.7	60.5	64.2	61.0	65.3	62.9	61.9	62.9	69.7	61.7	60.9	60.5	63.0	63.8	61.7	59.7
Moderately Dry	-1.5 – -1.0	12.6	10.0	13.3	13.9	12.4	12.6	11.4	12.6	11.8	11.1	11.6	12.4	14.6	12.8	15.1	11.4	13.6	14.4	12.6	12.4	14.9	14.8	15.6	12.3	11.6	14.8	14.9
Severely Dry	-2.0 – -1.5	6.6	7.3	6.3	8.5	6.1	4.1	6.1	4.6	5.6	5.1	4.5	7.1	5.1	3.6	8.5	6.5	4.6	8.1	5.3	3.6	7.3	8.3	6.8	6.0	7.5	6.0	5.6
Extremely Dry	< -2.0	1.0	1.5	0.8	1.2	2.0	1.7	0.5	1.5	1.5	1.2	1.7	1.3	0.7	2.8	1.2	1.5	2.5	0.3	2.2	0.3	2.8	0.8	2.2	1.2	1.2	0.8	1.5
	Total %	100	100	100	100	100	100	100	100	100	100	100	100	100	100	100	100	100	100	100	100	100	100	100	100	100	100	100

Table 12. Percentage classification values of drought based on 12-month SPEI results (%)

		Albacete	Almeria	Asturias	Badajoz Airp.	Barcelona	Bilbao	Burgos	Caceres	Castellon-Alamazora	Ciudad	Cordoba	Cuenca	Gijon	Girona	Granada	Guadalajara	Huelva	Huesca	Ibiza	Jerez de la Frontera	La Coruna	Leon-Virgen del Camino	Lleida	Logrono-Agoncillo	Madrid	Malaga	Melilla
Extremely Wet	> 2.0	0.7	0.0	1.3	0.3	0.5	1.2	0.0	1.8	1.7	0.0	0.0	0.0	0.2	1.7	0.2	0.7	2.0	0.0	0.5	1.8	1.7	1.8	0.3	1.5	0.3	0.7	2.7
Very Wet	1.5 – 2.0	3.8	2.3	4.8	4.8	5.8	4.2	2.0	6.7	3.5	0.8	3.2	2.2	5.0	5.5	6.5	3.5	4.5	1.8	5.5	1.5	3.7	5.8	3.5	4.3	2.2	7.2	2.5
Moderately Wet	1.0 – 1.5	11.8	5.0	10.7	8.8	7.2	7.0	4.5	14.3	8.8	8.0	7.5	6.0	7.8	10.5	6.5	6.8	12.0	3.5	9.0	6.8	10.0	6.8	10.7	8.3	5.8	6.2	7.7
Near Normal	-1.0 – 1.0	59.0	68.2	63.3	61.0	66.0	62.3	74.0	58.7	70.3	66.5	67.3	70.5	67.0	66.7	62.5	68.8	59.7	73.2	67.5	70.7	64.7	63.3	69.3	64.3	65.2	64.0	72.7
Moderately Dry	-1.5 – -1.0	15.8	15.5	13.7	15.3	9.8	14.8	13.3	10.5	7.8	17.3	14.7	12.8	11.0	9.8	14.8	10.7	15.5	12.0	9.7	12.8	12.0	14.3	10.3	11.5	14.5	11.3	8.7
Severely Dry	-2.0 – -1.5	7.7	6.8	3.8	9.0	5.2	8.3	3.8	7.3	5.2	6.7	5.8	6.8	6.2	4.0	7.3	7.0	5.8	5.7	6.8	5.2	6.8	6.7	4.5	7.8	9.3	5.3	3.3
Extremely Dry	< -2.0	1.2	2.2	2.3	0.7	5.5	2.2	2.3	0.7	2.7	0.7	1.5	1.7	2.8	1.8	2.2	2.5	0.5	3.8	1.0	1.2	1.2	1.2	1.3	2.2	2.7	5.3	2.5
	Total %	100	100	100	100	100	100	100	100	100	100	100	100	100	100	100	100	100	100	100	100	100	100	100	100	100	100	100

		Menorca	Molina di Aragon	Moron de la Frontera	Murcia	Murcia-San Javier	Oreense	Oviedo	Palma de Mallorca	Pamplona-Noain	Ponferada	Pontevedra	Reus Airp.	Salamanca	San Sebastian-Igueldo	Santander	Santiado de Compostela	Segovia	Sevilla	Soria	Tarifa	Toledo	Valencia Viveros	Valladolid	Vigo-Peinador	Vitoria	Zamora	Zaragoza
Extremely Wet	> 2.0	0.0	0.7	0.0	0.3	0.5	2.2	1.7	0.5	0.3	2.7	2.2	0.7	0.8	2.2	0.7	2.3	2.3	0.0	0.3	0.0	0.7	0.5	0.0	3.0	0.7	0.0	0.2
Very Wet	1.5 – 2.0	2.8	2.2	3.7	2.2	6.5	3.5	5.3	6.3	3.3	5.7	2.7	2.2	3.8	4.3	4.8	3.2	2.7	2.7	4.0	2.2	4.0	3.3	1.0	2.8	4.7	3.0	3.3
Moderately Wet	1.0 – 1.5	10.3	7.3	7.7	7.5	8.7	9.3	10.2	9.7	8.5	8.3	8.3	7.7	8.8	8.2	8.3	5.0	6.7	9.3	8.0	8.0	6.2	9.8	5.7	8.7	10.0	9.3	8.2
Near Normal	-1.0 – 1.0	65.2	68.7	66.8	63.3	60.7	64.3	66.8	67.0	67.8	69.0	71.5	70.3	67.3	67.3	61.7	68.3	69.7	64.0	65.0	77.9	60.7	60.5	66.2	66.2	65.2	65.5	67.2
Moderately Dry	-1.5 – -1.0	12.8	11.0	11.2	15.5	15.0	16.0	9.3	8.5	11.7	6.8	7.7	10.3	11.3	11.7	14.8	12.5	11.3	12.5	14.7	9.0	15.3	16.3	17.5	11.3	9.8	15.0	14.0
Severely Dry	-2.0 – -1.5	8.2	9.8	9.3	9.2	6.8	3.5	5.5	5.8	7.2	4.7	6.3	7.0	6.3	4.3	8.0	6.8	3.0	11.2	5.0	3.3	10.3	7.2	7.0	5.7	8.0	6.5	5.0
Extremely Dry	< -2.0	0.7	0.8	1.3	2.0	1.8	1.2	1.2	2.2	1.2	2.8	1.3	1.8	1.5	2.0	1.7	1.8	4.3	0.3	3.0	0.5	2.8	2.3	2.7	2.3	1.7	0.7	2.2
	Total %	100	100	100	100	100	100	100	100	100	100	100	100	100	100	100	100	100	100	100	100	100	100	100	100	100	100	100

Table 13. Percentage classification values of drought based on 1-month RDI results (%)

		Albacete	Almeria	Asturias	Badajoz Airp.	Barcelona	Bilbao	Burgos	Caceres	Castellon-Alamazora	Ciudad	Cordoba	Cuenca	Gijon	Girona	Granada	Guadalajara	Huelva	Huesca	Ibiza	Jerez de la Frontera	La Coruna	Leon-Virgen del Camino	Lleida	Logrono-Agoncillo	Madrid	Malaga	Melilla
Extremely Wet	> 2.0	1.3	2.3	5.4	2.0	3.3	2.3	1.8	2.6	2.6	1.6	2.0	1.6	2.5	1.8	1.6	1.5	2.6	1.8	1.8	1.1	1.3	1.0	2.0	2.0	1.8	1.1	2.0
Very Wet	1.5 – 2.0	3.1	4.1	2.3	2.8	2.8	6.1	2.3	3.3	3.3	3.6	6.9	2.0	3.1	5.4	3.4	3.3	3.6	2.9	6.1	6.5	3.8	3.3	7.9	3.8	3.1	4.3	3.9
Moderately Wet	1.0 – 1.5	9.7	7.7	8.0	9.0	8.3	4.4	8.7	9.8	9.8	8.0	3.6	7.0	8.5	10.1	8.3	9.3	9.7	6.1	8.5	9.0	10.0	7.2	7.9	8.5	8.2	6.2	9.8
Near Normal	-1.0 – 1.0	71.4	73.3	70.7	72.3	70.0	73.8	67.9	70.7	70.7	74.8	78.9	72.7	71.4	66.6	71.4	70.0	73.5	73.2	68.4	75.5	69.4	73.8	63.2	68.4	72.7	80.5	66.8
Moderately Dry	-1.5 – -1.0	9.0	8.0	9.0	8.0	9.7	8.7	7.7	7.7	7.7	8.7	5.1	9.7	8.0	8.0	7.9	14.4	5.2	11.0	9.3	7.9	7.9	9.5	13.3	10.8	8.5	5.2	11.8
Severely Dry	-2.0 – -1.5	5.1	4.6	2.6	5.2	4.4	2.6	11.5	4.1	4.1	3.3	0.3	5.4	4.6	5.9	6.5	1.5	3.6	4.3	3.9	0.0	4.9	4.7	3.9	5.4	4.7	2.6	5.9
Extremely Dry	< -2.0	0.5	0.0	2.0	0.7	1.5	2.1	0.2	1.8	1.8	0.0	3.3	1.6	2.0	2.1	0.8	0.0	1.8	0.8	2.0	0.0	2.8	0.5	2.0	1.1	1.0	0.0	0.6
	Total %	100	100	100	100	100	100	100	100	100	100	100	100	100	100	100	100	100	100	100	100	100	100	100	100	100	100	100

		Menorca	Molina di Aragon	Moron de la Frontera	Murcia	Murcia-San Javier	Oreense	Oviedo	Palma de Mallorca	Pamplona-Noain	Ponferrada	Pontevedra	Reus Airp.	Salamanca	San Sebastian-Igueldo	Santander	Santiado de Compostela	Segovia	Sevilla	Soria	Tarifa	Toledo	Valencia Viveros	Valladolid	Vigo-Peinador	Vitoria	Zamora	Zaragoza
Extremely Wet	> 2.0	1.8	1.1	1.3	2.9	3.4	1.6	2.8	2.9	0.0	2.3	1.1	1.5	1.0	6.1	3.1	1.5	2.1	1.8	2.8	1.3	1.8	3.3	2.5	0.7	3.4	1.1	2.1
Very Wet	1.5 – 2.0	3.9	3.3	3.8	4.4	3.8	3.9	4.1	4.1	2.0	3.9	4.4	4.1	5.1	5.4	2.5	2.8	1.8	3.9	1.6	2.5	3.3	4.7	3.1	4.4	3.4	3.4	4.7
Moderately Wet	1.0 – 1.5	11.6	9.3	7.5	9.2	7.4	7.4	9.0	8.0	7.9	10.6	11.0	11.3	7.7	3.1	9.2	8.3	6.4	7.4	7.7	6.7	8.0	10.6	5.6	8.0	8.7	10.8	8.2
Near Normal	-1.0 – 1.0	69.9	72.7	74.6	68.1	74.1	70.7	68.7	71.8	78.4	66.0	68.2	65.5	70.2	66.6	68.6	69.7	75.3	74.6	73.5	77.3	72.2	65.0	69.9	67.9	68.1	71.5	67.9
Moderately Dry	-1.5 – -1.0	6.5	8.8	6.9	12.6	8.5	9.2	9.2	9.3	3.9	10.8	8.0	12.3	9.5	15.4	9.7	10.8	8.8	6.2	8.8	6.1	8.2	11.6	10.8	12.3	9.0	8.2	10.0
Severely Dry	-2.0 – -1.5	4.7	2.1	5.7	2.5	2.6	6.4	4.3	3.4	2.0	4.1	3.8	4.3	3.3	2.3	4.3	4.4	5.6	5.6	4.7	6.2	5.6	4.3	6.7	4.6	5.4	4.1	5.6
Extremely Dry	< -2.0	1.5	3.1	0.2	0.3	0.2	0.8	2.0	0.3	5.9	2.3	3.4	1.1	3.3	1.1	2.8	2.5	0.0	0.5	0.8	0.0	1.0	0.5	1.5	2.1	2.0	0.8	1.5
	Total %	100	100	100	100	100	100	100	100	100	100	100	100	100	100	100	100	100	100	100	100	100	100	100	100	100	100	100

Table 14. Percentage classification values of drought based on 3-month RDI results (%)

		Albacete	Almeria	Asturias	Badajoz Airp.	Barcelona	Bilbao	Burgos	Caceres	Castellon-Alamazora	Ciudad	Cordoba	Cuenca	Gijon	Girona	Granada	Guadalajara	Huelva	Huesca	Ibiza	Jerez de la Frontera	La Coruna	Leon-Virgen del Camino	Lleida	Logrono-Agoncillo	Madrid	Malaga	Melilla
Extremely Wet	> 2.0	2.0	2.0	2.0	1.5	2.0	2.0	0.0	2.5	2.5	1.0	0.5	0.0	2.0	2.5	1.0	2.0	2.5	0.5	2.5	1.0	1.5	0.5	2.0	2.0	2.0	0.5	2.0
Very Wet	1.5 – 2.0	2.5	3.9	2.0	3.0	4.9	3.0	0.0	2.5	2.5	4.4	7.9	3.4	3.4	3.0	4.4	3.4	3.9	3.0	3.0	1.5	3.0	5.4	0.0	5.9	2.0	5.6	3.9
Moderately Wet	1.0 – 1.5	10.3	7.9	9.9	8.9	8.9	9.9	9.9	12.8	12.8	7.9	7.9	8.4	9.5	6.9	7.9	4.4	9.4	5.4	10.3	14.4	12.3	8.9	15.8	9.4	7.9	9.9	5.9
Near Normal	-1.0 – 1.0	67.5	64.0	76.4	67.0	64.4	63.5	76.4	67.8	67.8	73.9	69.0	70.4	68.8	69.3	68.5	73.9	73.4	71.9	64.0	64.9	63.5	67.5	65.4	63.9	73.4	67.3	71.3
Moderately Dry	-1.5 – -1.0	9.4	14.3	3.9	10.8	12.8	14.3	7.9	8.5	8.5	8.4	7.9	10.3	6.9	14.4	7.9	7.9	7.4	12.3	11.8	15.3	11.3	11.8	11.8	12.3	9.4	10.8	9.0
Severely Dry	-2.0 – -1.5	4.9	4.9	0.0	4.9	3.6	4.9	3.9	4.4	4.4	4.4	5.4	3.4	7.4	2.0	7.9	8.4	3.0	3.4	6.4	3.0	6.4	3.0	5.1	4.6	4.4	5.9	7.9
Extremely Dry	< -2.0	3.4	3.0	5.9	3.9	3.4	2.5	2.0	1.5	1.5	0.0	1.5	3.9	2.0	2.0	2.5	0.0	0.5	3.4	2.0	0.0	2.0	3.0	0.0	2.0	1.0	0.0	0.0
	Total %	100	100	100	100	100	100	100	100	100	100	100	100	100	100	100	100	100	100	100	100	100	100	100	100	100	100	100

		Menorca	Molina di Aragon	Moron de la Frontera	Murcia	Murcia-San Javier	Oreense	Oviedo	Palma de Mallorca	Pamplona-Noain	Ponferrada	Pontevedra	Reus Airp.	Salamanca	San Sebastian-Igueldo	Santander	Santiado de Compostela	Segovia	Sevilla	Soria	Tarifa	Toledo	Valencia Viveros	Valladolid	Vigo-Peinador	Vitoria	Zamora	Zaragoza
Extremely Wet	> 2.0	0.5	0.5	2.0	3.9	3.9	1.5	2.5	3.0	2.0	1.5	1.5	2.5	0.5	3.0	2.5	1.0	2.0	0.5	2.0	1.0	2.0	2.0	2.0	1.5	2.5	2.0	0.5
Very Wet	1.5 – 2.0	5.4	1.5	2.0	4.9	3.4	4.4	3.9	7.4	2.0	6.4	4.4	3.4	3.9	4.4	2.5	4.9	3.9	3.9	3.9	2.0	3.4	3.9	3.4	2.0	2.0	1.5	5.9
Moderately Wet	1.0 – 1.5	16.7	8.9	9.4	7.9	10.3	10.8	8.9	4.4	5.9	9.4	9.4	9.4	8.4	5.9	12.5	7.9	8.4	5.9	5.9	10.3	5.4	15.3	3.9	13.3	11.5	9.4	10.3
Near Normal	-1.0 – 1.0	61.9	69.5	70.6	65.5	67.0	70.4	70.0	72.4	70.4	66.5	66.8	66.8	66.0	69.5	62.4	68.5	64.0	72.4	70.4	73.4	72.4	63.5	69.0	64.0	66.3	69.5	66.3
Moderately Dry	-1.5 – -1.0	10.5	9.9	11.8	10.8	9.9	6.4	7.4	7.9	13.8	8.9	11.5	10.0	12.8	13.8	10.8	9.9	11.8	8.9	9.9	8.9	9.4	7.4	12.3	10.3	9.4	13.8	10.8
Severely Dry	-2.0 – -1.5	3.4	7.9	2.8	5.9	4.4	2.5	4.4	3.9	5.9	4.9	3.0	4.9	7.4	2.0	5.4	3.0	9.9	7.4	5.9	4.4	3.9	4.4	6.9	3.9	6.4	3.4	4.6
Extremely Dry	< -2.0	1.5	2.0	1.5	1.0	1.0	3.9	3.0	1.0	0.0	2.5	3.4	3.0	1.0	1.5	3.9	4.9	0.0	1.0	2.0	0.0	3.4	3.4	2.5	4.9	2.0	0.5	1.5
	Total %	100	100	100	100	100	100	100	100	100	100	100	100	100	100	100	100	100	100	100	100	100	100	100	100	100	100	100

Table 15. Percentage classification values of drought based on 6-month RDI results (%)

		Albacete	Almeria	Asturias	Badajoz Airp.	Barcelona	Bilbao	Burgos	Caceres	Castellon-Alamazora	Ciudad	Cordoba	Cuenca	Gijon	Girona	Granada	Guadalajara	Huelva	Huesca	Ibiza	Jerez de la Frontera	La Coruna	Leon-Virgen del Camino	Lleida	Logrono-Agoncillo	Madrid	Malaga	Melilla
Extremely Wet	> 2.0	1.0	1.0	2.0	1.0	2.0	4.0	0.0	1.0	1.0	0.0	0.0	0.0	1.0	4.0	1.0	1.0	2.0	0.0	2.0	0.0	1.0	2.0	0.0	3.0	0.0	0.0	2.0
Very Wet	1.5 – 2.0	4.0	5.0	0.0	3.0	3.0	0.0	2.0	5.0	5.0	3.0	5.9	0.0	3.0	4.0	4.0	4.0	5.0	2.0	5.0	0.0	3.0	2.0	4.0	6.9	3.0	0.0	2.0
Moderately Wet	1.0 – 1.5	8.9	3.0	11.9	6.9	9.9	5.6	11.9	11.9	11.9	5.0	5.9	10.9	6.9	9.9	5.9	8.9	11.9	6.6	5.0	15.8	11.9	9.9	9.9	5.9	8.9	13.9	9.9
Near Normal	-1.0 – 1.0	69.6	70.6	74.3	65.7	65.3	64.7	70.3	68.3	68.3	79.2	69.6	72.3	75.2	63.7	71.3	67.3	67.3	72.6	67.3	70.3	64.4	66.3	74.3	69.3	68.3	70.3	70.3
Moderately Dry	-1.5 – -1.0	10.9	11.6	4.0	13.5	12.9	17.8	7.9	4.0	4.0	11.9	10.6	9.9	5.0	16.5	8.9	9.9	10.9	9.9	11.9	9.9	8.9	11.9	5.9	6.9	13.9	5.9	7.9
Severely Dry	-2.0 – -1.5	4.6	5.0	2.0	5.0	4.0	6.9	5.9	5.9	5.9	1.0	4.0	4.0	4.0	1.0	4.0	8.9	3.0	7.9	5.9	2.0	9.9	6.9	5.9	5.0	4.0	4.0	7.9
Extremely Dry	< -2.0	1.0	4.0	5.9	5.0	3.0	1.0	2.0	4.0	4.0	0.0	4.0	3.0	5.0	1.0	5.0	0.0	0.0	1.0	3.0	2.0	1.0	1.0	0.0	3.0	2.0	5.9	0.0
	Total %	100	100	100	100	100	100	100	100	100	100	100	100	100	100	100	100	100	100	100	100	100	100	100	100	100	100	100

		Menorca	Molina di Aragon	Moron de la Frontera	Murcia	Murcia-San Javier	Oreense	Oviedo	Palma de Mallorca	Pamplona-Noain	Ponferrada	Pontevedra	Reus Airp.	Salamanca	San Sebastian-Igueldo	Santander	Santiado de Compostela	Segovia	Sevilla	Soria	Tarifa	Toledo	Valencia Viveros	Valladolid	Vigo-Peinador	Vitoria	Zamora	Zaragoza
Extremely Wet	> 2.0	1.0	1.0	0.0	2.0	4.0	3.0	3.0	3.0	0.0	4.0	2.0	0.0	1.0	0.0	1.0	2.0	2.0	0.0	2.0	1.0	1.0	2.0	0.0	2.0	2.0	1.0	0.0
Very Wet	1.5 – 2.0	4.0	3.0	2.0	3.0	4.0	5.0	5.9	5.0	2.0	5.0	3.0	5.9	5.9	9.9	2.0	5.0	6.9	2.0	5.0	2.0	2.0	7.9	4.0	4.0	4.0	3.0	5.9
Moderately Wet	1.0 – 1.5	12.9	7.9	10.9	11.9	10.9	8.9	6.9	7.9	4.0	5.9	12.9	7.9	6.9	5.9	10.6	3.0	6.9	7.9	7.9	5.9	8.9	6.9	5.9	5.9	9.6	9.9	7.9
Near Normal	-1.0 – 1.0	62.4	67.3	73.3	67.3	68.3	66.3	68.3	72.3	81.5	69.3	64.4	68.3	68.3	60.4	68.6	74.3	66.3	74.3	68.3	79.2	66.3	67.3	68.3	68.3	65.7	73.3	70.3
Moderately Dry	-1.5 – -1.0	11.9	11.9	5.9	12.9	7.9	10.9	10.9	5.0	2.6	9.9	11.9	9.9	11.9	9.9	7.9	5.9	11.9	3.0	9.9	5.9	12.9	10.9	9.9	9.9	9.9	10.9	11.9
Severely Dry	-2.0 – -1.5	5.9	5.9	3.0	3.0	3.0	5.9	5.0	6.9	5.9	5.0	5.9	7.9	2.0	9.9	5.0	7.9	5.9	9.9	4.0	5.0	5.9	2.0	9.9	8.9	5.9	2.0	4.0
Extremely Dry	< -2.0	2.0	3.0	5.0	0.0	2.0	0.0	0.0	0.0	4.0	1.0	0.0	0.0	4.0	4.0	5.0	2.0	0.0	3.0	3.0	1.0	3.0	3.0	2.0	1.0	3.0	0.0	0.0
	Total %	100	100	100	100	100	100	100	100	100	100	100	100	100	100	100	100	100	100	100	100	100	100	100	100	100	100	100

Table 16. Percentage classification values of drought based on 9-month RDI results (%)

		Albacete	Almeria	Asturias	Badajoz Airp.	Barcelona	Bilbao	Burgos	Caceres	Castellon-Alamazora	Ciudad	Cordoba	Cuenca	Gijon	Girona	Granada	Guadalajara	Huelva	Huesca	Ibiza	Jerez de la Frontera	La Coruna	Leon-Virgen del Camino	Lleida	Logrono-Agoncillo	Madrid	Malaga	Melilla
Extremely Wet	> 2.0	2.0	2.0	0.0	0.0	4.0	2.0	0.0	0.0	0.0	0.0	4.0	0.0	2.0	4.0	0.0	0.0	2.0	2.0	4.0	2.0	4.0	0.0	0.0	2.0	2.0	4.0	4.0
Very Wet	1.5 – 2.0	4.0	2.0	4.0	4.0	4.0	8.0	0.0	10.0	10.0	0.0	2.0	0.0	2.0	2.0	6.0	2.0	2.0	0.0	2.0	2.0	2.0	6.0	6.0	4.0	0.0	2.0	2.0
Moderately Wet	1.0 – 1.5	4.0	8.0	8.0	13.9	8.0	6.0	8.0	13.9	13.9	8.0	6.0	4.0	8.0	11.9	6.0	11.9	13.9	0.0	10.0	6.0	13.9	4.0	6.0	13.9	10.0	8.0	4.0
Near Normal	-1.0 – 1.0	72.0	72.1	68.2	58.2	64.2	58.2	76.1	56.2	56.2	82.1	72.1	72.1	70.1	64.0	74.1	68.2	66.2	82.1	70.1	84.1	58.2	70.1	74.1	60.2	74.1	68.2	74.1
Moderately Dry	-1.5 – -1.0	10.0	8.0	8.0	10.0	8.0	11.9	8.0	13.9	13.9	6.0	10.0	17.9	13.9	13.9	4.0	8.0	10.0	10.0	2.0	2.0	13.9	10.0	8.0	11.9	4.0	10.0	11.9
Severely Dry	-2.0 – -1.5	6.1	4.0	6.0	8.0	10.0	13.9	4.0	4.0	4.0	2.0	6.0	2.0	2.0	4.1	6.0	10.0	6.0	2.0	10.0	4.0	6.0	8.0	2.0	4.0	10.0	4.0	4.0
Extremely Dry	< -2.0	2.0	4.0	6.0	6.0	2.0	0.0	4.0	2.0	2.0	2.0	0.0	4.0	2.0	0.0	4.0	0.0	0.0	4.0	2.0	0.0	2.0	2.0	4.0	4.0	0.0	4.0	0.0
	Total %	100	100	100	100	100	100	100	100	100	100	100	100	100	100	100	100	100	100	100	100	100	100	100	100	100	100	100

		Menorca	Molina di Aragon	Moron de la Frontera	Murcia	Murcia-San Javier	Oreense	Oviedo	Palma de Mallorca	Pamplona-Noain	Ponferrada	Pontevedra	Reus Airp.	Salamanca	San Sebastian-Igueldo	Santander	Santiado de Compostela	Segovia	Sevilla	Soria	Tarifa	Toledo	Valencia Viveros	Valladolid	Vigo-Peinador	Vitoria	Zamora	Zaragoza
Extremely Wet	> 2.0	0.0	0.0	0.0	0.0	4.0	0.0	6.0	0.0	4.0	0.0	2.0	2.0	0.0	0.0	4.0	6.0	0.0	0.0	0.0	0.0	2.0	4.0	0.0	4.0	2.0	0.0	0.0
Very Wet	1.5 – 2.0	2.0	4.0	2.0	6.0	2.0	6.0	4.0	6.0	2.0	8.0	4.0	0.0	2.0	6.0	2.0	0.0	8.0	0.0	6.0	0.0	6.0	8.0	2.0	2.0	2.0	0.0	8.0
Moderately Wet	1.0 – 1.5	11.9	4.0	6.0	11.9	19.9	11.9	6.0	15.9	6.0	4.0	6.0	11.9	8.0	8.0	11.9	2.0	4.0	8.0	10.0	6.0	6.0	10.0	10.0	4.0	8.0	15.9	4.0
Near Normal	-1.0 – 1.0	64.0	68.2	78.1	68.2	60.2	66.2	70.1	68.2	72.1	72.1	74.1	70.0	72.1	70.1	62.2	72.1	70.1	70.1	66.2	82.1	66.2	62.2	76.1	72.1	72.1	70.1	76.1
Moderately Dry	-1.5 – -1.0	14.1	11.9	4.0	10.0	8.0	6.0	8.0	4.0	10.0	11.9	8.0	8.1	10.0	6.0	11.9	6.0	11.9	10.0	11.9	10.0	10.0	10.0	4.0	10.0	10.0	10.0	4.0
Severely Dry	-2.0 – -1.5	4.0	10.0	6.0	4.0	2.0	8.0	6.0	4.0	6.0	2.0	4.0	6.0	6.0	4.0	6.0	13.9	6.0	10.0	2.0	0.0	6.0	6.0	4.0	6.0	6.0	4.0	8.0
Extremely Dry	< -2.0	4.0	2.0	4.0	0.0	4.0	2.0	0.0	2.0	0.0	2.0	2.0	2.0	2.0	6.0	2.0	0.0	0.0	2.0	4.0	2.0	4.0	0.0	4.0	2.0	0.0	0.0	0.0
	Total %	100	100	100	100	100	100	100	100	100	100	100	100	100	100	100	100	100	100	100	100	100	100	100	100	100	100	100

Table 17. Percentage classification values of drought based on 12-month RDI results (%)

		Albacete	Almeria	Asturias	Badajoz Airp.	Barcelona	Bilbao	Burgos	Caceres	Castellon-Alamaziora	Ciudad	Cordoba	Cuenca	Gijon	Girona	Granada	Guadalajara	Huelva	Huesca	Ibiza	Jerez de la Frontera	La Coruna	Leon-Virgen del Camino	Lleida	Logrono-Agoncillo	Madrid	Malaga	Melilla
Extremely Wet	> 2.0	2.0	2.0	0.0	0.0	2.0	0.0	0.0	2.0	2.0	0.0	0.0	0.0	0.0	2.0	2.0	0.0	2.0	0.0	2.0	2.0	2.0	2.0	0.0	2.0	0.0	2.0	4.0
Very Wet	1.5 – 2.0	2.0	2.0	8.0	4.0	2.0	4.0	2.0	8.0	8.0	0.0	4.0	0.0	6.0	6.0	4.0	2.0	2.0	1.7	2.0	0.0	4.0	4.0	7.7	4.0	4.0	6.0	2.0
Moderately Wet	1.0 – 1.5	11.7	0.0	4.0	6.0	8.0	11.7	2.0	18.0	18.0	14.0	10.0	10.0	8.0	10.0	8.0	8.0	12.0	2.0	6.0	6.0	10.0	8.0	8.0	12.0	4.0	8.0	6.0
Near Normal	-1.0 – 1.0	66.3	70.3	68.0	68.0	68.0	58.3	76.0	50.3	50.3	74.0	68.0	76.0	68.0	64.0	64.3	70.0	68.0	76.3	70.0	78.0	70.0	68.0	70.3	64.0	76.0	64.0	68.0
Moderately Dry	-1.5 – -1.0	16.0	19.7	12.0	10.0	6.0	18.0	14.0	9.7	9.7	8.0	14.0	6.0	10.0	14.0	13.7	14.0	10.0	10.0	12.0	10.0	4.0	12.0	6.0	12.0	10.0	12.0	14.0
Severely Dry	-2.0 – -1.5	2.0	4.0	4.0	6.0	10.0	4.0	4.0	12.0	12.0	4.0	4.0	6.0	6.0	4.0	6.0	6.0	6.0	6.0	6.0	4.0	6.0	4.0	4.0	2.0	6.0	4.0	4.0
Extremely Dry	< -2.0	0.0	2.0	4.0	6.0	4.0	4.0	2.0	0.0	0.0	0.0	0.0	2.0	2.0	0.0	2.0	0.0	0.0	4.0	2.0	0.0	4.0	2.0	4.0	4.0	0.0	4.0	2.0
	Total %	100	100	100	100	100	100	100	100	100	100	100	100	100	100	100	100	100	100	100	100	100	100	100	100	100	100	100

		Menorca	Molina di Aragon	Moron de la Frontera	Murcia	Murcia-San Javier	Oreense	Oviedo	Palma de Mallorca	Pamplona-Noain	Ponferrada	Pontevedra	Reus Airp.	Salamanca	San Sebastan-Igueldo	Santander	Santiado de Compostela	Segovia	Sevilla	Soria	Tarifa	Toledo	Valencia Viveros	Valladolid	Vigo-Peinador	Vitoria	Zamora	Zaragoza
Extremely Wet	> 2.0	0.0	0.0	0.0	0.0	1.7	0.0	2.0	0.0	2.0	2.0	2.0	0.0	0.0	2.0	0.0	6.0	2.0	0.0	2.0	0.0	0.0	2.0	0.0	4.0	2.0	0.0	0.0
Very Wet	1.5 – 2.0	6.0	0.0	0.0	0.0	6.0	2.0	6.0	6.0	3.7	2.0	4.0	4.0	2.0	6.0	6.0	0.0	0.0	6.0	2.0	2.0	2.0	4.0	4.0	2.0	4.0	0.0	4.0
Moderately Wet	1.0 – 1.5	2.0	12.0	10.0	9.7	2.0	6.0	6.0	8.0	6.0	10.0	4.0	2.0	6.0	6.0	6.0	0.0	10.0	4.0	8.0	6.0	16.0	8.0	10.0	1.7	6.0	10.0	9.7
Near Normal	-1.0 – 1.0	70.0	64.0	72.0	74.3	74.3	76.0	68.0	72.0	68.3	68.0	76.0	74.0	76.0	70.0	62.0	76.0	76.0	64.3	70.0	82.3	60.0	70.0	68.0	76.3	74.0	80.0	72.3
Moderately Dry	-1.5 – -1.0	12.0	16.0	8.0	10.0	10.0	12.0	12.0	8.0	14.0	12.0	4.0	10.0	10.0	10.0	18.0	8.0	6.0	17.7	10.0	9.7	12.0	12.0	12.0	8.0	4.0	8.0	4.0
Severely Dry	-2.0 – -1.5	8.0	2.0	4.0	6.0	2.0	2.0	6.0	2.0	6.0	4.0	6.0	10.0	4.0	2.0	6.0	6.0	2.0	8.0	6.0	0.0	6.0	2.0	2.0	4.0	10.0	2.0	10.0
Extremely Dry	< -2.0	2.0	6.0	6.0	0.0	4.0	2.0	0.0	4.0	0.0	2.0	4.0	0.0	2.0	4.0	2.0	4.0	4.0	0.0	2.0	0.0	4.0	2.0	4.0	4.0	0.0	0.0	0.0
	Total %	100	100	100	100	100	100	100	100	100	100	100	100	100	100	100	100	100	100	100	100	100	100	100	100	100	100	100

APPENDIX 3

(a)

(b)

(c)

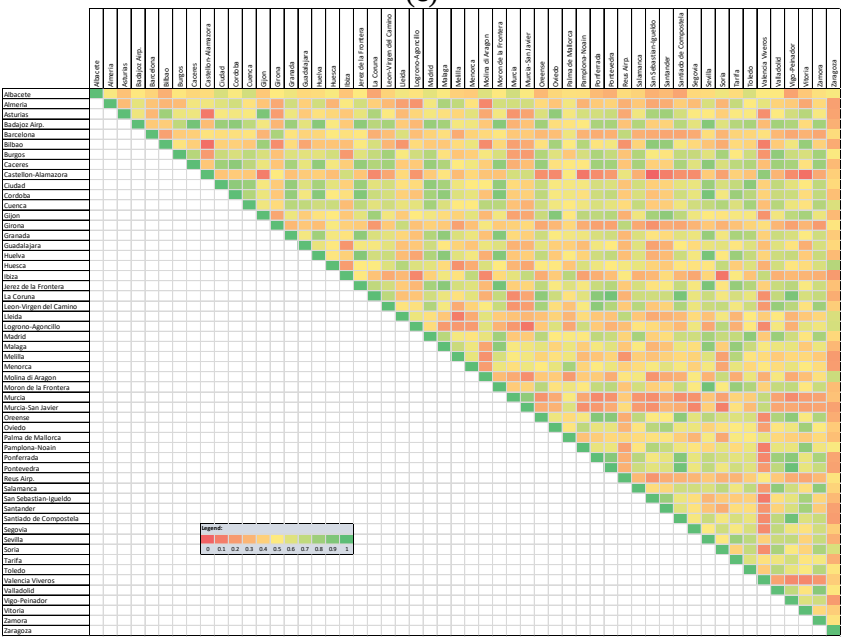
Albacete
Almeria
Asturias
Badajoz Airp.
Barcelona
Bilbao
Burgos
Caceres
Castellon-Alamazora
Ciudad
Cordoba
Cuenca
Gijon
Girona
Granada
Guadalajara
Huelva
Huesca
Ibiza
Jerez de la Frontera
La Coruna
Leon-Virgen del Camino
Lleida
Logrono-Agoncillo
Madrid
Malaga
Melilla
Menorca
Molina di Aragon
Moron de la Frontera
Murcia
Murcia-San Javier
Oreense
Oviedo
Palma de Mallorca
Pamplona-Noain
Ponferrada
Pontevedra
Reus Airp.
Salamanca
San Sebastian-Igueldo
Santander
Santiado de Compostela
Segovia
Sevilla
Soria
Tarifa
Toledo
Valencia Viveros
Valladolid
Vigo-Peinador
Vitoria
Zamora
Zaragoza
Legend:
0 0.1 0.2 0.3 0.4 0.5 0.6 0.7 0.8 0.9 1

(d)

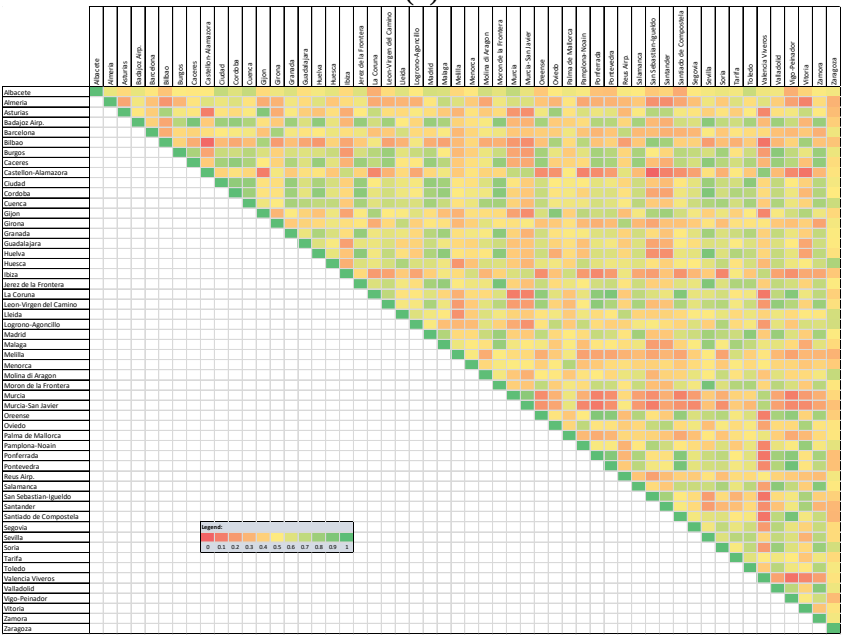
Albacete
Almeria
Asturias
Badajoz Airp.
Barcelona
Bilbao
Burgos
Caceres
Castellon-Alamazora
Ciudad
Cordoba
Cuenca
Gijon
Girona
Granada
Guadalajara
Huelva
Huesca
Ibiza
Jerez de la Frontera
La Coruna
Leon-Virgen del Camino
Lleida
Logrono-Agoncillo
Madrid
Malaga
Melilla
Menorca
Molina di Aragon
Moron de la Frontera
Murcia
Murcia-San Javier
Oreense
Oviedo
Palma de Mallorca
Pamplona-Noain
Ponferrada
Pontevedra
Reus Airp.
Salamanca
San Sebastian-Igueldo
Santander
Santiado de Compostela
Segovia
Sevilla
Soria
Tarifa
Toledo
Valencia Viveros
Valladolid
Vigo-Peinador
Vitoria
Zamora
Zaragoza
Legend:
0 0.1 0.2 0.3 0.4 0.5 0.6 0.7 0.8 0.9 1

(e)

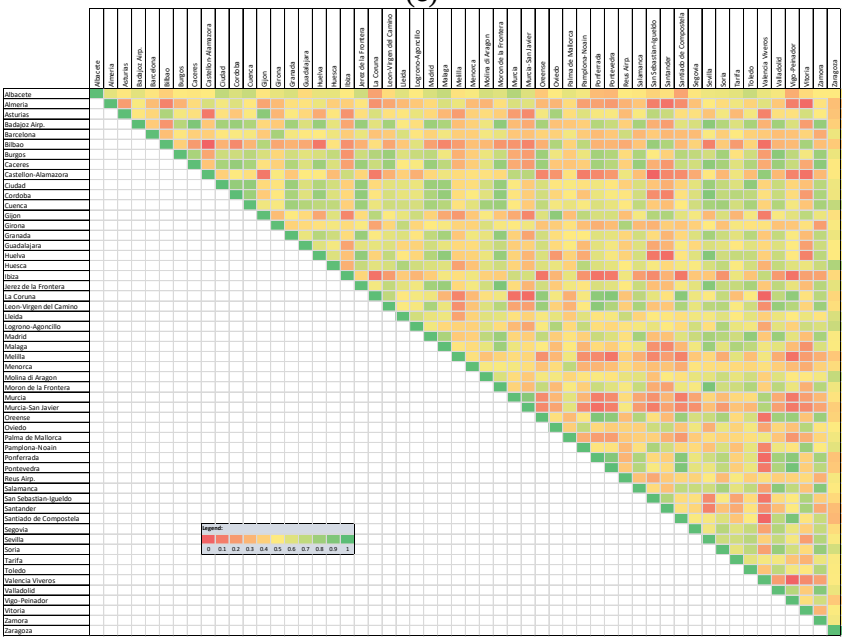

Fig. 10. Correlation coefficients between Spain stations for different time scales of SPI (1, 3, 6, 9, and 12 months) (a, b, c, d, and e)

(a)

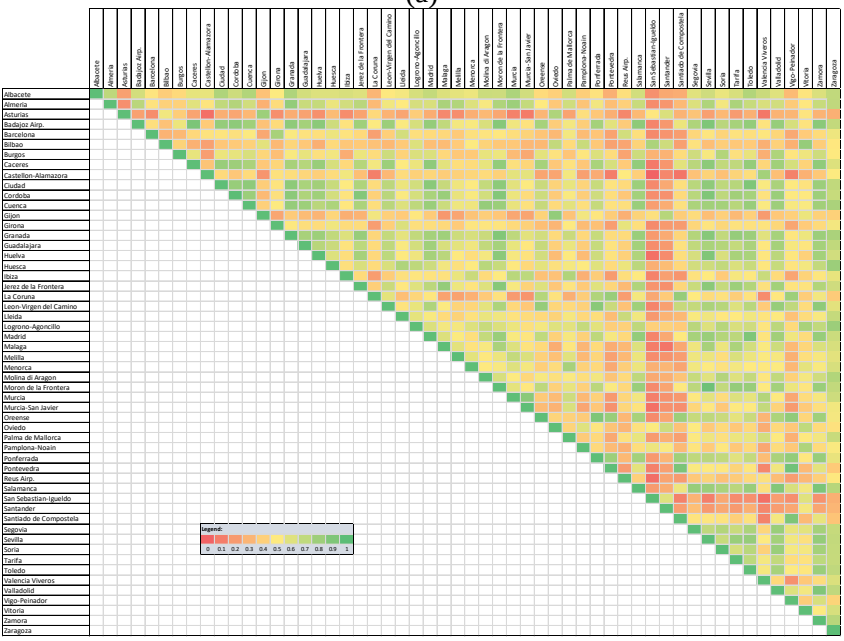

(b)


Albacete
Almeria
Asturias
Badajoz Airp.
Barcelona
Bilbao
Burgos
Caceres
Castellon-Alamazora
Ciudad
Cordoba
Cuenca
Gijon
Girona
Granada
Guadalajara
Huelva
Huesca
Ibiza
Jerez de la Frontera
La Coruna
Leon-Virgen del Camino
Lleida
Logrono-Agoncillo
Madrid
Malaga
Melilla
Menorca
Molina di Aragon
Moron de la Frontera
Murcia
Murcia-San Javier
Oreense
Oviedo
Palma de Mallorca
Pamplona-Noain
Ponferrada
Pontevedra
Reus Airp.
Salamanca
San Sebastian-Igueldo
Santander
Santiado de Compostela
Segovia
Sevilla
Soria
Tarifa
Toledo
Valencia Viveros
Valladolid
Vigo-Peinador
Vitoria
Zamora
Zaragoza
Legend:
0 0.1 0.2 0.3 0.4 0.5 0.6 0.7 0.8 0.9 1

(c)


Albacete
Almeria
Asturias
Badajoz Airp.
Barcelona
Bilbao
Burgos
Caceres
Castellon-Alamazora
Ciudad
Cordoba
Cuenca
Gijon
Girona
Granada
Guadalajara
Huelva
Huesca
Ibiza
Jerez de la Frontera
La Coruna
Leon-Virgen del Camino
Lleida
Logrono-Agoncillo
Madrid
Malaga
Melilla
Menorca
Molina di Aragon
Moron de la Frontera
Murcia
Murcia-San Javier
Oreense
Oviedo
Palma de Mallorca
Pamplona-Noain
Ponferrada
Pontevedra
Reus Airp.
Salamanca
San Sebastian-Igueldo
Santander
Santiado de Compostela
Segovia
Sevilla
Soria
Tarifa
Toledo
Valencia Viveros
Valladolid
Vigo-Peinador
Vitoria
Zamora
Zaragoza
Legend:
0 0.1 0.2 0.3 0.4 0.5 0.6 0.7 0.8 0.9 1

(d)

(e)

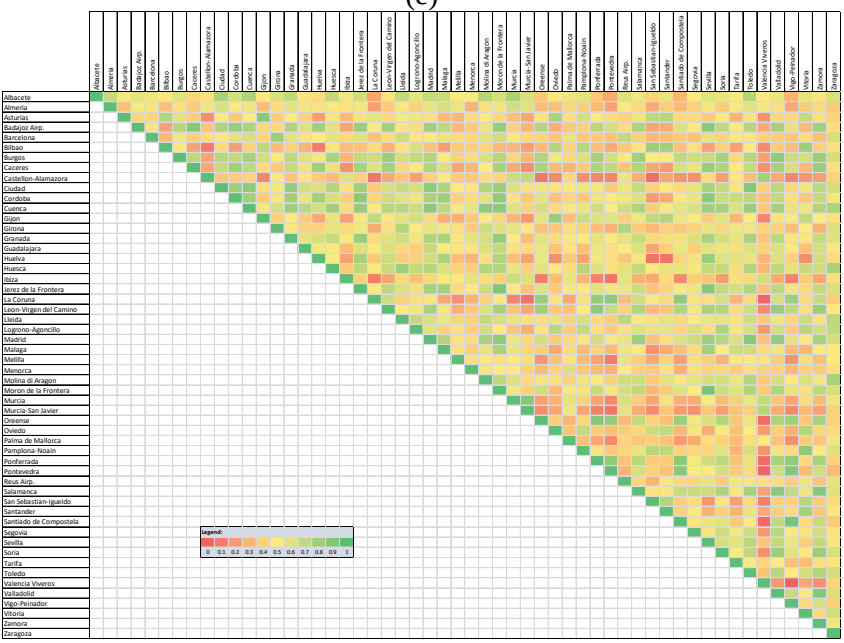

Fig. 11. Correlation coefficients between Spain stations for different time scales of SPEI (1, 3, 6, 9, and 12 months) (a, b, c, d, and e)

(a)

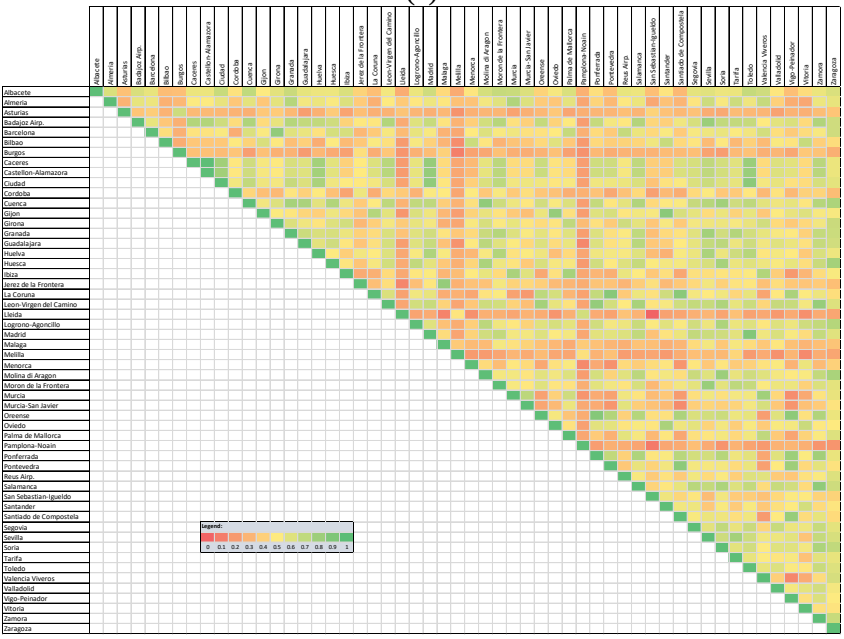
Albacete
Almeria
Asturias
Badajoz Airp.
Barcelona
Bilbao
Burgos
Caceres
Castellon-Alamazora
Ciudad
Cordoba
Cuenca
Gijon
Girona
Granada
Guadalajara
Huelva
Huesca
Ibiza
Jerez de la Frontera
La Coruna
Leon-Virgen del Camino
Lleida
Logrono-Agoncillo
Madrid
Malaga
Melilla
Menorca
Molina di Aragon
Moron de la Frontera
Murcia
Murcia-San Javier
Oreense
Oviedo
Palma de Mallorca
Pamplona-Noain
Ponferrada
Pontevedra
Reus Airp.
Salamanca
San Sebastian-Igueldo
Santander
Santiado de Compostela
Segovia
Sevilla
Soria
Tarifa
Toledo
Valencia Viveros
Valladolid
Vigo-Peinador
Vitoria
Zamora
Zaragoza
Legend:
0 0.1 0.2 0.3 0.4 0.5 0.6 0.7 0.8 0.9 1

(b)

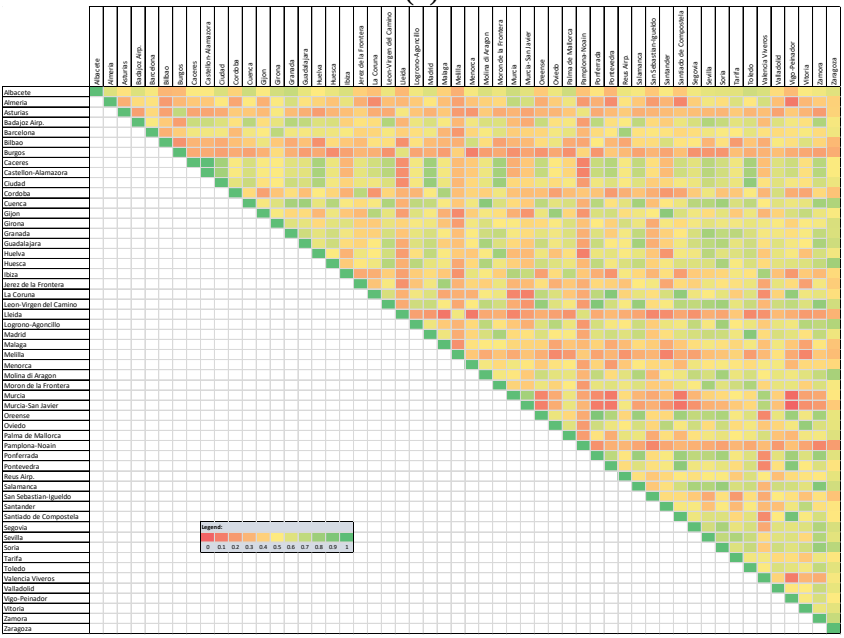
Albacete
Almeria
Asturias
Badajoz Airp.
Barcelona
Bilbao
Burgos
Caceres
Castellon-Alamazora
Ciudad
Cordoba
Cuenca
Gijon
Girona
Granada
Guadalajara
Huelva
Huesca
Ibiza
Jerez de la Frontera
La Coruna
Leon-Virgen del Camino
Lleida
Logrono-Agoncillo
Madrid
Malaga
Melilla
Menorca
Molina di Aragon
Moron de la Frontera
Murcia
Murcia-San Javier
Oreense
Oviedo
Palma de Mallorca
Pamplona-Noain
Ponferrada
Pontevedra
Reus Airp.
Salamanca
San Sebastian-Igueldo
Santander
Santiado de Compostela
Segovia
Sevilla
Soria
Tarifa
Toledo
Valencia Viveros
Valladolid
Vigo-Peinador
Vitoria
Zamora
Zaragoza
Legend:
0 0.1 0.2 0.3 0.4 0.5 0.6 0.7 0.8 0.9 1

(c)

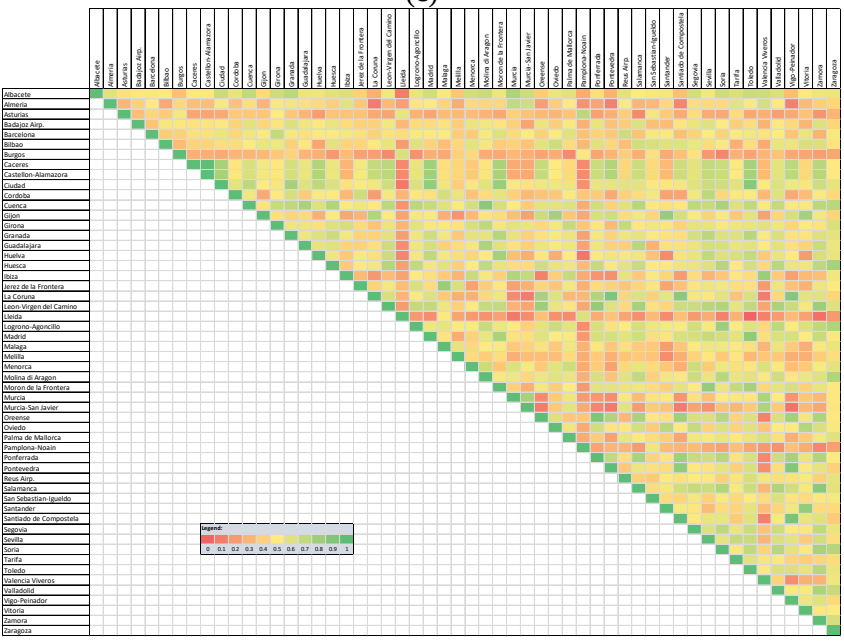
Albacete
Almeria
Asturias
Badajoz Airp.
Barcelona
Bilbao
Burgos
Caceres
Castellon-Alamazora
Ciudad
Cordoba
Cuenca
Gijon
Girona
Granada
Guadalajara
Huelva
Huesca
Ibiza
Jerez de la Frontera
La Coruna
Leon-Virgen del Camino
Lleida
Logrono-Agoncillo
Madrid
Malaga
Melilla
Menorca
Molina di Aragon
Moron de la Frontera
Murcia
Murcia-San Javier
Oreense
Oviedo
Palma de Mallorca
Pamplona-Noain
Ponferrada
Pontevedra
Reus Airp.
Salamanca
San Sebastian-Igueldo
Santander
Santiado de Compostela
Segovia
Sevilla
Soria
Tarifa
Toledo
Valencia Viveros
Valladolid
Vigo-Peinador
Vitoria
Zamora
Zaragoza
Legend:
0 0.1 0.2 0.3 0.4 0.5 0.6 0.7 0.8 0.9 1

(d)

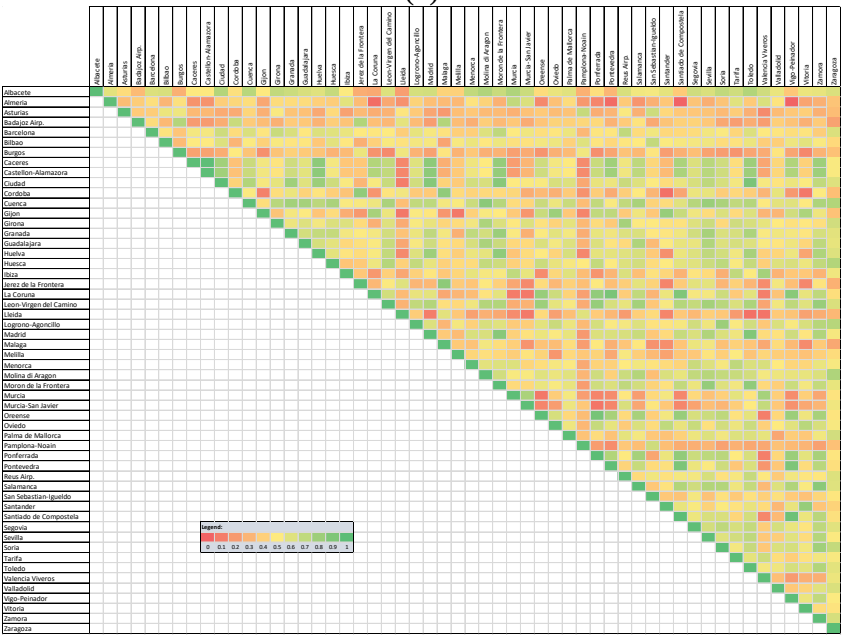
Albacete
Almeria
Asturias
Badajoz Airp.
Barcelona
Bilbao
Burgos
Caceres
Castellon-Alamazora
Ciudad
Cordoba
Cuenca
Gijon
Girona
Granada
Guadalajara
Huelva
Huesca
Ibiza
Jerez de la Frontera
La Coruna
Leon-Virgen del Camino
Lleida
Logrono-Agoncillo
Madrid
Malaga
Melilla
Menorca
Molina di Aragon
Moron de la Frontera
Murcia
Murcia-San Javier
Oreense
Oviedo
Palma de Mallorca
Pamplona-Noain
Ponferrada
Pontevedra
Reus Airp.
Salamanca
San Sebastian-Igueldo
Santander
Santiado de Compostela
Segovia
Sevilla
Soria
Tarifa
Toledo
Valencia Viveros
Valladolid
Vigo-Peinador
Vitoria
Zamora
Zaragoza
Legend:
0 0.1 0.2 0.3 0.4 0.5 0.6 0.7 0.8 0.9 1

(e)

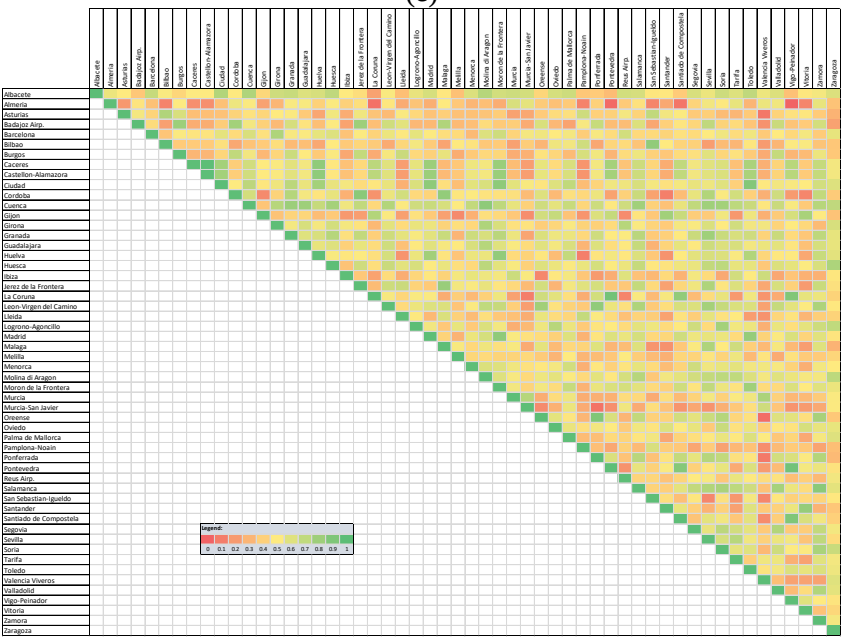

Fig. 12. Correlation coefficients between Spain stations for different time scales of RDI (1, 3, 6, 9, and 12 months) (a, b, c, d, and e)

INSTRUCTIONS TO AUTHORS OF *IDŐJÁRÁS*

The purpose of the journal is to publish papers in any field of meteorology and atmosphere related scientific areas. These may be

- research papers on new results of scientific investigations,
- critical review articles summarizing the current state of art of a certain topic,
- short contributions dealing with a particular question.

Some issues contain "News" and "Book review", therefore, such contributions are also welcome. The papers must be in American English and should be checked by a native speaker if necessary.

Authors are requested to send their manuscripts to

Editor-in Chief of IDŐJÁRÁS
P.O. Box 38, H-1525 Budapest, Hungary
E-mail: journal.idojaras@met.hu

including all illustrations. MS Word format is preferred in electronic submission. Papers will then be reviewed normally by two independent referees, who remain unidentified for the author(s). The Editor-in-Chief will inform the author(s) whether or not the paper is acceptable for publication, and what modifications, if any, are necessary.

Please, follow the order given below when typing manuscripts.

Title page should consist of the title, the name(s) of the author(s), their affiliation(s) including full postal and e-mail address(es). In case of more than one author, the corresponding author must be identified.

Abstract: should contain the purpose, the applied data and methods as well as the basic conclusion(s) of the paper.

Key-words: must be included (from 5 to 10) to help to classify the topic.

Text: has to be typed in single spacing on an A4 size paper using 14 pt Times New Roman font if possible. Use of S.I. units are expected, and the use of negative exponent is preferred to fractional sign. Mathematical formulae are expected to be as simple as possible and numbered in parentheses at the right margin.

All publications cited in the text should be presented in the *list of references*, arranged in alphabetical order. For an article: name(s) of author(s) in Italics, year, title of article, name of journal, volume, number (the latter two in Italics) and pages. E.g., *Nathan, K.K.,* 1986: A note on the relationship between photo-synthetically active radiation and cloud amount. *Időjárás 90,* 10–13. For a book: name(s) of author(s), year, title of the book (all in Italics except the year), publisher and place of publication. E.g., *Junge, C.E.,* 1963: *Air Chemistry and Radioactivity.* Academic Press, New York and London. Reference in the text should contain the name(s) of the author(s) in Italics and year of publication. E.g., in the case of one author: *Miller* (1989); in the case of two authors: *Gamov* and *Cleveland* (1973); and if there are more than two authors: *Smith et al.* (1990). If the name of the author cannot be fitted into the text: *(Miller,* 1989); etc. When referring papers published in the same year by the same author, letters a, b, c, etc. should follow the year of publication. DOI numbers of references should be provided if applicable.

Tables should be marked by Arabic numbers and printed in separate sheets with their numbers and legends given below them. Avoid too lengthy or complicated tables, or tables duplicating results given in other form in the manuscript (e.g., graphs). *Figures* should also be marked with Arabic numbers and printed in black and white or color (under special arrangement) in separate sheets with their numbers and captions given below them. JPG, TIF, GIF, BMP or PNG formats should be used for electronic artwork submission.

More information for authors is available: journal.idojaras@met.hu

Published by the HungaroMet Hungarian Meteorological Service

Budapest, Hungary

ISSN 0324-6329 (Print)

ISSN 2677-187X (Online)